

Aeroelastic analysis and testing of a small wind turbine with thrust force based passive pitch

Department of
Wind Energy
Master Report

Josep Fernandez Gausach

DTU Wind Energy-M-0208

December 2017

DTU Wind Energy
Department of Wind Energy



Authors: Josep Fernandez Gausach

Title: Aeroelastic analysis and testing of a small wind turbine with thrust force based passive pitch

DTU Wind Energy-M-02088

December 2017

Project Period:

July 2017 – December 2017

ECTS: 30

Education: Master of Science

Supervisors:

Taeseong Kim, **DTU Wind Energy**

Robert Flemming Mikkelsen, **DTU Wind Energy**

Sudheesh Sureshkumar, **Enbreeze**

Remarks:

This report is submitted as partial fulfillment of the requirements for graduation in the above education at the Technical University of Denmark.

DTU Wind Energy is a department of the Technical University of Denmark with a unique integration of research, education, innovation and public/private sector consulting in the field of wind energy. Our activities develop new opportunities and technology for the global and Danish exploitation of wind energy. Research focuses on key technical-scientific fields, which are central for the development, innovation and use of wind energy and provides the basis for advanced education at the education.

We have more than 240 staff members of which approximately 60 are PhD students. Research is conducted within nine research programmes organized into three main topics: Wind energy systems, Wind turbine technology and Basics for wind energy.

Technical University of Denmark

Department of Wind Energy
Frederiksborgvej 399
2800 Kgs. Lyngby
Denmark

www.vindenergi.dtu.dk

SUMMARY

In this thesis, a new passive pitch concept based on the thrust force conceived by enbreeze GmbH is analyzed by adapting it to a small wind turbine, and testing it both simulating the model with HAWC2, and building a real prototype for testing it on field.

This report introduces the studied concept. The steps followed to realize the field test are described, explaining designed prototype, the equipment used, and how it has been configured. An optical sensor has been used to measure pitch angle and rotational speed in parallel. The optical sensor and an anemometer have been controlled with an Arduino microcontroller. The possible ways of controlling a permanent magnet synchronous generator (PMSG) are exposed, as well as how the PMSG used in the present study has been controlled using an electronic load and LabVIEW. To enhance and ease the visualization of the acquired data, it is presented a post-processing tool that reads the raw data, enhances and makes it readable by Pdap. It is designed a bending moment sensor for the blade root, and explained the process of attaching strain gages on a thrust-torque sensor.

The wind turbine has been tested in a wind tunnel output before testing it in the field. It is demonstrated that the wind tunnel output is not a reliable wind source. It is also explained how to correct the spectrum of an anemometer to show the right values of turbulence. The field test has been carried out in the Risø test field. The presented results prove the correct performance of the passive pitch system without the use of springs or dampers. It is analyzed a fatigue failure happened during the test.

A model of the wind turbine with the passive pitch system has been implemented in HAWC2. HAWC2 is an aero-hydro-servo-elastic modelling software that allows to simulate the real behavior of the wind turbine. In order to validate the HAWC2 model, the conditions measured in the field test have been recreated, and compared the numerical model with the real prototype. It is also carried out a comparison of the small wind turbine used in this project with the 15kW enbreeze wind turbine, equipped with the same passive pitch system.

Finally, the behavior of the 15kW enbreeze wind turbine is analyzed without the use of a damper on the passive pitch system, which is used at the present to mitigate an instability. It is concluded that the tower oscillation is not causing this instability, and two alternative ways for mitigating this problem are proposed: to equip the generator controller with a PID, and using operations research to optimize the parameters of the passive pitch system linkages.

PREFACE

The present thesis has been carried out in the second semester of 2017 in the department of Wind Energy of the Technical University of Denmark (DTU) and in the headquarters of enbreeze GmbH in Berlin. It is submitted as a final project in fulfillment of the requirements for acquiring both the MSc in Sustainable Energy, Wind Energy specialization, and the Master's Degree in Industrial Engineering in the Polytechnic University of Valencia, in the framework of the T.I.M.E. (Top Industrial Managers for Europe) Double Degree program.

The thesis results from the collaboration between DTU and enbreeze, being Taeseong Kim the supervisor and Robert Femming Mikkelsen the co-supervisor at DTU, and Sudheesh Sureshkumar the supervisor at enbreeze.

Copenhagen, 26th January 2018

Josep Fernández Gausach

ACKNOWLEDGEMENTS

This thesis is my last task before finishing my student life. Although I know I will miss it, I am desiring to start the new stage in my life. However, the time along this project has already been different from what my student life used to be, working in a real project, being challenged everyday by a company.

I would like to express my gratitude to Sudheesh Sureshkumar for all his attention during these months, for passing his enthusiasm on to me, and for all what I learnt from him. I would also like to congratulate him for his great team in enbreeze, which I had the opportunity to work with, and I'm sure their effort will lead to a successful future for them and the company.

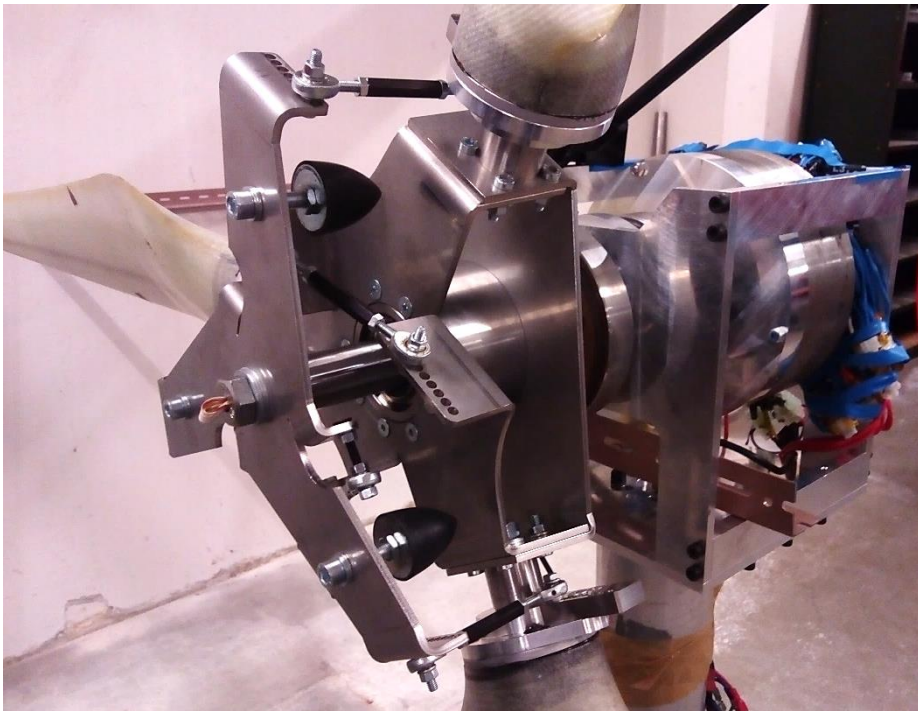
Thanks to Taeseong Kim for all his support and patience with me. It has been a great honor to have been supervised by such a skilled professor.

I would also like to thank Robert Mikkelsen for sharing with me his expertise, for his active contribution on building the prototype and during the tests, and for his clever solutions.

Thanks to Claus Suldrup for his selfless help in the workshop. Especially for making possible to continue de tests, by building a spare component in record time.

Aprofite per a manifestar el que he trobat a faltar en este llarg viatge a la meua família i amics en casa. Gràcies a tots aquells que m'heu recolzat des de la distància. Espere tornar a gaudir prompte de la vostra presència.

Finally, I would like to thank everybody who contributed this last year and five months to my great experience in Denmark. Thanks to all my friends in DTU for sharing their time with me, and thanks to Mads, Jesper and Eva for being so friendly and making me feel like at home.



Enbreeze passive pitch system on DTU small wind turbine

CONTENTS

Summary	i
Preface.....	ii
Acknowledgements	iii
List of abbreviations and acronyms	vii
List of symbols	viii
1. Introduction	1
1.1. Motivation	1
1.2. Precedents.....	2
1.3. Scope and limitations	4
1.4. Outline	5
2. The concept	7
3. Experimental setup.....	9
3.1. Integration of the concept on the DTU SWT	9
3.2. Instrumentation and control.....	11
3.2.1. Sensors.....	11
3.2.2. Signal conditioning.....	14
3.2.3. Data acquisition	15
3.2.4. Post-processing.....	20
3.2.5. Generator control.....	21
3.3. Designing the bending moment sensor	25
3.4. Strain gages on the thrust-torque sensor.....	32
4. Measurement campaigns	35
4.1. Wind tunnel outlet.....	35
4.2. Risø test field.....	39
5. Model of the wind turbine with HAWC2.....	45
5.1. Dynamic simulation	45
5.2. Comparison between DTU 500W SWT and enbreeze 15kW WT.....	49
6. Analysis of the 15kW wind turbine.....	53
6.1. Control solution.....	55
6.2. Design solution.....	56
7. Conclusions	57
8. Future works.....	58
References	59
Appendices.....	62
A. Wind measurement devices.....	62
B. Distance sensors	63

C.	Strain gages attachment.....	64
D.	Generator controllers.....	67
E.	More about measurement campaigns	69
F.	Mann model.....	71
G.	Arduino code for distance sensor and anemometer.....	72
H.	Post-processing code	74
I.	PSD code.....	78
J.	LabVIEW code.....	82
K.	Drawings	84

LIST OF ABBREVIATIONS AND ACRONYMS

AC	Altern Current
ADAMS	Automated Dynamic Analysis of Mechanical Systems
ADC	Analog to Digital Converter
CAD	Computer-Aided Design
CSV	Comma Separated Value
Cp	Power Coefficient
DAQ	Data Acquisition
DC	Direct Current
DIY	Do it yourself
DLL	Dynamic Link Library
DOF	Degree Of Freedom
DTU	Danmarks Tekniske Universitet
DXF	Drawing eXchange Format
Emf	electromotive force
FAST	Fatigue, Aerodynamics, Structures and Turbulence
FEM	Finite Element Method
GF	gage factor
HAWT	Horizontal Axis Wind Turbine
HAWC2	Horizontal Axis Wind turbine simulation Code 2nd generation
HB	Brinell Hardness
HR	Rockwell Hardness
I/O	Input / Output
IP	Index of Protection
ISR	Interrupt Service Routine
LabVIEW	Laboratory Virtual Instrument Engineering Workbench
LIDAR	Laser Imaging Detection and Ranging
LIFA	LabVIEW Interface for Arduino
MATLAB	Matrix Laboratory
MPP	Maximum Power Point
MPPT	Maximum Power Point Tracker
P&O	Perturb and Observe MPPT algorithm
Pdap	Python Data Analysis Program
PLC	Programmable Logic Controller
PMSG	Permanent Magnet Synchronous Generator
PSD	Power spectral density
PWM	Pulse Weight Module
Re	Reynolds number
SD	Secure Digital
SWT	Small wind turbine
TUDeft	Technical University of Delft
VAWT	Vertical Axis Wind Turbine
VI	Virtual Instrument
VISA	Virtual Instrument Software Architecture
WT	Wind turbine

LIST OF SYMBOLS

A	Effective cup anemometer area [m^2]
a	Constant of order 8 [-]
C	First-order constant [-]
c	Chord of the airfoil [m]
coh_{uu}	Spatial coherence between two u components [-]
Δt	Time step [s]
Δz	Distance between two u components [m]
$\varepsilon_{XT,i}$	Crosstalk error on component i [%]
ε_T	Total error [%]
ε_{max}	Maximum error [%]
f	Temporal frequency [Hz]
f_s	Sampling frequency [Hz]
F_{meas}	Measured force [N]
F_{nom}	Nominal force [N]
F_{real}	Real force [N]
F_x	Tangential force [N]
F_y	Normal force [N]
F_z	Centrifugal force [N]
g	Gravity [m/s^2]
H	Hub height [m]
I	Current [A], moment of inertia [$kg \cdot m^2$], turbulence intensity [-]
k_{opt}	Optimal generator characteristic constant [$Nm \cdot s^2$]
κ	Von Kármán constant [-]
l	Cup anemometer response distance [m]
L	Anemometer distance constant [m], Obukhov length scale [m]
Λ	Characteristic instrument length scale [m]
M_{gen}	Generator Torque [Nm]
M_{nom}	Nominal moment [Nm]
M_x	Flapwise bending moment [Nm]
M_y	Edgewise bending moment [Nm]
M_z	Pitching moment [Nm]
μ	Mean
$\mu\varepsilon$	Microstrains
P	Electrical power [W]
P_a	Measured PSD [m^2/s^2]
P_c	Compensated PSD [m^2/s^2]
P_{mec}	Mechanical power [W]
Q_0	Heat flux from ground to air [$K \cdot m/s$]
r	Distance from the shaft axis to the airfoil [m], rotor radius [m]
R^2	Coefficient of determination [-]
σ	Standard deviation
θ_p	Pitch angle [deg]
ρ	Air density [kg/m^3]
T_0	Surface air temperature [$^{\circ}C$]
U	Mean wind speed [m/s]

U_{XT}	Crosstalk uncertainty [N,Nm]
u	Component of the wind speed in the main direction
u_*	Friction velocity [m/s]
ν	kinematic viscosity [Pa·s]
V	Undisturbed wind speed [m/s], Voltage [V]
V_{rel}	Relative velocity [m/s]
ω	Rotational speed [RPM], pulsation [rad/s]
$XT_{i,j}$	Crosstalk of component j on component i [%]

1. INTRODUCTION

The firm enbreeze GmbH has introduced a new concept of passive pitch system that uses thrust force as main governor [1]. Before testing their 15kW wind turbine, this system will be analyzed and tested in a downscale model. The DTU 500W SWT (small wind turbine) [2] will be used in order to prove this new concept, by using HAWC2, and building and testing a real prototype.

1.1. Motivation

Nowadays, the energy generation system is based on a centralized structure, where customers rely on a few big energy producers that control the energy market. An important part of (non-renewable) energy is lost through transmission lines, for the long distance between the customer and the producer, contributing to global warming.

Thanks to technological advances in the energy generation field, the global energy system tends to a more decentralized structure, where security of supply increases, as producers increase in number, and the energy losses are diminished, for increasing the proximity between the customer and the producer.

This thesis follows this path, with the aim to enable common people to become energy producers. To achieve this goal, small generation units, e.g. small wind turbines, require to be more affordable. The way this thesis contributes to more affordable small wind turbines is by giving a step forward in the transition from active pitch systems to passive pitch systems.

Active pitch systems use software to control electronically the pitch angle of the blades. (Active pitch systems are controlled via software-based PLC intelligence, which calculates the required pitch angle for a particular wind speed and executes the changing of pitch angle with hydraulic/ electrical based actuators). These systems are widely used nowadays to limit the power of the wind turbine above rated wind speed. Passive pitch systems are purely mechanical systems, i.e. they don't use software or any active actuator to control the pitch angle. Passive pitch systems, compared to active pitch systems, are more robust and fail-safe. Conversely, rotational speed is more difficult to control precisely. Since the cost of electronics is barely scalable, passive pitch systems are emerging in small wind turbines for being a more economical solution. When it comes to small wind turbines, regulation of power is given higher importance than the regulation of speed. This is because the increased cost associated with electrical components such as generator and inverter are considerably high compared to a corresponding cost to accommodate the increase of loads due to higher rpm.

Pitch systems can pitch to feather or pitch to stall. Pitching to feather, the blade becomes more parallel to the airflow. Pitching to stall, the blades follow the opposite path, creating a high turbulence on the side of the blade that decreases the lift force. While in pitch-to-feather systems, the only load that increases beyond the rated point is the centrifugal force, in pitch-to-stall systems the drag also increases, leading to higher overall loads [3].

For the size of the enbreeze wind turbine, the optimal pitch system is a pitch-to-feather passive pitch system. Therefore, it is interesting to test the passive pitch system invented by enbreeze, as a small contribution for a more competitive green energy. It is also of interest to prove this concept in a smaller scale wind turbine, such as the DTU SWT, not only for economic reasons, but for assessing the replicability of the concept and downscaling.

1.2. Precedents

Many kinds of passive pitch systems already exist in the market. Figure 1 shows a small wind turbine using a rotational speed-based passive pitch system. Its operating mode is analogous to the flyball governor: the higher the rotational speed, the higher the centrifugal force. This centrifugal force pushes out the masses which, in this case, pitch out the blades by leverage effect. The implementation of this system in the DTU SWT is studied in [3].



Figure 1. Small wind turbine with rotational speed-based passive pitch system. Source: [45]

Another kind of passive pitch system, pitch the blade in the axis perpendicular to the span axis. In this system, there is a hinge in the blade root, so that the blade can teeter. The teetering hub principle is mainly used for 2-bladed wind turbines [4]. Figure 2 shows this system applied to a mid-size wind turbine.

Enbreeze GmbH has already developed other passive pitch systems prior to the one studied in this project. Figure 3 shows one of their designs. This design is also based in an equilibrium of forces, like the studied system in this thesis, but the centrifugal force plays a more important role, for the use of the counterweights in the blade root [5].

Beyond passive pitch systems, other passive mechanisms that can keep the power constant are passive stall control, yaw control and air-brakes.

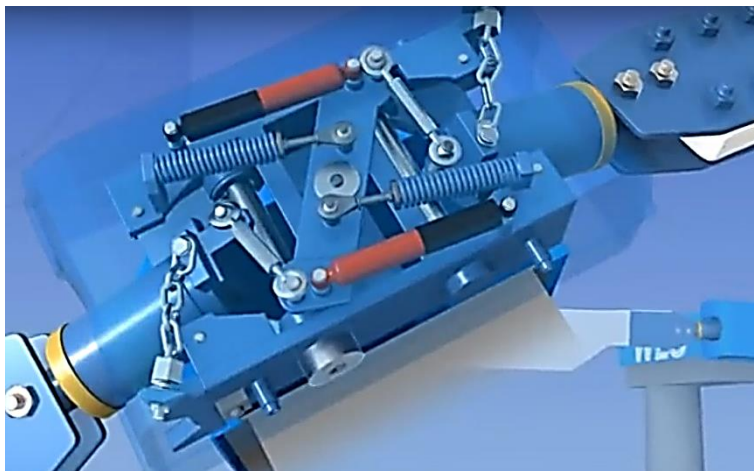


Figure 2. Passive pitch system based on teetering hub principle. Source: [41]

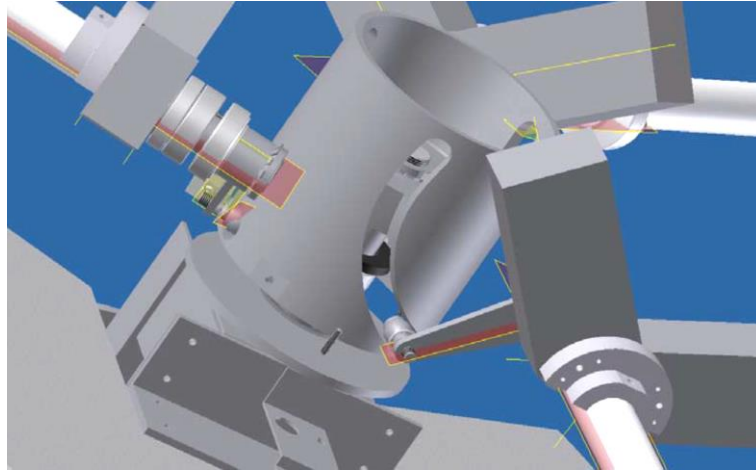


Figure 3. Passive pitch system designed by *enbreeze*. Source: [47]

The passive stall control is one of the simplest configurations. In fact, there is no mechanism. Blades are fixed. The power control is achieved by designing the blade to stall from rated wind speed, so that the lift coefficient decreases with increasing wind speed and, reducing the aerodynamic torque accordingly. The setback of this system is the low efficiency, especially at very high wind speeds [6].

Yaw control consists in limiting the power output by misaligning the rotor plane with respect to the wind direction. Yaw control is not a good technique to keep the power constant, because of the fatigue at which the blades are submitted [7]. On one side, the blades are located upstream the wake, where loads are higher and, on the other side, the blades are located



Figure 4. Wincharger small wind turbine. The governor pitches out its flaps at rated rotational speed to keep the power constant. Source: [48].

downstream the wake, where loads are lower (and turbulence is higher). The rotation of the rotor makes the blades to move between these two sides, creating the aforesaid fatigue.

The air-brake (Figure 4) is an obsolete system used in early small wind turbines. The blades are fixed, but a governor pitches its flaps out at high rotational speeds, working as an aerodynamic brake [8]. The major drawback of this system is that the loads on the blades are not alleviated in any way.

1.3. Scope and limitations

The aim of this project is to prove the passive pitch control system concept in a small-scale wind turbine. In a principle, the best way to achieve the most similar behavior to the enbreeze wind turbine is to downscale the model by means of similarity rules for wind turbine scaling¹.

Similarity rules raise one of the biggest concerns nowadays in wind turbine upscaling. If the geometry of the wind turbine is preserved, aerodynamic stresses are maintained, but stresses due to weight increase linearly with radius. Downscaling is not exempt of limitations. The scaling theory assumes constant drag and lift coefficients. Unfortunately, this is only true when the Reynolds number (Re) is higher than $Re=2e5$. Furthermore, for Reynolds numbers lower than $Re=5e4$, even thin and sharp low-Reynolds profiles no longer produce any lift [9].

To assess if these limitations are overcome, the Reynolds numbers have been calculated for a hypothetical 500W downscaled model from the 15kW wind turbine. The Reynolds number on a blade can be calculated as in Equation 1.

$$Re = \frac{c \times V_{rel}}{\nu} \quad (1)$$

Where c is the chord of the airfoil, ν the kinematic viscosity and V_{rel} the relative velocity on the airfoil, which is determined by the velocity triangle (Equation 2).

$$V_{rel} = \sqrt{(\omega \times r)^2 + V^2} \quad (2)$$

Where ω is the rotational speed of the rotor, r the distance from the shaft axis to the airfoil, and V the undisturbed wind speed.

Figure 5 shows the Reynolds number for several airfoils along the blade and several wind speeds for both the 15kW and the hypothetical 500W downscale wind turbines. To visualize better if the Reynolds number condition is fulfilled, Reynolds numbers above $Re=2e5$, which allow to use similarity rules, have been colored in blue. Reynolds numbers between $Re=2e5$ and $Re=5e4$, which do not allow to use similarity rules due to changes in lift and drag coefficient, have been colored in yellow. Reynolds numbers below $Re=5e4$, where the lift is expected to be 0, have been colored in red.

The situation in Figure 5 reflects the impossibility to use a downscaled model, since the downscale model is under Reynolds under $Re=2e5$ for most of the airfoils and wind speeds, so similarity rules would not be fulfilled.

The DTU 500W SWT has been used, as advanced before. This situation is not undesirable. In fact, it can be seen as an opportunity to assess the behavior of the system in study

¹ Other machines, such as turbopumps, use also similarity rules. The principle is the same, but the resulting rules differ considerably, since a focus in different parameters, e.g. relative pressure or number of stages, is given.

in a different wind turbine. Nonetheless, some changes have been applied to the DTU 500W SWT in order to resemble more to the 15kW enbreeze WT, as will be explained in section ‘3.1. Integration of the concept on the DTU SWT’.

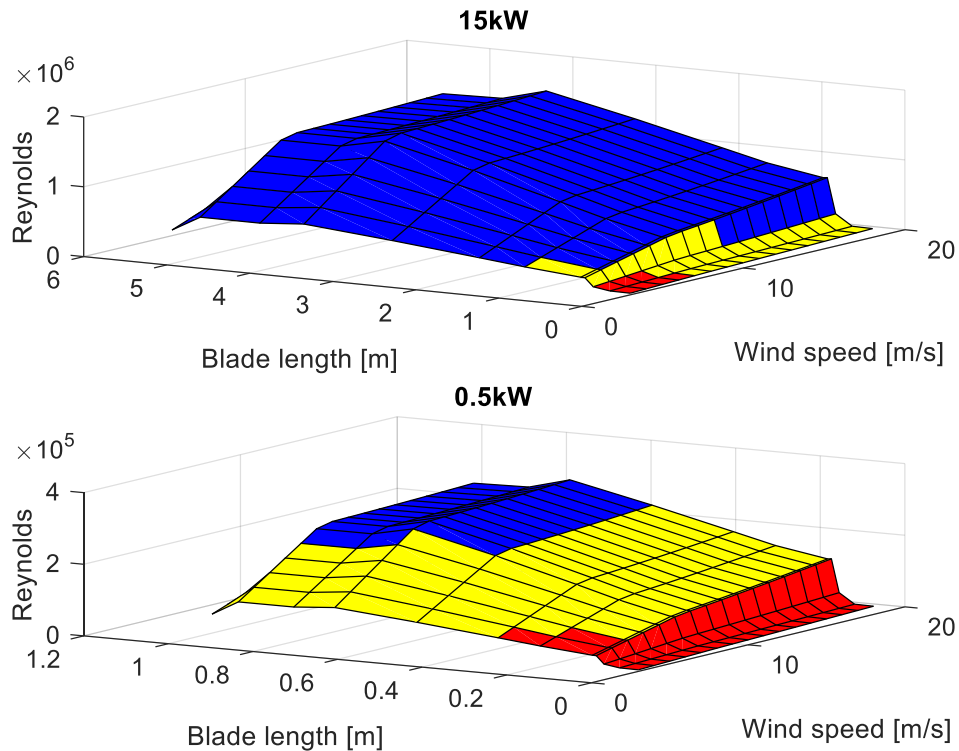


Figure 5. Reynolds number in function of the blade length and wind speed for the 15kW and its hypothetical 0.5kW downscale. Blue: $Re > 2e5$. Yellow: $Re \in [5e4, 2e5]$. Red: $Re < 5e4$.

Another reason why it has been decided to start this project is to approach the reduction of an instability that prevents the correct operation of the passive pitch system in the 15kW wind turbine when a damper is not used. In this project, a stiff tower will be used, because it is thought that the instability comes from the oscillation of the tower. In the next semester another student will evaluate the behavior of the SWT with a flexible tower. In addition, a master student doing his thesis in enbreeze is focusing on the solution of this instability. Nevertheless, due to the experience acquired in this project, a study about this issue will be shown in this paper, under chapter ‘6. Analysis of the 15kW wind turbine’.

1.4. Outline

This thesis shows the entire process of building and analyzing a passive pitch system on a small wind turbine. The report is divided into 6 major chapters: The concept, Experimental setup, Measurement campaigns, Model of the wind turbine with HAWC2, Analysis of the 15kW wind turbine and Conclusions.

Chapter 2. The concept, explains how operates the passive pitch system introduced by enbreeze.

Chapter 3. Experimental setup, guides the reader through the design of the passive pitch system integrated in the DTU SWT. The chapter continues with the design of the instrumentation and control system.

In chapter 4. Measurement campaigns, the experimental tests carried out in a wind tunnel output, as well as in the test field, are explained, showing the results from the measurements, and sensitivity analyses.

The thesis continues with chapter 5. Model of the wind turbine with HAWC2, where the numerical model is explained, and the results from the simulation are shown and contrasted with the experimental measurements. Once the numerical model is validated, the chapter concludes with a comparison of the numerical models of the DTU SWT and the enbreeze WT.

Chapter 6. Analysis of the 15kW wind turbine, focuses on the analysis of the 15kW enbreeze wind turbine without the use of a damper, posing solutions for the present instability.

The report is concluded with chapter 7. Conclusions, where the most remarkable points along the thesis are collected.

2. THE CONCEPT

In this chapter, the passive pitch concept introduced by enbreeze GmbH is explained. A 2D scheme of the system is shown in Figure 6. In this system, the pitch angle is the result of an equilibrium of forces between the generator disc and the hub. The generator disc moves together with the shaft, which is considered fixed to ground in the figure. The generator disc and the hub reach a force equilibrium through the generator rod. The main contributor on the generator disc is the torque from the generator, and the main contributor on the hub is the thrust force. A change in this force equilibrium causes a linear motion of the hub, constrained by the slider. This linear motion is transformed into rotational motion on the blade by using a crank-connecting rod mechanism.

The system presented in this project features a clear advantage: although it is a passive system, it still has one control DOF (Degree Of Freedom), the generator torque. By adjusting the generator torque, the wind turbine can work in the partial load region² without excessive values of rotational speed.

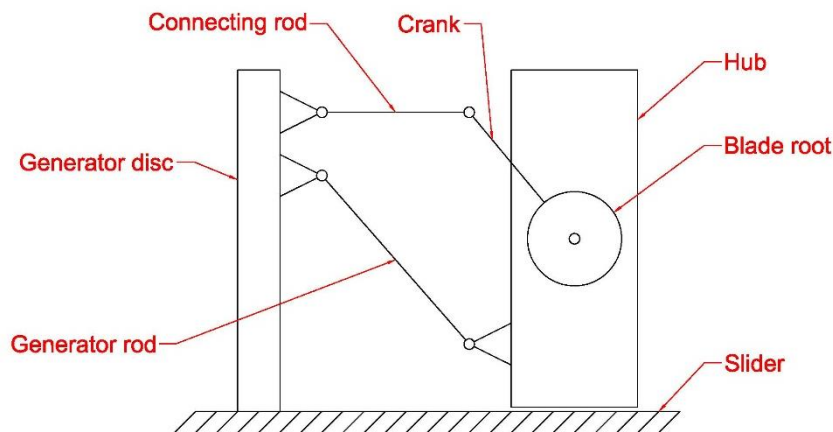


Figure 6. 2D model of the passive pitch system.

The terms that contribute to pitch out are the thrust and the centrifugal force, while the terms that contribute to pitch in are the aerodynamic torque and the generator torque. The linkages are designed such that at rated wind speed, the blades begin to pitch, i.e. the forces from the terms that contribute to pitch out are higher than the forces from the terms that contribute to pitch in. This behavior, in combination with synchronous generators, which decrease their torque beyond the rated rotational speed (in order to keep constant power) makes the system able to pitch out in the required amount when rated power is reached. The correct adjustment of the linkages of the passive pitch system enables the blades to follow the correct pitch angle as the wind speed increases. So, varying the positions of these linkages, the system can be adapted to different wind turbines.

The abovementioned behavior implies a safety advantage: the system pitches out when the generator is lost (or disconnected voluntarily). Therefore, the wind turbine slows down when, for example, an electrical failure happens. This enables the wind turbine to avoid the use of a mechanical brake, which is a clear advantage compared with active pitch systems.

² A wind turbine is working in partial load when it produces less than what it is able to produce. The partial load region is the area below the power curve in a power vs wind speed graph, e.g. Figure 60.

Furthermore, the opposite procedure provides also an advantage: increasing the generator torque, the blades pitch in. So, no auxiliary element, such as a spring, is needed to reset the system after it has been activated.

It is noteworthy to say that the 2D model shown in Figure 6 is overconstrained. To allow mobility, the hub rotates on the plane perpendicular to the linear movement direction. The 3D configuration of the system for a single blade can be seen in Figure 7. To allow both linear and rotational motion on the hub over the slider, roller bearings are mounted on top of a linear bearing, as seen in Figure 8. The connecting rod and the generator rod also require various DOF, which are achieved by using joint bearings. In addition, to impose the minimum and maximum pitch angles and, at the same time, preventing the system from strong impacts, bumpers are used.

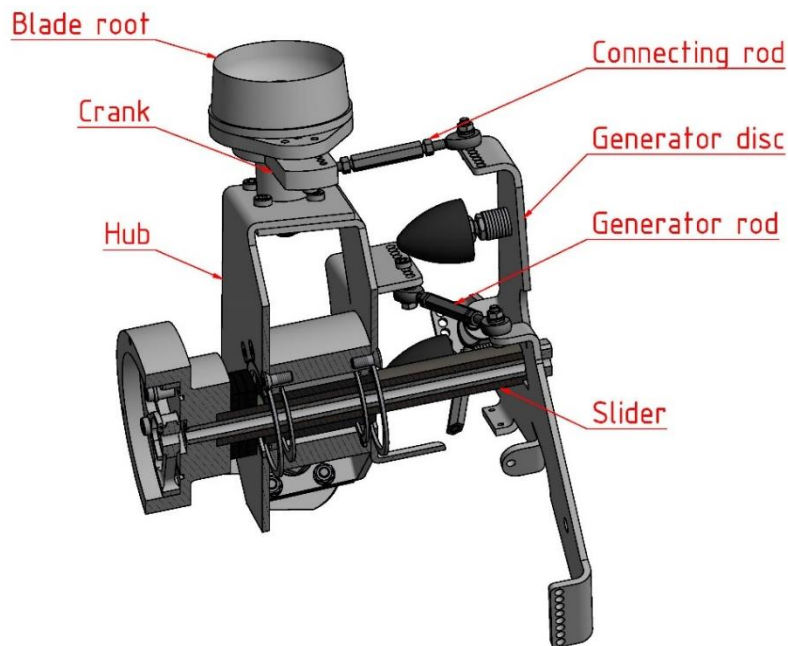


Figure 7. Main components of the passive pitch system.

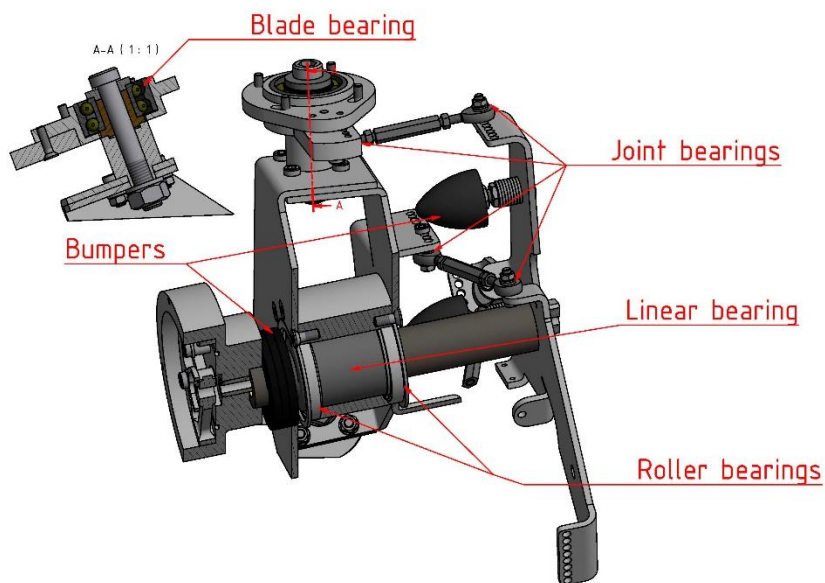


Figure 8. Secondary components of the passive pitch system

3. EXPERIMENTAL SETUP

Numerical model simulations are a cheap and fast way to predict real systems' behavior. However, numerical models can present errors or inaccuracies due to simplifications or estimated parameters that can lead the resulting simulation to behave different than in the reality. Conversely, real models are exempt of these uncertainties. However, results from real models can differ from the reality due to errors and uncertainties in the measurements. In this chapter, the setup of the real model, as well as the measurement system will be exposed.

3.1. Integration of the concept on the DTU SWT

The 500W DTU SWT is a homemade wind turbine. Until this project, it has been 3-bladed, upwind, direct-drive, with a PMSG (Permanent Magnet Synchronous Generator).

The enbreeze passive pitch system has been implemented on the DTU SWT by replacing its hub. In order to resemble more to the 15kW enbreeze wind turbine, the DTU SWT has been modified to downwind, by simply turning the blades 180°. The coning angle of the blades has been set to 6 degrees³.

The most important task in the design of the new hub has been to calculate the dimensions of the passive pitch system linkages. The inputs for this calculation are the forces on the blade (normal and tangential force), the pitching moment (on the pitch axis of each blade), the moment on the rotor shaft, and the mass of the blades. The inputs are a function of the wind speed, rotor speed and pitch angle. HAWC2 has been used to provide these inputs. More information about HAWC2 can be found in chapter '5. Model of the wind turbine with HAWC2'.

The calculation consisted in using the forces and moments obtained in the HAWC2 simulation to calculate the linkages positions and lengths. To do so, a first step has been to calculate the pitching moment on the blade from the forces and moments from HAWC2. It has also been calculated the required generator torque to achieve the desired power at the range of wind speeds where the passive pitch system is activated. With these parameters, it has been calculated a first approximation to the linkages positions and lengths. Due to the complexity of the system, some simplifications have been taken, such as using the 2D model presented in Figure 6. Once the first approximation is obtained, the values are fine-tuned by an iterative process with the help of HAWC2. An alternative to this process is proposed in section '6.2. Design solution'.

The new hub is bigger than the previous hub. For this reason, the rotor diameter has increased from 1.6m to 1.75m. This modification leads to the need of looking for a new optimum pitch angle (which corresponds to completely pitched in blades), because the angles of attack have changed with this modification. The new optimum pitch angle is found by finding the power coefficient (C_p) for different values of pitch angle and tip speed ratio, and choosing the pitch angle with the highest associated C_p . This exercise could not be carried out for time issues, and it is proposed in the '8. Future works' section.

An improvement that has been given to the DTU SWT is to manufacture a centering in the already existing shaft, for a better fit between the shaft and the hub.

The slider of the passive pitch system has been designed to be made of steel, since aluminum is not enough hard. Figure 9 shows the hardness factor in function of the Rockwell hardness for a linear bearing. The hardness factor indicates the real lifetime with respect to the ideal lifetime in function of the hardness of the surface.

³ It has been set to 6 degrees for similarity with the enbreeze wind turbine. According to [57], this value is the one that provides a fastest yawing response without overshoot, if integrated in a passive yaw system. Furthermore, if the blades feature a coning angle, the centrifugal forces compensate the aerodynamic bending moment.

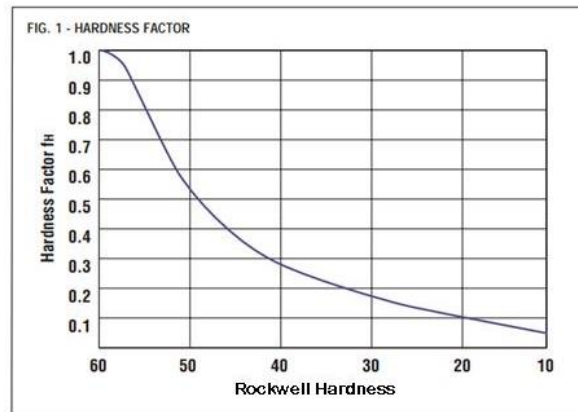


Figure 9. Hardness factor for a linear ball bearing. Source: PBC linear.

Although a long lifetime is not important for this project, a Rockwell hardness of 10 HR gives a lifetime of around the 5%. The aluminum, without any treatment has a hardness lower than 95 HB (Brinell hardness), which does not even have an equivalent in the Rockwell scale, because it is too soft. Therefore, the use of aluminum is not acceptable. The chosen steel for the slider has a hardness of 50 HR.

Regarding threaded joints, as the system is prepared to change the position of the linkages, locknuts have not been considered, since they can only be used once. Glue for threaded unions has been used instead.

Figure 10 shows the CAD model of the new hub with the passive pitch system made with Autodesk Inventor. The drawings of the non-standard parts, i.e. the parts that require to be manufactured, are attached in Appendix K.



Figure 10. CAD model of the passive pitch system.

To set the correct twist angle, the angle indicator shown in Figure 11 has been used. To check that the pitch system moves from 0 to 35° an android app called ‘Precise level’, which works in the same manner as a real level, has been used.



Figure 11. Aligning the blade with respect to the rotor plane.

3.2. Instrumentation and control

This section addresses the instruments and software used for measuring and recording data from the wind turbine, as well as controlling it. Before starting for each individual part, an overall view of the system is shown in Figure 12. In the upper side of this figure are shown the devices inside the wind turbine. In the rotor are located the force sensors, whose data are sent wirelessly to the computer. It can be seen that the distance sensor measures both distance, which will be converted to pitch angle, and rotational speed. The 3-phase generator is connected to the DC electronic load via a rectifier. The emergency brake control system, in the right side of the figure, is the only sub-system independent of the computer. The electronic load measures voltage, power and resistance, and, in this case, it controls and measures current. The anemometer, in the left-bottom side, it is connected to the same Arduino controller as the optical sensor. Finally, the computer collects and processes all signals from the measurements, and sends the instructions to the electronic load to control the generator.

3.2.1. Sensors

In an ideal case, only one variable is needed to know the operational point of the WT, such as wind speed or power output. However, it is needed to check that the prototype works as expected and, in case of a bias, be able to identify where is the problem. Therefore, some more variables are needed to confirm that the wind turbine is working in a specific operational point:

- Wind speed and direction
- Pitch angle
- Rotational speed
- Voltage and current output from the generator

And it is also helpful to measure other variables, such as:

- Loads in the blade root
- Loads in the shaft

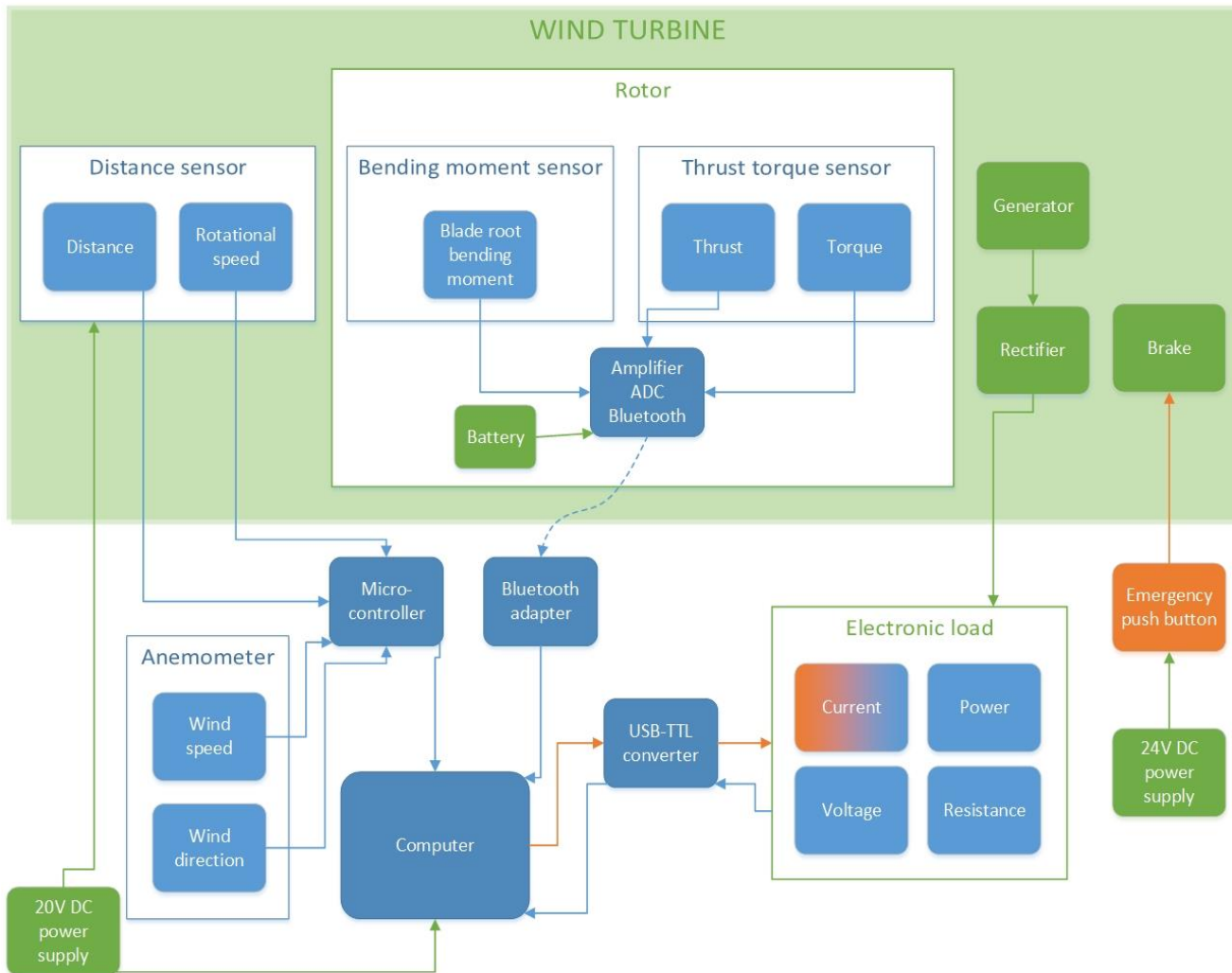


Figure 12. Instrumentation and control diagram of the entire system. Green: electric equipment and power flow. Blue: sensors, measured variables (light blue), DAQ equipment (dark blue) and DAQ signals. Orange: controlled elements and control signals.

Wind speed and direction

In order to measure wind speed and direction many different the state-of-the art technologies such as sonic anemometers or LIDAR (see Appendix A) can be used. But in this study, we used a cup anemometer because it is cheap and easy to implement to the system. Cup anemometers present some inaccuracies when measuring the wind speed. Due to inertia, they don't respond instantaneously to changes in wind. The effect of the inertia can be seen as a first-order filter with a length scale of 1-2m [10]. Cup anemometers measure the wind speed over a plane (two components). To know the direction of the wind in that plane, a vane is used. For this project, the wind direction is useful to know if the rotor plane is perpendicular to the wind direction. The cup anemometer used in this study, which includes a vane, is the DAVIS 6410 (Figure 13).



Figure 13. DAVIS 6410 Cup anemometer.
Source: [49]

Pitch angle and rotational speed

The optical sensor shown in Figure 14 has been used to measure both pitch angle and rotational speed. The other sensors considered in the selection process are examined in Appendix B.



Figure 14. Optical sensor. Source: [11]

The optical sensor has two operating modes that can work simultaneously and configured independently: analog output and switching output. The analog output provides an analog signal, while the switching output provides a Boolean signal. This Boolean signal can be used as a tachometer⁴ if at least once a revolution there is a certain distance measurement outside the sliding plate range. To put this into practice, the auxiliary component in Figure 15 has been designed and manufactured using a laser cutter. This component has been placed between the sliding plate and the distance sensor. The analog signal, however, suffers three perturbations every revolution. These perturbations are minimized with the design in Figure 15, and they can be completely eliminated in the post-processing phase, as will be explained in the '3.2.4. Post-processing' section.

⁴ A tachometer and an incremental encoder are very similar instruments. A tachometer measures rotational speed while an incremental encoder measures relative position. The designed configuration can work as a tachometer as well as an incremental encoder, but as the purpose is to measure rotational speed, the present configuration is referred as tachometer.

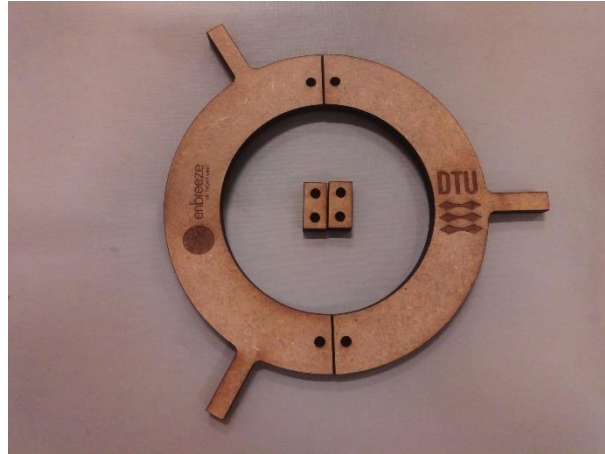


Figure 15. Auxiliary component to measure rotational speed.

Voltage and current

The voltage and current output from the generator have been measured by means of a DC electronic load (Figure 25, page 24). More details about the electronic load are given under ‘3.2.5. Generator control’ section.

Electric power and resistance can be calculated easily from voltage and current. Power is the product of these two, and the resistance the quotient of the voltage divided by the current (Ohm’s law). However, power and resistance are acquired from the electronic load for redundancy.

Loads

Loads are calculated indirectly from deformations, by using strain gages. Strain gages can be placed directly on existing components, or in special components designed to attach strain gages. In this last case, the device is called load cell⁵ or force sensor.

As explained in the section ‘3.3. Designing the bending moment sensor’, only bending moment can be measured in the blade root of the wind turbine in study. The bending moment sensor (Figure 28, page 27) could not be manufactured due to time reasons. Furthermore, the chosen amplifier (Figure 16) could not be purchased due to budget reasons. The thrust-torque sensor (Figure 29, page 28) could be completed. The design of the strain gages arrangement on this sensor is shown in section ‘3.4. Strain gages on the thrust-torque sensor’. Appendix C shows the attachment of the strain gages according to the resulting arrangement.

3.2.2. Signal conditioning

The optical sensor, the anemometer and the electronic load do not need signal conditioning to be read by the computer or microcontroller. They do the force sensors.

The voltage output from the Wheatstone bridge of the strain gages is very low. For the case of the thrust-torque sensor it is maximum 0.5mV/V, as derived in section ‘3.3. Designing the bending moment sensor’, which, for a source voltage of 2.5V, it means a maximum output of 1.25mV. Therefore, an amplifier is needed.

As the force sensors are in the rotor, the signal from the amplifier cannot be transferred directly by cable. Either a slip ring or wireless system are needed. Slip rings have been considered for this application. They have a disadvantage, which is that they add noise to the signal. Good

⁵ Load cell is a term commonly used in weighing systems.

slip rings have an electrical noise of around 0.01Ω , which is not a big issue. The reason why a slip ring has been discarded is the price. On the other side, a disadvantage of wireless devices is that they need a battery to work. These add weight to the rotor and their life is limited. However, wireless devices are cheaper than slip rings.

The chosen device is the ME-Systeme GSV-4BT M12, which includes amplifier, ADC (Analog to Digital Converter) and Bluetooth⁶ transmitter.



Figure 16. ME-Systeme GSV-4BT M12. Source: [35]

Apart from the competitive price and its wireless connection, these are other relevant characteristics for this project:

- IP67 environmental protection. So, it is protected against the rain.
- 16-bit resolution and 5% accuracy class. The accuracy is more than enough, compared with the errors that are being committed on the wind speed measurement.
- 4 channels. This means that 4 bridges can be measured at the same time. For this project, 3 channels are needed: blade root bending moment, thrust and torque.
- 450Hz Sampling frequency. This is explained below in the ‘3.2.3. Data acquisition’ section.

A very important parameter this manufacturer does not provide is the vibration the device can withstand without being damaged. Another amplifier, the NI 9237 specifies on its datasheet a maximum vibration of $5g^7$, which is much higher than the vibration on the SWT rotor. According to the HAWC2 simulations, the vibration in the rotor is expected to be lower than $0.3g$. On a call with the manufacturer, they pointed out that some customers have already used their device under heavier vibrations without any problem.

3.2.3. Data acquisition

A sensor cannot be connected directly to a computer. Sensors are the first ‘step’ in the DAQ (Data Acquisition) chain. An example of DAQ chain is shown in Figure 17. The second step is the signal conditioning. The following step is the DAQ hardware and software. These vary from one application to another. For example, a stand-alone DAQ system does not need a computer. A stand-alone DAQ system could be, for example, a microcontroller collecting data

⁶ The Bluetooth card is a long-distance Bluetooth interface with up to 1000m range. This is not much important on this project but, as a comparison, USB cables can reach up 5m length and Ethernet cables up to 100m length before needing a hub, switch or repeater [39].

⁷ 5 times the acceleration of the gravity (9.81m/s)

from a sensor into an SD card. This configuration could be a cheaper alternative to the abovementioned Bluetooth strain gage DAQ, but it has not been implemented because an important purpose was to visualize live data.



Figure 17. DAQ chain example. Source: [54]

In the adopted configuration, different hardware send data to the computer and, in the computer, the data is recorded and visualized. A single DAQ hardware has not been used because the strain gage amplifier⁸, as well as the electronic load, have their own DAQ hardware.

To control the anemometer and the distance sensor, the same microcontroller has been used: an Arduino Uno. The possibilities of this low-cost microcontroller are limited. For example:

- It does not include a current-to-voltage converter, so all input signals must be in voltage terms.
- The voltage input has to be from 0 to 5V. The analog input only comprises 1024⁹ different levels.
- It is not rugged: it does not have any mechanical protection, nor overcurrent or overvoltage protection. Long-term reliability is not guaranteed.

The first issue is not a problem for this application. The distance sensor, as well as the anemometer, give the signal in voltage terms.

The second issue can be fixed using voltage dividers. 10-bit resolution is enough for this application. For this resolution, if the range of the angle is from 0° to 35°, it means steps of 0.034°.

The issue of the mechanical protection is fixed partially by using a case (shown in Figure 20). Arduino is a simple electronic board, it cannot be compared to industrial PLCs in terms of ruggedness. As there are not lives at stake, a failure is not critical. The cost of a PLC does not compensate the cost of buying a new Arduino if it failed, even if it happens several times.

Before showing how these sensors have been hooked up to Arduino, the required sampling frequency is found. If it is desired to have the same results as in HAWC2, the sampling frequency would be $f_s = \frac{1}{\Delta t} = \frac{1}{0.001} = 1000\text{Hz}$. On the other hand, there is no need to get frequencies higher than $3P^{10}$, that, for a rotational speed of 650rpm (10.83Hz) corresponds to 32.5Hz and, considering the Nyquist theorem, which says that the minimum sampling frequency has to be at least the double of the maximum frequency, the minimum sampling frequency needed is $f_{s,min}=65\text{ Hz}$.

⁸ The manufacturer calls it amplifier, but it is actually an amplifier + ADC + Bluetooth transmitter

⁹ 1024 levels mean a resolution of 10 bits. $2^{10} = 1024$.

¹⁰ $P = \frac{2\pi}{\omega_{max}}$, where ω_{max} is the maximum achievable rotational speed (beyond the rated speed)

Distance sensor DAQ

As in the datasheet of the distance sensor is specified that the operating voltage of the optical sensor has to be between 13 and 30V, and Arduino can only provide a voltage of 5V, a 20V computer power source has been used.

The analog output gives a voltage between 0 and 10V, and the switching output gives the same voltage as the power source (20V) when it is on. Therefore, voltage dividers as in Figure 18 have been implemented. The resistance R1 has been set to 10 k Ω . If the resistance is too low, too much energy will be wasted. If the resistance is too high, the Vout measurement can be affected, because it has been assumed that there is not current flow towards Vout, but it is a simplification. The Arduino pin has an internal resistance of 100 M Ω . The resistance R2 has been calculated according to Kirchoff's voltage law. The result is R2=10k Ω for the analog output (black cable), and R2=3.33k Ω for the switching output (white), which becomes 3.30k Ω when taking an E6 series value, as seen in Figure 19. The V- pin (color blue in Figure 19) has been connected to ground, to close the circuit.

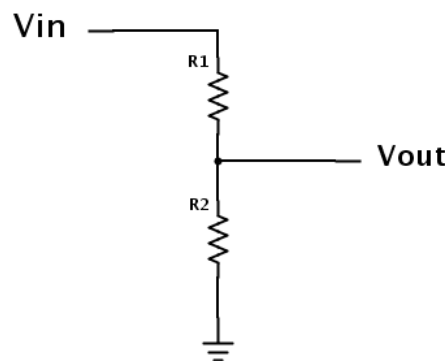


Figure 18. Voltage divider

Once the sensor can be connected to the controller, the code to acquire data from it can be implemented. To visualize, register and control the whole system, LabVIEW has been used. LabVIEW (Laboratory Virtual Instrument Engineering Workbench) is a development environment that allows to create programs using a graphical language, called G. LabVIEW offers an interface for Arduino, called LIFA (LabVIEW Interface for Arduino). LIFA is a code for Arduino that, when uploaded to the microcontroller, the device can be controlled from the LabVIEW environment with specific VIs (Virtual Instruments). This interface, however, had to be discarded for being too slow. While tested, it could not exceed sampling frequencies of 5Hz. Instead, Arduino has been programmed with its own programming code, and the connection with LabVIEW has been done through a VISA (Virtual Instrument Software Architecture). This configuration is a little more difficult to implement but, in this way, the microcontroller and the computer distribute tasks. The microcontroller is in charge of converting the input signal into real magnitudes, while the computer is in charge of visualizing and recording them. The Arduino code can be seen in appendix G. This code is shared for the distance sensor and the anemometer.

To measure rotational speed, the elapsed time and the number of rising edges in a loop cycle are measured. A rising edge is the step from LOW to HIGH in the pin, i.e. when the auxiliary component crosses the beam of light of the distance sensor. To not lose any rising edge, an ISR (Interrupt Service Routine) is utilized. ISRs stop what the controller is doing when a trigger (in this case a rising edge) is activated, and run the code inside this routine. The code inside an ISR has to be as short as possible, since the time does not increment until the ISR finishes. A long ISR would mean, then, an added error to the rotational speed measurement. In the presented code, inside the ISR is only incremented the rising edges counter.

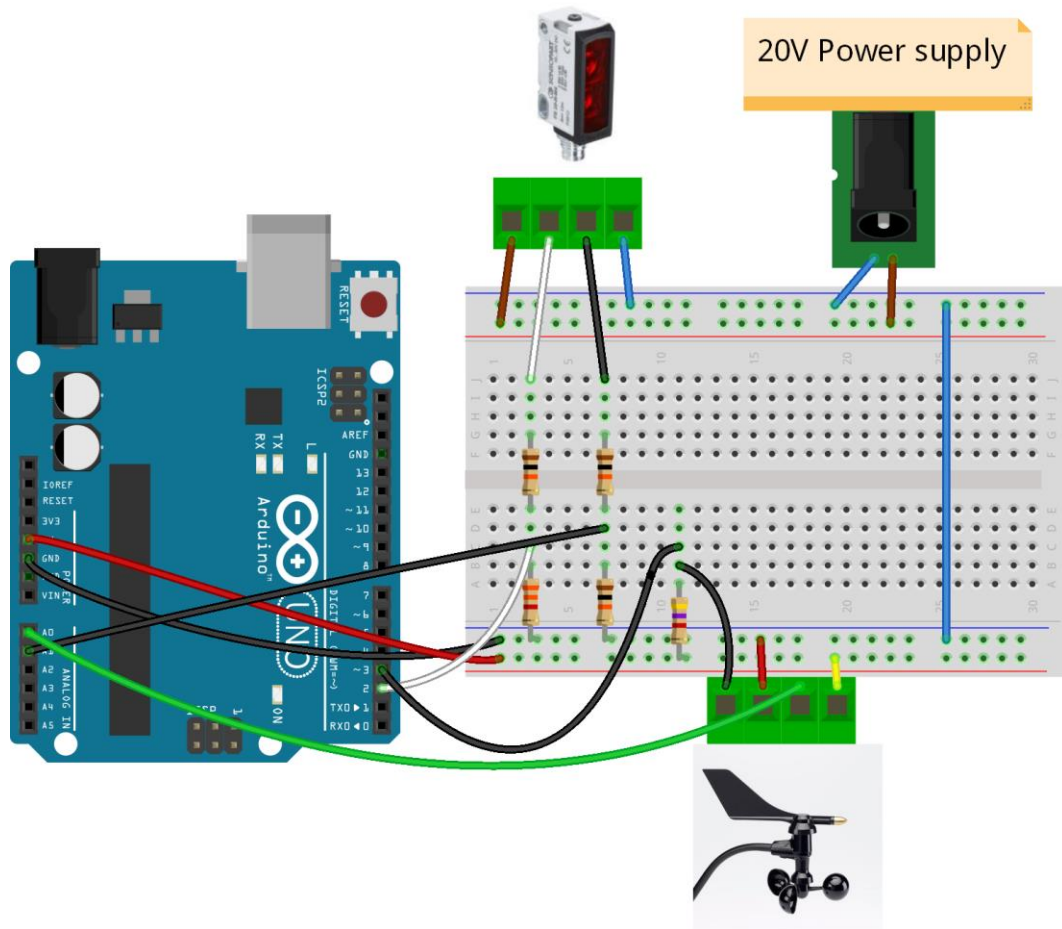


Figure 19. Arduino connections with distance sensor and anemometer. Illustration created with Fritzing.

To measure distance, the code simply gets the analog value from 0 to 1024 without any modification. This value is processed later in the post-processing phase.

Anemometer DAQ

Before continuing with the explanation of the Arduino code, the output signal of the anemometer is explained. According to the datasheet, the anemometer has four I/O signals:

- Potentiometer supply voltage (yellow)
- Wind direction potentiometer wiper (green)
- Ground (red)
- Wind speed contact closure to ground (black)

As can be deduced, the wind direction sensor is a potentiometer (which can be fed at 5V), and the wind speed sensor gives a 0-voltage pulse every revolution.

However, the wind speed sensor requires a pullup resistor to not cause false triggers. The resistor sets the input pin to HIGH. Each pulse the voltage drops to 0, as the 'wind speed contact closure to ground' pin is connected to ground in each pulse.

At this point, it is possible to identify that there is an analogy between the optical sensor and the anemometer. Indeed, the rotational speed meter works in the same way as the wind speed meter, and the distance meter works like a potentiometer, which is the wind direction meter. Therefore, the codes for both sensors are the same, but changing the conversion to real units.

When the values from each sensor are ready, they are sent through the serial port (USB) to the computer, where LabVIEW reads it using VISA. To identify which values come from the optical sensor and which ones from the anemometer, the separator for the optical sensor package is a space and the separator for the anemometer package is a comma. The implemented LabVIEW code, which can be seen in Appendix J, distinguishes between these two separators and the data is collected into two different files, one for each sensor.

In this way, the desired sampling frequency can be reached. The sampling frequency for the optical sensor has been set to 100Hz, although in the practice it varies between 80Hz and 120Hz because of Arduino and, mainly, LabVIEW processing times.

The sampling frequency of the anemometer has been set to 3Hz, not for software limitations, but for sensor limitations. According to the datasheet, 1Hz corresponds to 1m/s, approximately. If the wind speed is lower than the half of the sampling frequency, errors in the measurement can be produced. For example, if the wind speed is 1m/s and the sampling frequency 3Hz, it means that the sensor updates every second, but the data is acquired three times a second, what would mean that the wind speed appears to not change during a second, but it can do. So, the spectrum below the half of the sampling frequency (Nyquist theorem) is wrong. Higher sampling frequencies would mean bigger error, and at higher wind speeds.

In relation with false triggers, a debouncer has been implemented in the Arduino code. In the transition between opening or closing a physical contact, it can happen that in the limit between both states are generated multiple LOW and HIGH signals. This phenomenon is known as bouncing. To debounce the rotational and wind speed meters, the rising signals closer than 15ms from the previous signal, are disregarded (it would correspond to a rotational speed of 1333rpm or a wind speed of 67m/s)

Electronic load DAQ

As mentioned before, the electronic load already includes a DAQ hardware. However, its communication standard is TTL. To be able to connect the electronic load to the computer, a USB-TTL converter is needed. Fortunately, Arduino-based microcontrollers use TTL standard for serial communication, and they incorporate an USB-TTL converter to communicate with the

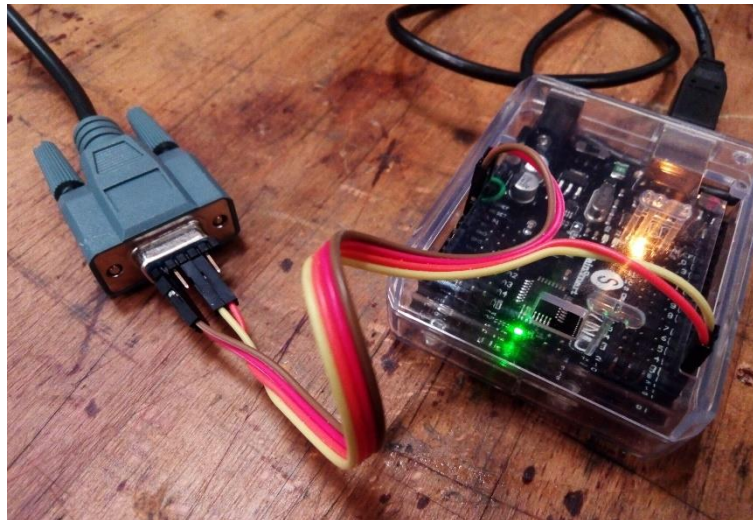


Figure 20. USB-TTL converter

computer. This converter can be set to work independently by connecting the RESET pin to ground (Green cable in Figure 20).

Solving the problem of the standard is only halfway to communicate with the electronic load. The electronic load uses a specific¹¹ communication protocol, and this has to be read by the LabVIEW program. Therefore, LabVIEW instrument drivers are presented. According to National Instruments, an instrument driver is a set of software routines that control a programmable instrument. Instrument drivers simplify instrument control by eliminating the need to learn the programming protocol for each instrument [12]. In the practice, instrument drivers are a set of VIs that contain instructions written in the instrument communication protocol. Fortunately, there exist instrument drivers for the electronic load used in this project, the Array 3711A. Without these instrument drivers the control of the electronic load from the computer would have been impossible for time reasons.

Strain gage amplifier DAQ

As said before, the strain gage amplifier could not be acquired. However, its implementation into the DAQ system would have been easy because the manufacturer provides an instrument driver for LabVIEW.

3.2.4. Post-processing

The DAQ system is already prepared to acquire data. However, as said before, it is needed to filter the distance measurement from the rotational speed auxiliary component disturbances. Besides, the sampling rate is non-uniform. The sampling rate from the electronic load and the anemometer present negligible variations and they can be assumed constant. The optical sensor, however, presents sampling rates between 80 and 125 Hz, which cannot be assumed constant.

The post-processing code is shown in appendix H. The results can be seen in Figure 21.

A perfect method to resample the non-uniformly sampled data could not be found. The procedure followed has been to resample the data to a constant sampling rate, using the MATLAB function ‘resample’, and afterwards the resampled data have been resampled again to a specific sampling rate (65Hz) using the MATLAB function ‘interp1’, which interpolates between two values.

With this procedure, the time series before and after do not present any visual difference, but the frequency spectrum is altered. The workaround for this problem is to use the raw data when plotting the spectrum.

Finally, the post-processing code saves all processed data in a CSV (Comma Separated Value) file, which is readable by Pdap (Python Data Analysis Program). Pdap is a program for post-processing, analysis, visualization and presentation of data [13], especially designed for wind turbines. The graphs presented in chapter ‘5. Model of the wind turbine with HAWC2’ are created with Pdap.

¹¹ Although many electronic load manufacturers use very similar protocols.

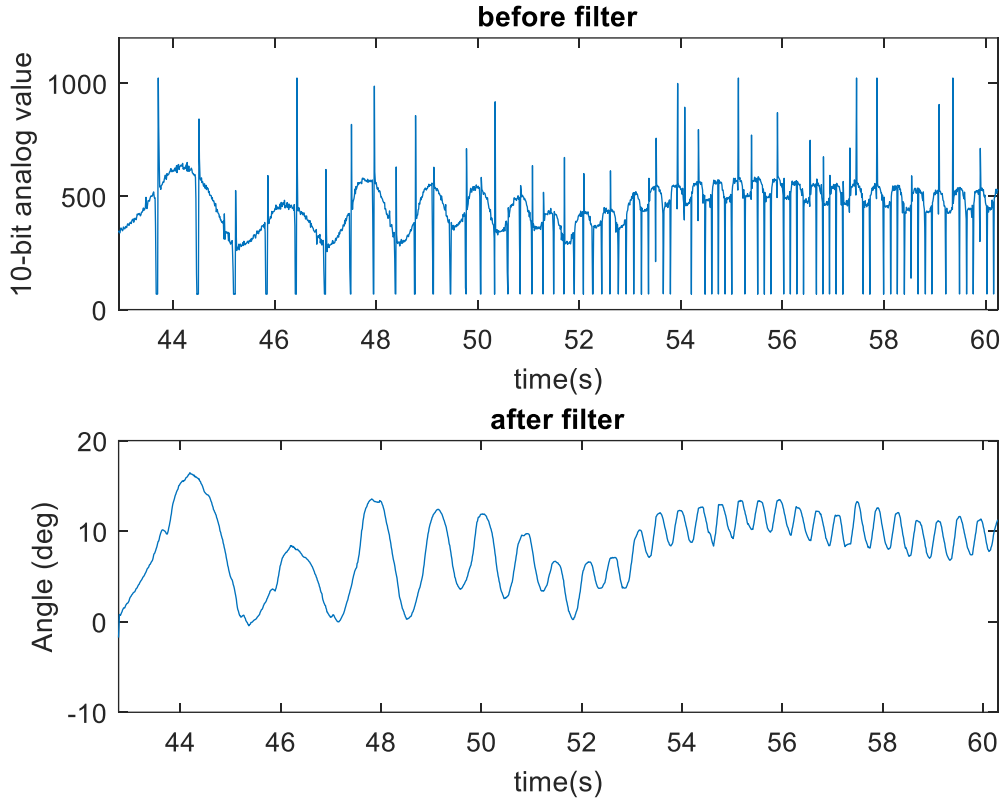


Figure 21. Before and after filtering the disturbances in the pitch angle measurement.

3.2.5. Generator control

So far, it has been exposed the instrumentation part of the instrumentation and control system. The control sub-systems in Figure 12 are the generator and brake systems.

The brake is activated manually. It is not a regulable brake, i.e. it has only two positions: on and off. Therefore, it cannot be used to influence in the performance of the wind turbine, only for stopping the wind turbine. When there is no power on the brake terminals, the brake is braking, so there is no risk in case of power shortage.

There are no active pitch nor active yaw systems. So, the main system in the control system is the generator. The generator, as said before, is a PMSG. The power delivered from a synchronous generator depends on the impedance of the load it is feeding. Therefore, the generator can be regulated by regulating the load impedance.

Before explaining the methods for controlling the load, more information about the operation of the PMSG is given. In a PMSG, the back emf (back electromotive force) is proportional to the rotational speed. Assuming the voltage drop in the synchronous impedance (synchronous reactance + armature resistance) is small, the voltage in the terminals is proportional to the rotational speed. The current is proportional to the generator torque. Figure 22 shows the per-phase equivalent circuit in the armature.

Therefore, assuming no losses, the generated power can be expressed as in Equation 3.

$$P = M_{gen}\omega = IV \quad (3)$$

Where M_{gen} is the generator torque, ω the rotational speed, I the current and V the voltage.

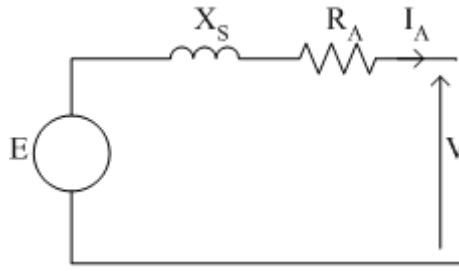


Figure 22. Equivalent circuit of a synchronous generator. E is the emf, Xs the synchronous reactance, Ra the resistance in the armature, and V the voltage between the terminals.

The generator characteristic for this kind of generators is given by Equation 4.

$$M_{gen} = \begin{cases} k_{opt}\omega^2, & \omega \leq \omega_{rated} \\ \frac{\omega_{rated}}{\omega} \cdot M_{gen,rated}, & \omega > \omega_{rated} \end{cases} \quad (4)$$

Where k_{opt} is a constant implicit in the generator, that has been set in the design phase, and depends on the rotor characteristics and the efficiency of the generator.

For the case of below rated rotational speed (ω_{rated}), the torque curve is such that the optimal torque is given for each wind speed. For the case above the rated rotational speed, the curve is the result of keeping the power constant. To keep the power constant, if the rotational speed increases, the torque has to decrease accordingly. There is only one optimal torque for each wind speed. Figure 23 presents the power output from the generator if the wind speed is kept constant and the load connected to the generator is varied. Indeed, the generator characteristic below rated rotational speed defined in Equation 4 is actually a curve that follows the MPP (Maximum Power Point) for each wind speed. The generator does not follow the MPP automatically, but needs to be controlled externally (with the connected load, as said before).

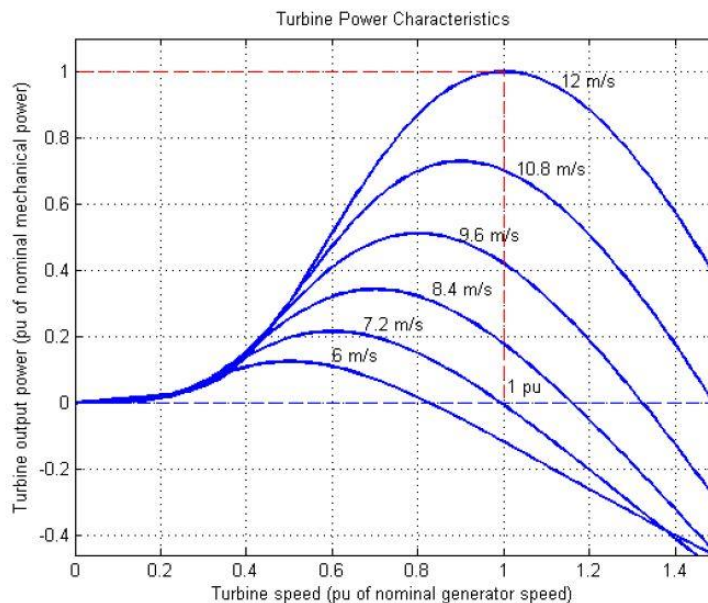


Figure 23 Power output for different wind speeds and loads. Source: [16]

A way to regulate the load electronically is by using a Boost¹² converter (Figure 24). Boost converters are DC-DC converters that increase the output voltage by decreasing the output current (so, the power is conserved). The output voltage varies in function of the duty cycle. The duty cycle is the fraction of time the transistor is closed.

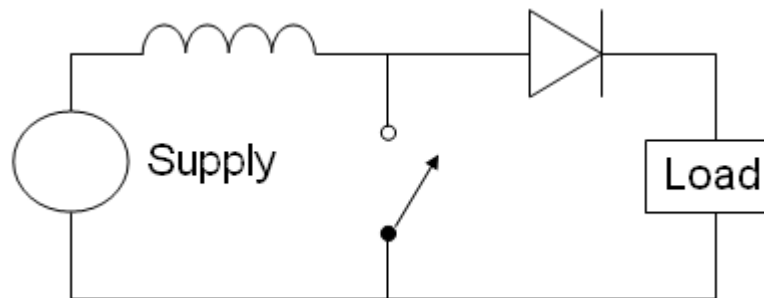


Figure 24. Boost converter. Source: [14]

From the point of view of the supply, when the transistor is open, the load that it can ‘see’ is the real load, but when the transistor is closed, the load is 0. Therefore, the ‘apparent’ load seen from the generator depends on the duty cycle of the transistor. The transistor can be controlled by PWM (Pulse Weight Module) with a controller.

This technique is based on DC. The generator is an AC dual 3-phase stator winding. It means the AC has to be converted into DC by using a 3-phase rectifier¹³ (AC-DC converter). Furthermore, the stator windings can be connected in series or in parallel. They have been connected in parallel to reach lower voltage levels: more safety in expenses of sacrificing some performance and the need of two rectifiers.

Electronic load

The only feasible option in this project to control the generator is to use an electronic load. The other considered options are described in Appendix D. Electronic loads, also called programmable loads, are lab instruments that, using the principle of the DC-DC converters explained before, can vary their impedance as desired. These devices are very expensive, but they provide many advantages:

- They are fully programmable
- The input variables, voltage, current resistance or power, can be measured and logged.
- Already include all kind of protection, such as overtemperature, overvoltage, overcurrent, overpower and power fail.

A DC electronic load has been chosen that fits the wind turbine, the 1kW Elektro-Automatik EL 9200-35 B HP 2U. This electronic load has the advantage that does not need a computer to control the generator, since it includes a function where the generator characteristic curve can be inserted. It also includes an MPPT function. However, this function is expected to not work in the field, since it is very slow.

A clarification about MPPT is given: there are three different MPPT algorithms that can be implemented in a SWT [15]:

¹² It can be also used a Buck or a Buck-Boost converter

¹³ The rectifier used is the VUO36-14NO8.

- Based on the power curve characteristic¹⁴
- Based on the optimal tip speed ratio
- Perturb and Observe (P&O)

When the parameters of the wind turbine are not known, P&O is the only algorithm that can be used. This algorithm works by making small variations in the control variable and checking if the output has decreased or increased.

Some studies approve the performance of the P&O algorithm in SWT, such as [15], [16] or [17]. However, these studies are based on wind tunnel tests. From the enbreeze experience, this algorithm does not perform well in field because of the wind fluctuations. The speed at which this algorithm can work is limited for the inertia of the rotor: changes are not instantaneous. P&O is still useful if, for example, it is desired to compare the numerical model power curve with the actual power curve, in a wind tunnel.

The EL 9200-35 B HP 2U could not be purchased for budget reasons, but another DC electronic load provided by enbreeze GmbH has been used instead: the 300W Array 3711A (Figure 25).



Figure 25. Array 3711A. Source: [18]

As only 300W could be delivered to the electronic load, the linkage configuration of the passive pitch system has been modified to pitch out at 300W, instead of 500W.

It is noteworthy to say that there also exist AC electronic loads. However, AC electronic loads are single phase devices. Therefore, 3 AC electronic loads (which include 3-phase functions) would have been needed, since the generator is 3-phase. The advantage of using AC electronic loads is that they also include a reactive load, therefore the reactive power can be compensated.

In the configuration used in this project, the reactive power is not compensated in any way. Fortunately, it is so small that it does not make any damage. In wind farms using synchronous generators, two ways of compensating the reactive power are used [19]:

- If the generator has excitation circuit, the reactive power compensation is done from this element.
- If the generator is a PMSG (this case), the compensation is done from the frequency converter.

Indeed, frequency converters can compensate the reactive power by using rectifiers for power factor correction [20].

¹⁴ This is the chosen algorithm. Its implementation is detailed in section ‘4.1. Wind tunnel outlet’.

3.3. Designing the bending moment sensor

In order to sense the loads acting on the blade root, strain gages are needed. In a principle, strain gages can be placed on the blade. There are special strain gages for composites that adapt to the particular properties of these materials. However, in this case the blade is too stiff. That's why it is decided to install a multicomponent force and moment sensor right below the blade root.

Preliminary step

Prior to the design of the sensor, provided that the centrifugal forces are much bigger than the other components, a calculation of the crosstalk in a commercial model has been done. Crosstalk, when talking about force and torque sensors, can be defined as the effect from loads (parasitic loads) in different components (influencing components) in the measurement of a certain component (affected component). That is under the hypothesis that strain gages are well arranged to feel only one component in a specific channel. Sources of crosstalk are the deformation of the material in transverse directions due to Poisson effect [21], or inaccuracies in the manufacturing process [22]. Crosstalk effect use to be between 1% and 5% [23], and it is determined experimentally, this is the reason why a preliminary calculation with a commercial sensor is done.

The multicomponent sensor HBM MCS10-BG1, shown in Figure 26, has been chosen for being an accurate sensor and having a good definition of the crosstalk and other sources of errors in its datasheet.



Figure 26. HBM MCS10 multicomponent sensor. Source: [51]

Given the nominal forces (F_{nom}) and moments (M_{nom}) of the sensor, the values in percentage of crosstalk (XT) expressed as decimal, and the external forces and moments actuating on the sensor, the crosstalk uncertainty (U_{XT}) can be calculated as in Equation 5.

$$U_{XT,i} = \sum_{j \neq i}^6 XT_{i,j} \frac{F_j}{F_{j,nom}} F_{nom,i} \quad (5)$$

Where i is the affected component and j the influencing component. For simplicity, F represents indistinctly forces and moments.

It is remarkable to say that the external forces are not the maximum forces, but the forces that give most unfavorable results. For example, the tangential force to the rotor plane, F_x , is not much dependent on the wind speed. Therefore, the normal force F_y will be affected more by F_x when F_y is small than when it is big. The chosen values of the external forces are, then, the most

unfavorable in the interest zone, which is the range of wind speeds where the pitch system is acting. These values are shown in Table 1.

Table 1. External forces and moments on the blade root.

	x-axis	y-axis	z-axis
Force (N)	40	115	1260
Moment (Nm)	28	2	0.3

Equation 5, however, shows the uncertainty in Newtons. In order to know to what extent the actual measurement is affected, the crosstalk error in percentage ($\epsilon_{XT}(\%)$) is presented in equation 6.

$$\epsilon_{XT,i}(\%) = \frac{F_{real,i} - F_{meas,i}}{F_{real,i}} \cdot 100 = \frac{U_{XT,i}}{F_{real,i}} \cdot 100 \quad (6)$$

Table 2 shows the calculated crosstalk error for a MCS10-BG1. The component that most contributes to the crosstalk is in all cases the centrifugal force (F_z), so the concern that motivated this study is now evidenced.

Table 2. Crosstalk error for each relevant component

	F_x	F_y	M_x	M_y
$\epsilon_{XT}(\%)$	49.8	16.7	1.9	45.5

Crosstalk can be reduced with the calibration matrix method, also called matrix compensation method. This post-acquisition¹⁵ method is based on a series of coefficients that indicate how much an influencing component influences the affected component. The coefficients are obtained experimentally by varying an influencing component and keeping the other components constant. Regrettably, to use the calibration matrix method, the influencing components have to be measured. That would increase substantially the number of channels needed to be read in parallel, increasing the cost of the project to unaffordable levels.

Hence, as a DIY sensor is not expected to be more accurate than a commercial proven fine-tuned sensor, the only component that can be read with an acceptable error is the flapwise¹⁶ bending moment M_x .

In addition, there are other uncertainties apart from crosstalk. The MCS10-BG1 datasheet includes the most common error sources:

- Relative zero signal error
- Temperature effect
- Linearity deviation
- Relative reversibility error
- Relative creep over 30 min.
- Relative standard deviation of repeatability

¹⁵ There exist commercial products that integrate matrix compensation in the sensor board.

¹⁶ Referred to the blade coordinate system.

These errors have been calculated, leading to the total error¹⁷ ($\epsilon_T(\%)$), including crosstalk, shown in Table 3.

Table 3. Total error for each relevant component

	F_x	F_y	M_x	M_y
$\epsilon_T(\%)$	56.5	18.4	2.7	52.8

Comparing Table 3 with Table 2, it is demonstrated that the biggest source of error comes from the crosstalk.

Design of the mechanical component

The design of the bending moment sensor has been inspired in actual products. There is a wide variety of force sensors, as seen in Figure 27. Although it is going to be a bending moment sensor, the design is planned to be expandable to multicomponent sensor by attaching more strain gages.



Figure 27. Variety of load cells and force sensors. Source: [24]

There are two main types of multicomponent sensors. The one shown in Figure 28, and the one shown in Figure 29, also known as ‘pancake’ multicomponent sensor, for its flat shape. The choice of one or other type depends on the desired geometry. As the blade root diameter is relatively small, the type in Figure 28 is chosen. In fact, that specific component is the final design of the mechanical part of the sensor.

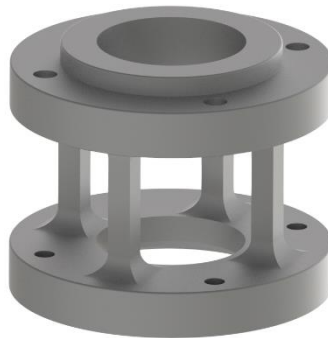


Figure 28. Multicomponent sensor

¹⁷ Note that the total error is calculated as $\epsilon_T = \sqrt{\sum_j^n \epsilon_j^2}$, which is different from the maximum error: $\epsilon_{max} = \sum_j^n \epsilon_j$.

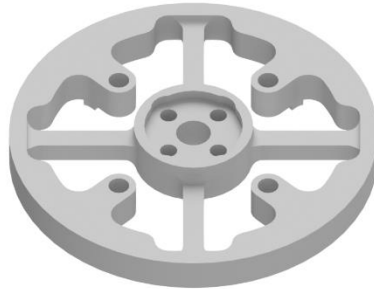


Figure 29. Pancake multicomponent sensor

The next step has been to give the foot and the top of the sensor the appropriate shape to be attached to the blade root and the hub, with its corresponding centering. Subsequently, the size of the columns has been dimensioned. The initial size has been set to 6x6x25mm, because of the size of the acquired strain gages.

With the initial shape, a stress analysis with Autodesk Inventor has been conducted, using the general-purpose Aluminum 6061-T6 as material, the same external forces as for the commercial sensor, applied on the surface in contact with the blade root, and blocking the movement in the surfaces in contact with the hub. The stress analysis in Inventor uses the Finite Element Method (FEM) for solving the stress and deformation problems. A fine mesh of finite elements with an average element size of 0.02 relative to the bounding box length has been generated and, before running the simulation, the number of local refinements has been set to 5 and the stopping criteria to 1%. It means there should be less than 1% difference between two consecutive solution steps to end the simulation.

Figure 30 shows the equivalent strain resulting from the stress analysis. In the beam suffering most deformation, there is a tension strain of around $4e-4$ m/m or, a more common pseudo-unit used in strain gages datasheets, $400\mu\epsilon$ (microstrains). However, the other side is not symmetrical, because of the centrifugal force. In the other side there is only $100\mu\epsilon$.

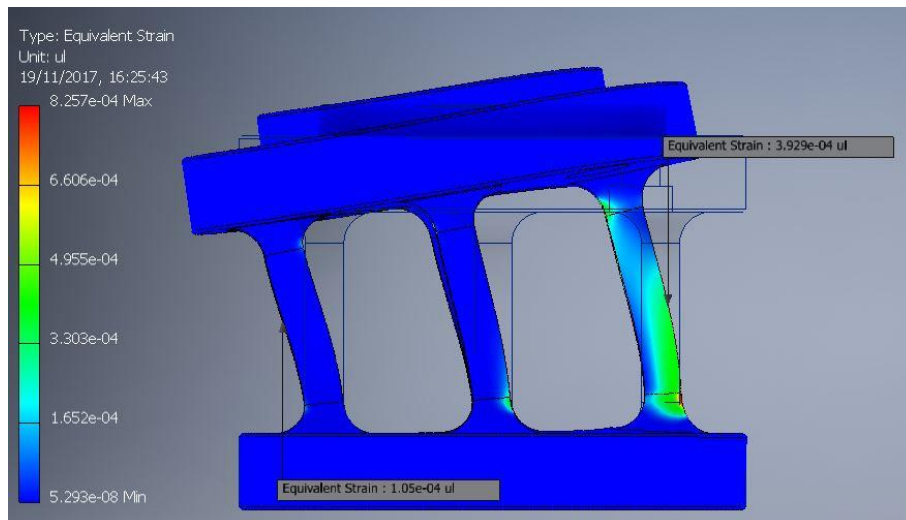


Figure 30. Strain values from the stress analysis for the bending moment sensor. 'ul' means unitless.

Figure 31 shows the component deformation if there were only bending moment. Both sides are antisymmetric. That is the strain the strain gages feel if they are correctly arranged, and it corresponds to $250\mu\epsilon$.

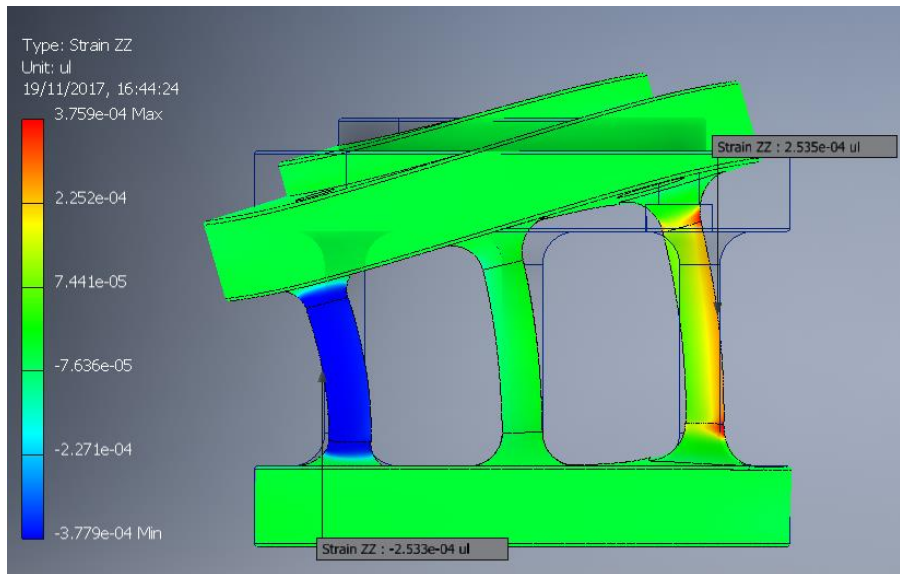


Figure 31. Strain values from the stress analysis for the bending moment sensor under pure bending moment.

The gage factor (GF) is defined as in Equation 7, and it determines how much varies the strain gage resistance in function of the strain, i.e. it determines the sensitivity. A common value for the gage factor is $GF = 2$. It means that if the microstrains are $250\mu\epsilon$, the output is 0.125mV/V for a single strain gage. For a full-bridge configuration (explained in the next step: ‘Design of the electric configuration’), the output is roughly four times bigger: 0.5mV/V . The minimum value of nominal sensitivity for the acquired data acquisition system is 2mV/V . The value 0.5mV/V is enough¹⁸, but the ideal would be to reduce the thickness of the columns in order to reach values closer to 2mV/V . But, as said before, the minimum thickness of the columns is limited by the size of the strain gage.

$$GF = \frac{\Delta R/R_0}{\Delta L/L} \quad (7)$$

Regarding the material, the component suffers a maximum stress of 57 MPa , which is lower than the yield strength¹⁹ of the material. To ensure that the component won’t break, a further fatigue analysis needs to be done. Using other aluminum alloys, the strain would be similar, because the Young modulus of aluminum alloys is always around 70 GPa , so the strain in function of the applied forces for the same component geometry would be similar.

Another material common in force sensors is steel. *Ceteris paribus*, the strain would be $83\mu\epsilon$, because the Young modulus is the triple. That means steel would be adequate for higher external forces, because the strength is also the triple, but for this case it is better to use aluminum.

So, the initial size is good, but it could be improved by buying smaller strain gages or moving the columns to the center. However, the first option is discarded due to the cost, and the second is discarded because of the increment of weight that it would imply.

¹⁸ For a 16-bit resolution, there are 16384 values between 0 and 0.5mV/V .

¹⁹ Yield strength is the stress where plastic deformation begins. It is desired to work only in elastic deformation. According to Inventor, the yield strength of Al6061-T5 is 275 MPa .

Design of the electric configuration

At this point, the strain gage bridge can be implemented. Strain gages resistance variation is very small. In order to measure very small resistance variations, a Wheatstone bridge (Figure 32) is used. Wheatstone bridges can be quarter-bridge, half-bridge and full-bridge. Quarter and half-bridge have 1 and 2 strain gages, respectively, and the rest are dummy resistors²⁰. The advantage of these two configurations is a lower cost, for using less strain gages. Quarter-bridge, however, needs temperature compensation. Half and full-bridge are not affected by temperature effect because the Wheatstone bridge measures resistance variations, and the thermal expansion or contraction acts equally on all strain gages, assuming they are all at the same temperature.

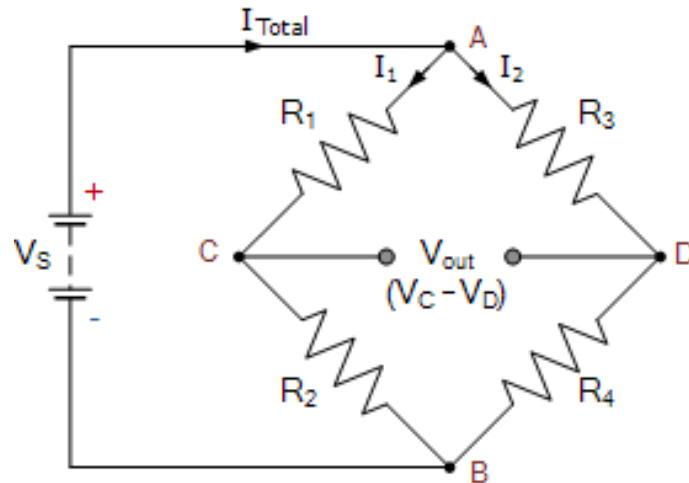


Figure 32. Wheatstone bridge. Source: [25]

The advantage of full-bridge is that it has the double of sensitivity than half-bridge. In the previous step it has been said that the output from the Wheatstone bridge is expected to be 0.5mV/V at nominal bending moment. If that value were higher than 4mV/V , it would not make sense to use full-bridge, because the half-bridge would output 2mV/V , which is the nominal sensitivity of the DAQ system.

A full-bridge is then, the best option. The next step is to choose the location of the strain gages. They have to be arranged in a way that they feel only bending moment, and as much as possible. It is obvious that the locations have to be in the two columns with maximum tension and compression. It is less obvious the choice of using shear strain gages on the side or normal strain gages on the front. Figure 33 shows that the shear is very low. Therefore, normal strain gages in the fronts are chosen.

²⁰ Also called completion resistors

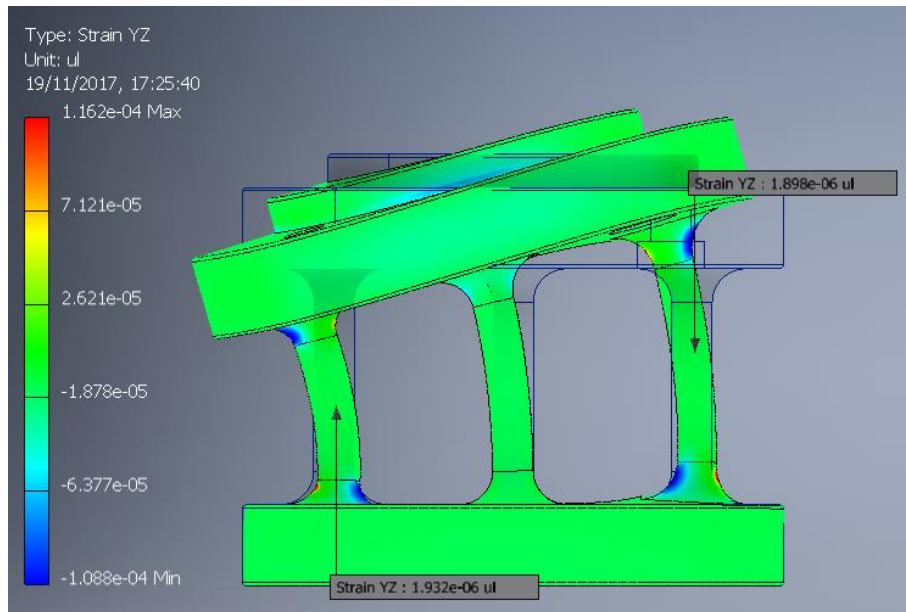


Figure 33. Shear strain values for the bending moment sensor under pure bending moment

The location of the strain gages, following the numbers in Figure 32, is shown in Figure 34. The Wheatstone bridge can be seen as two voltage dividers in parallel. In this case both voltage dividers have the same resistances but distributed differently: R1 has a lower voltage drop than R2 because the first is in compression and the second in tension. In that way, in the point V_C is reached maximum voltage and in the point V_D is reached minimum voltage. The output is the difference between V_C and V_D .

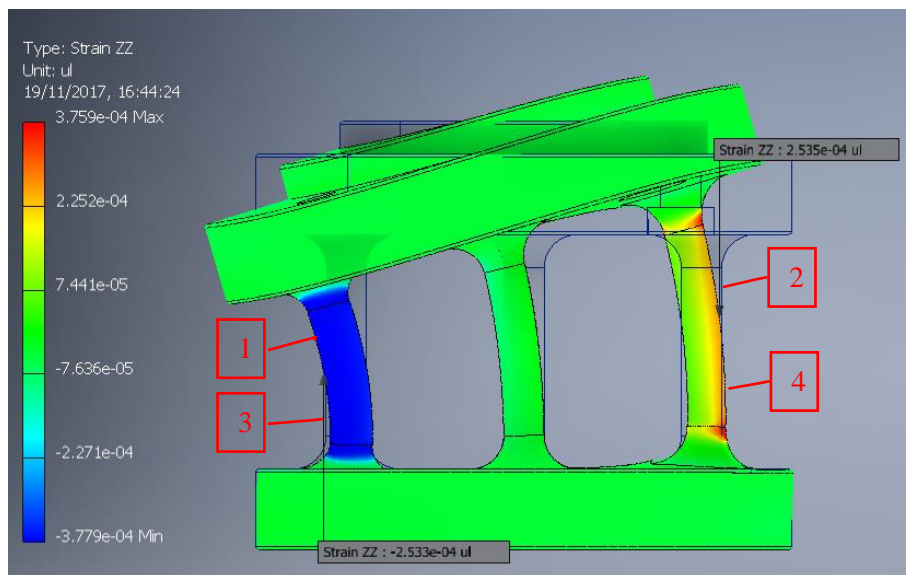


Figure 34. Location of the strain gages for the bending moment sensor. All are oriented equally, in vertical position.

The last step would be to check that other components do not influence the measurement. This blade plus sensor system can be seen as a cantilever beam, which is a well-known case. See [26] for more details. The thrust torque sensor, nonetheless, is not in the same situation, and this step will be necessary.

3.4. Strain gages on the thrust-torque sensor

The thrust torque sensor is an already existing component which only lacks the strain gages. It can be seen in Figure 35²¹. In Appendix C is presented the procedure followed to attach the strain gages to the component. But, before, the strain gage configuration needs to be calculated.



Figure 35. Thrust-torque sensor in its location in the hub.

The thrust-torque sensor, which is a pancake multicomponent sensor with only two channels (force and moment in the axial direction), cannot be regarded as a cantilever beam, but as a fixed-roller beam in the 3 planes, being the columns fixed-fixed beams, because there is a steel component surrounding it on its external perimeter.

Figure 36 shows that the thrust torque sensor strain under external loads at rated power is very low. Running a stress analysis with isolated loads for thrust and torque is found that the biggest deformations are caused by shear stresses. These deformations are still very low, $53 \mu\epsilon$ and $25 \mu\epsilon$ for torque and thrust, respectively, as shown in Figure 37 and Figure 38.

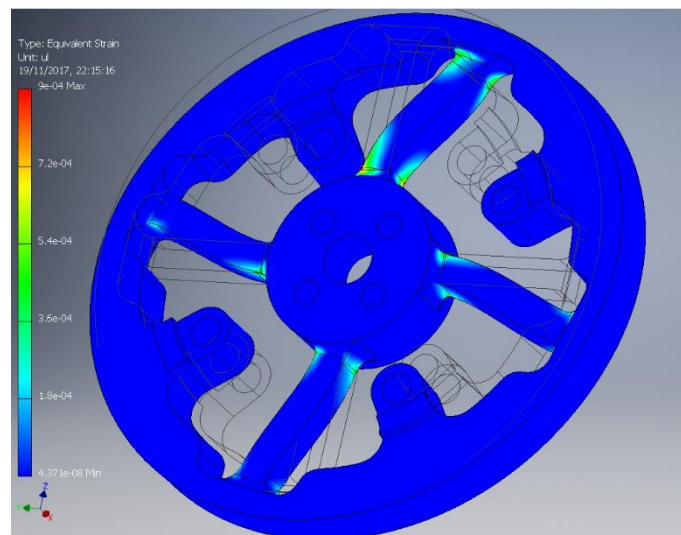


Figure 36. Thrust torque sensor strain under external loads at rated power.

²¹ However, there are some differences between the real part and the received CAD model, but these are not relevant for the final results.

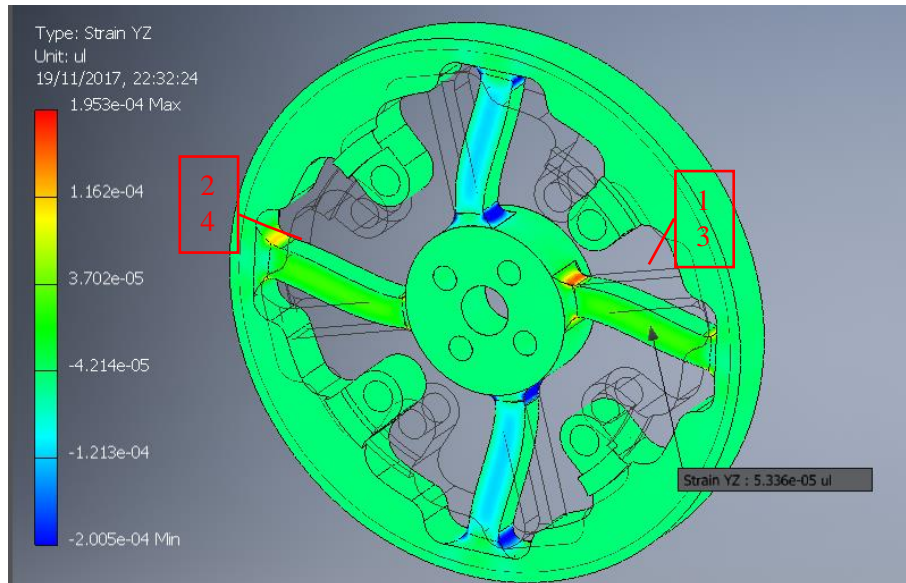


Figure 37. Strain caused by shear stress under torque. Strain gages locations numbered in red.

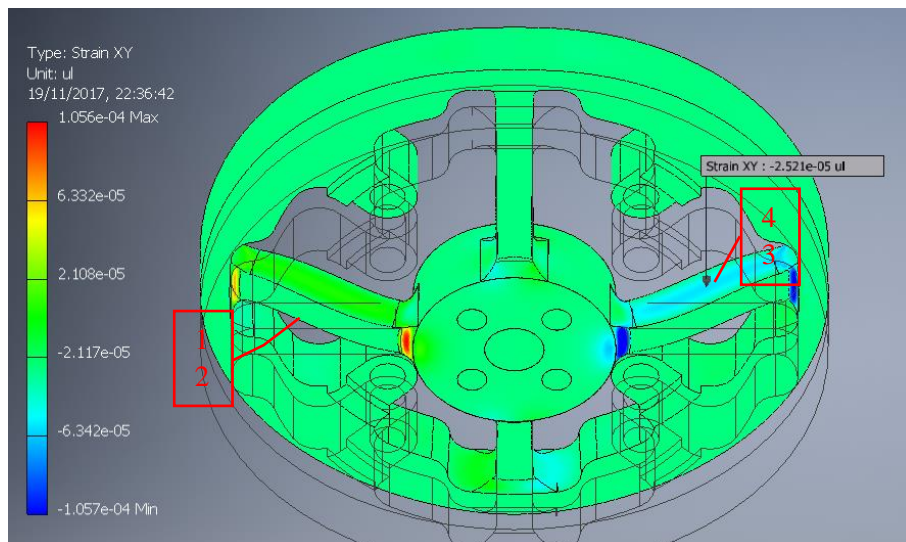


Figure 38. Strain caused by shear stress under thrust. Strain gages locations numbered in red.

To measure shear stress, shear strain gages are needed. Shear strain gages are normal strain gages twisted 45° , so when there are two of them arranged perpendicularly, one gets compression and the other tension. Figure 39 illustrates this explanation.

The configurations of shear strain gages that isolate torque and thrust, following the Wheatstone numbering in Figure 32, are shown in Figure 37 and Figure 38, respectively. For the case of torque configuration, neither the thrust load nor the bending moments²² parallel to the YZ plane (Figure 40) cause any shear stress on the surface of the strain gages. They do the forces parallel to the YZ plane (Figure 41). For these forces, 2 and 4 are in tension and 1 and 3 in compression, so the voltage at C and T is the same, and then the output voltage is 0.

A similar reasoning can be done for the thrust configuration.

²² Note that the piece is symmetrical, so the bending moment in Y causes the same effect as the bending moment in Z. The same can be applied to the forces in Y and Z.

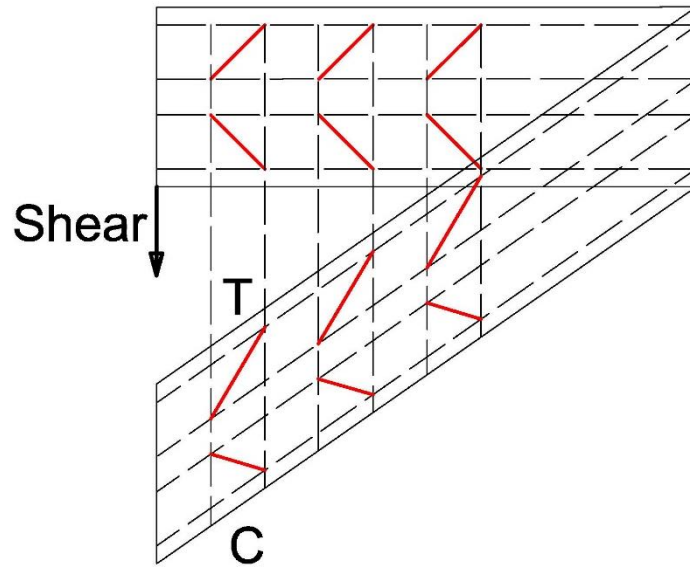


Figure 39. Shear strain gage under pure shear stress. T indicates the side under tension and C the side under compression after the shear stress is applied.

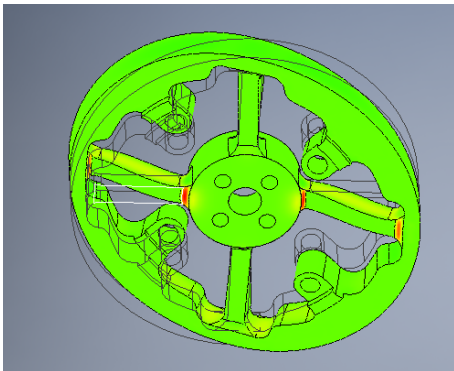


Figure 40. Moment parallel to the YZ plane

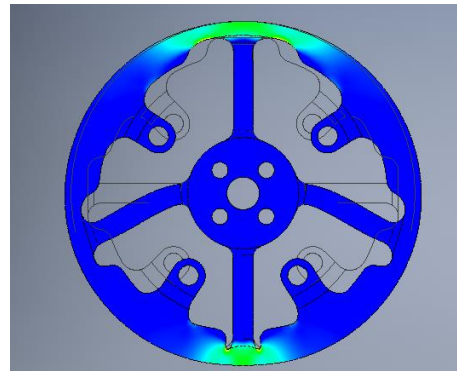


Figure 41. Force parallel to the YZ plane

This chapter has presented the design of the passive pitch system prototype, as well as the design of the instrumentation and control system. The hub has been designed with the same qualitative parameters as the one of the enbreeze wind turbine. The instrumentation and control system allows live monitoring of the wind turbine, as well as recording the data for a later comparison with the HAWC2 simulations. The implementation of both systems on the DTU SWT give a step to the realization of the tests, presented in the next chapter.

4. MEASUREMENT CAMPAIGNS

The wind turbine has been tested in two different sites: in a wind tunnel outlet in Lyngby campus, and in the test field of Risø campus.

4.1. Wind tunnel outlet

The wind turbine has been tested in a wind tunnel outlet, instead of in the test section, due to size reasons. The test sections in the wind tunnels of DTU are too small.

Wind flow quality

In the wind turbine output, which is shown in Figure 42, moderate wind speeds enough to test the passive pitch system can be reached. The problem of this wind source is the quality of the flow: the produced wind speeds present a high turbulence, which causes very low spatial coherence and present a big wind shear.

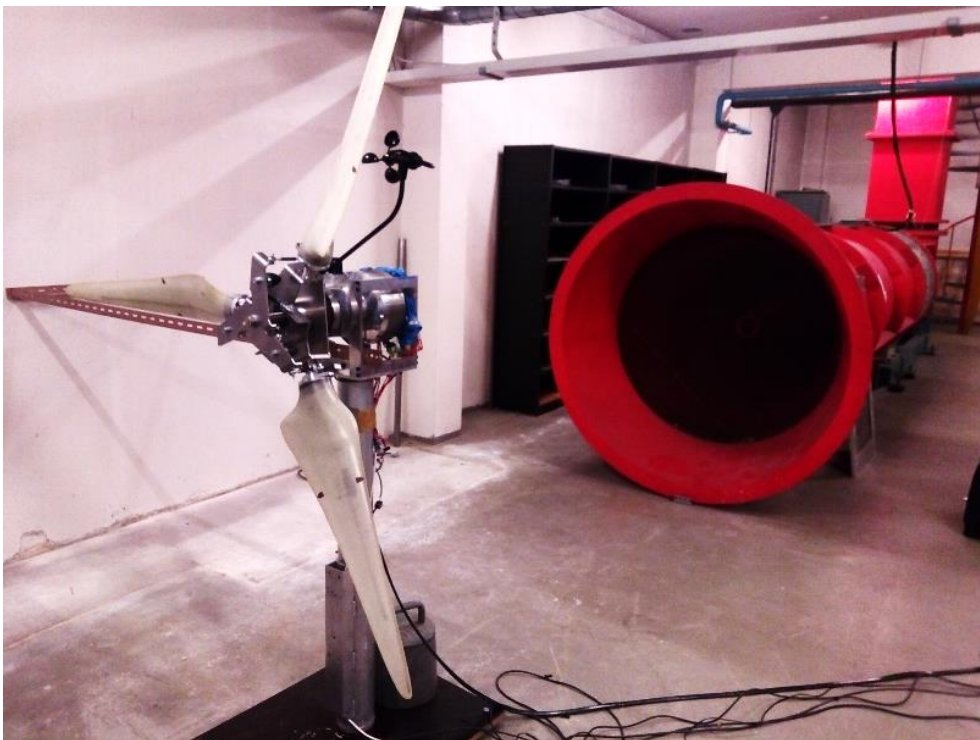


Figure 42. Wind turbine prepared for being tested in the wind tunnel outlet.

The spatial coherence has been tested *in situ* by using a portable anemometer placed a certain distance to the anemometer used for the measurements and comparing both wind speeds. Numerical results (time-series) from this test cannot be given because the portable anemometer cannot register data. However, another approach to demonstrate the low spatial coherence can be undertaken.

Figure 43 shows the spectrum²³ of the wind speed of a 1-hour dataset of an almost constant wind speed in the Risø test field. In this graph, it is also represented a theoretical Kaimal spectrum for the same mean wind speed and hub height as the datasets, 3.3m/s and 1.5m, respectively. The Kaimal spectrum describes the ideal shape of the wind speed spectrum in function of the mean wind speed and the hub height. There are several similar versions of the

²³ It is referred spectrum as the PSD (Power Spectral Density). The implemented code to obtain the PSD can be consulted in Appendix I.

Kaimal spectrum. The one represented corresponds to the non-dimensionalized u-component single-sided spectrum presented in the IEC-61400-1.

Figure 43 shows that the test field measurement diverges from the Kaimal spectrum substantially from 0.06 Hz to higher frequencies. This is not due to differences in the wind patterns. The reason of this divergence lies on the cup anemometer. Indeed, as already presented in section 3.2.1, cup anemometer measurements are affected by their inertia. Cup anemometers are especially bad for measuring turbulence due to their dynamic characteristics [27]. At the highest frequencies, the signal is mixed with white noise²⁴.

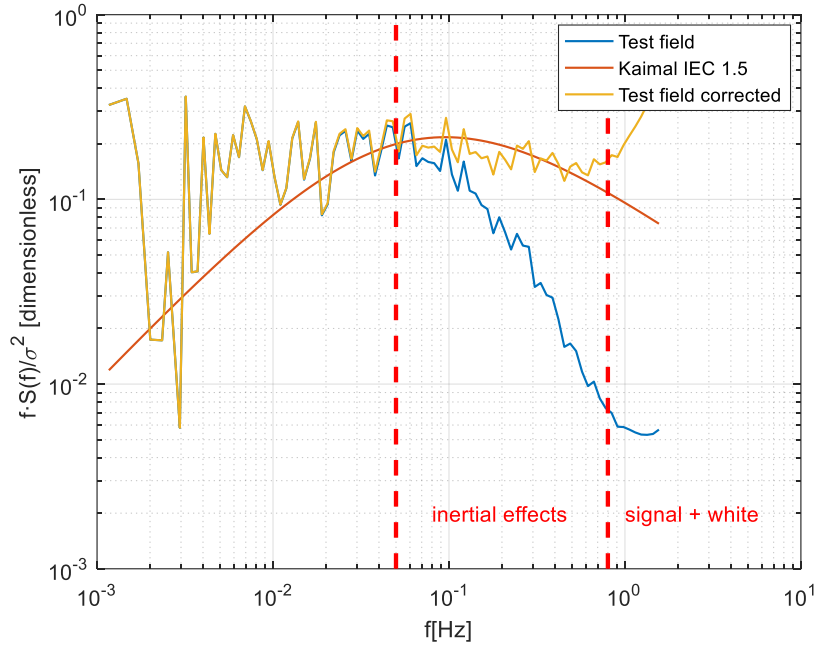


Figure 43. ‘Test field’:PSD of wind speed data collected in Risø at a mean of 3.3m/s influenced by the inertia of the anemometer. ‘Kaimal IEC 1.5’ Kaimal theoretical spectrum for 3.3m/s and a height of 1.5m. ‘Test field corrected’: same data as ‘Test field’ but the inertial effects of the anemometer are corrected.

Fortunately, Yahaya and Frangi presented a formula to compensate the cup anemometer response [27]. This formula can be seen in Equation 8.

$$P_c(\omega) = P_a(\omega) \cdot \left(1 + \frac{\omega^2 L^2}{U^2}\right) \quad (8)$$

Where P_c is the compensate PSD, P_a the measured spectral density, ω the pulsation, U the mean wind speed, and L the distance constant, expressed in Equation 9.

$$L = \frac{2I}{\rho C A r (l + \Lambda)} \quad (9)$$

Where I is the anemometer inertia, ρ the air density, C a first-order constant, A the effective cup area, r the rotor radius, l the response distance and Λ the characteristic instrument length scale [28].

As the parameters in Equation 9 are difficult to obtain, the distance constant has been found experimentally by matching the spectrum to the Kaimal theoretical spectrum, as recommended in [27], yielding a value of $L=3\text{m}$. Furthermore, the distance constant is an instrument constant [28], so it can be used henceforth to correct other spectra from the same anemometer. The result of this correction can be seen also in Figure 43.

²⁴ White noise is a random signal having equal intensity at different frequencies [59].

Figure 44 shows the corrected spectrum for both the test field and the wind tunnel outlet. The range where the white noise affects the measurements has been trimmed. As can be seen, the wind tunnel outlet presents more energy at higher frequencies, increasing the gap from the theoretical Kaimal spectrum. This is due to the high turbulence.

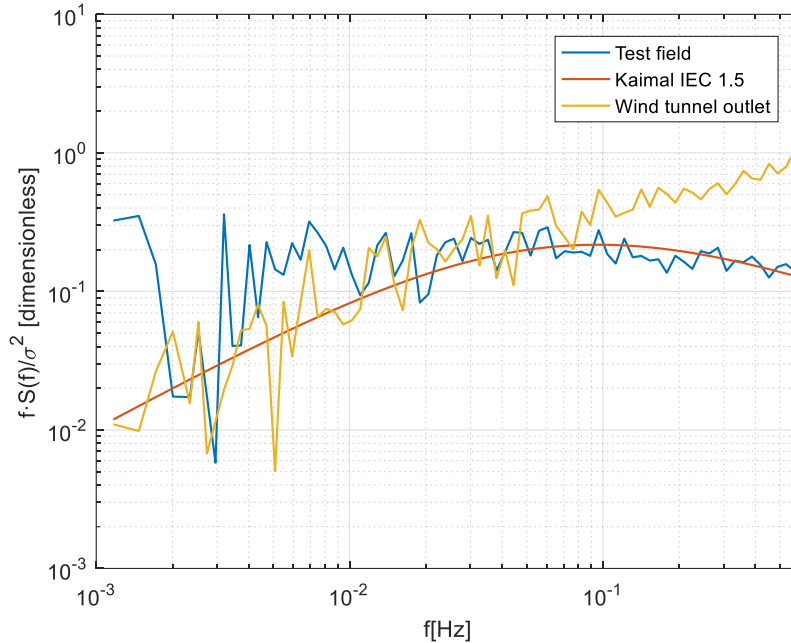


Figure 44. Corrected data for the Risø test field and the wind tunnel outlet.

As said by Davenport, spatial coherence (coh_{uu}) is related to temporal frequency (f) according to Equation 10. Therefore, wind speeds ‘blowing’ at higher frequencies present lower spatial coherence. A more intuitive interpretation is the following: eddies at higher frequencies are smaller, therefore, for two anemometers placed at the same distance, the ‘chance’ of an eddy to touch both anemometers is smaller [10].

$$coh_{uu}(f, \Delta z) = e^{-\frac{a(f\Delta z)}{U}} \quad (10)$$

Where a is a constant of order 8, Δz is the distance between two u components and U is the mean wind speed.

Figure 45 shows the time-series of the test field and wind tunnel output datasets. The test field series presents bigger ‘structures’ than the wind tunnel outlet. This is an indicator of a higher autocorrelated time series for the test field dataset, and it is in line with higher energy at lower frequencies. The shown data, however, nodes not include the correction for the anemometer’s inertia.

The problem with low spatial coherence is that the measurement of the wind speed becomes more inaccurate. But this inaccuracy goes beyond the concept of spatial coherence. The measured mean wind speed along the time presents big differences along the rotor plane. This can be defined as shear, but not in the way typically found in wind energy, where the wind speed increases gradually with the height. The shear presents an unknown shape. In fact, the majority of the measurements taken showed unrealistic values of wind speed: depending on where the anemometer was placed, the values were too high or too low. Therefore, the data from the anemometer in the wind tunnel outlet cannot be trusted.

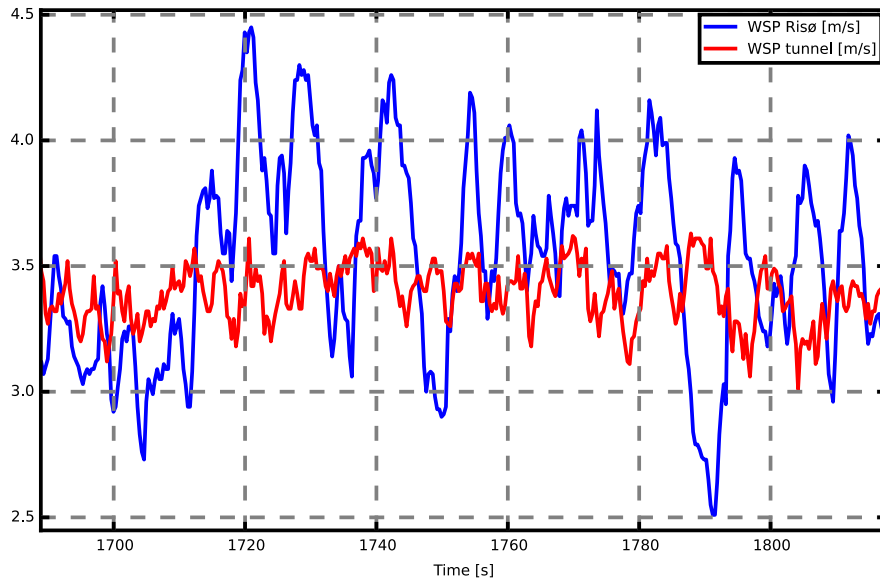


Figure 45. Time-series for Risø test field and wind tunnel outlet.

Nevertheless, the tests in the wind tunnel outlet have been very useful to check that the system works properly before testing in Risø test field, which is 40km away from the workshop.

MPPT algorithm

The wind tunnel outlet has also been useful to find the real optimal generator characteristic curve. The passive pitch system implied some changes, such as changing to downwind, adding a coning angle, and increasing the rotor diameter, as already mentioned in section ‘3.1. Integration of the concept on the DTU SWT’. So, the real optimal generator characteristic does not match anymore with the one found last year in the SWT competition.

Although what is desired to test is the passive pitch system, which works in the limitation zone, the power curve in the optimization zone is needed in order to be able to reach the limitation zone, and it is better if it is reached at the lowest wind speed possible. For example, if a too ‘optimistic’ power curve is used, the generator would slow down the wind turbine because the rotor cannot²⁵ produce that power for a specific rotational speed. On the other side, if a too ‘relaxed’ power curve is used, the passive pitch system would pitch out, for its implicit working principle. Nonetheless, as the objective of this project is not to produce energy, the abovementioned P&O MPPT method has not been implemented, but an acceptable generator characteristic has been found manually. This curve has been included later in the HAWC2 model, so this practice does not create any bias between the real and the numerical models.

To do so, for a certain wind speed, the maximum output power has been found by varying manually the output current. The time-series of this experiment can be seen in Appendix E. With only one optimal point, the generator characteristic can be found by knowing the rotational speed in that point, as can be deduced from Equation 4.

The found point featured the values shown in Table 4. Note that the torque is not straightforward to obtain²⁶. Although, as mentioned before, the wind speed indicated in the

²⁵ It can for some seconds, because the rotor is delivering the kinetic energy contained in the rotating parts when it is slowing down.

²⁶ The power, which is the product of the voltage and the current (Equation 1), is $P=100W$. From the combination of equations 1 and 2, the generator constant results to be $k=2.54e-3 \text{ Nm}/(\text{rad/s})^2$. However, in Equation 1 it has been assumed no losses. The measured power is actually the power in the terminals of the electronic load.

anemometer is not reliable, an approximate value of the wind speed value can be found. This value is found by comparing the measured power with the power in the HAWC2 simulation. A mechanical power of $P_{mec}=108W$ (value in Footnote 26), corresponds to an undisturbed wind speed of around 6m/s in the simulation results, as depicted in Figure 60, page 50. Therefore, the real average wind speed in the rotor area should be close to 6m/s.

Table 4. Approximate values of the found optimal point

<i>Parameter</i>	ω (rad/s)	V (V)	I (A)	θ_p (deg)
<i>Value</i>	34	25	4	0

The chosen MPPT algorithm, as advanced in section ‘3.2.5. Generator control’, is based on the power curve characteristic. It has not been chosen the MPPT based on the optimal tip speed ratio because of the need of a precise measurement of the wind speed.

The algorithm based on the power curve characteristic can be controlled from power or rotational speed as input. Rotational speed has been chosen due to its fast sampling frequency, and because the electrical power in terminals of the electronic load does not match with the mechanical power in the generator, as stated in Footnote 26.

From the programming point of view, the MPPT algorithm is a lookup table, which contains the generator characteristic curve. The implemented curve in the LabVIEW code is not M vs ω , but I vs ω . As current is proportional to torque, and the variable that the electronic load can control is the current, this variable was preferred for simplicity. The M vs ω curve is shown in Figure 62, page 51.

4.2. Risø test field

Some data from the test field has already been presented to correct the spectrum of the cup anemometer. A picture of the arrangement in the Risø test field can be seen in Figure 46.

The data acquired in Risø test field has been used to validate the HAWC2 model. Although quantitatively the results differed, as will be explained in chapter ‘5. Model of the wind turbine with HAWC2’, qualitatively, the passive pitch system behaved as expected.

The efficiency of the generator is unknown, but it can be approximated to $\eta=0.95$. The losses in the rectifiers are found in their datasheet, which for 2A (4A distributed into two branches with same impedance) they are 1.5W per rectifier. The losses in the cables can be assumed negligible. The accumulated losses are, therefore, 8W, which is the 8% of the measured power. The generator constant considering losses is $k=2.74e-3 \text{ Nm}/(\text{rad/s})^2$, which is closer to the actual generator constant $k_{opt}=2.87e-3 \text{ Nm}/(\text{rad/s})^2$.

This deduction evidences, by using the generator characteristic as indicator, that the measured power is not a good parameter to use to calculate the torque. Likewise, the calculated losses are not constant, but they depend on the output current, and this dependence is not known mathematically.



Figure 46. Arrangement in the Risø test field. The DTU SWT is shown in first plane, fixed to the ground with ropes and stakes. Behind, the electronic devices for live monitoring and controlling the SWT. The anemometer can be seen in the left side of the picture.

Figure 47 shows a fragment of this test with the system working below rated wind speed. Although the pitch angle must be 0, the turbulence makes the system to pitch out intermittently on a small scale. On the one hand, this behavior reduces the power output. On the other hand, the loads on the wind turbine are diminished. Nevertheless, the lost power for working in the partial load region is negligible, because the average pitch angle of the sample is less than 1 degree.

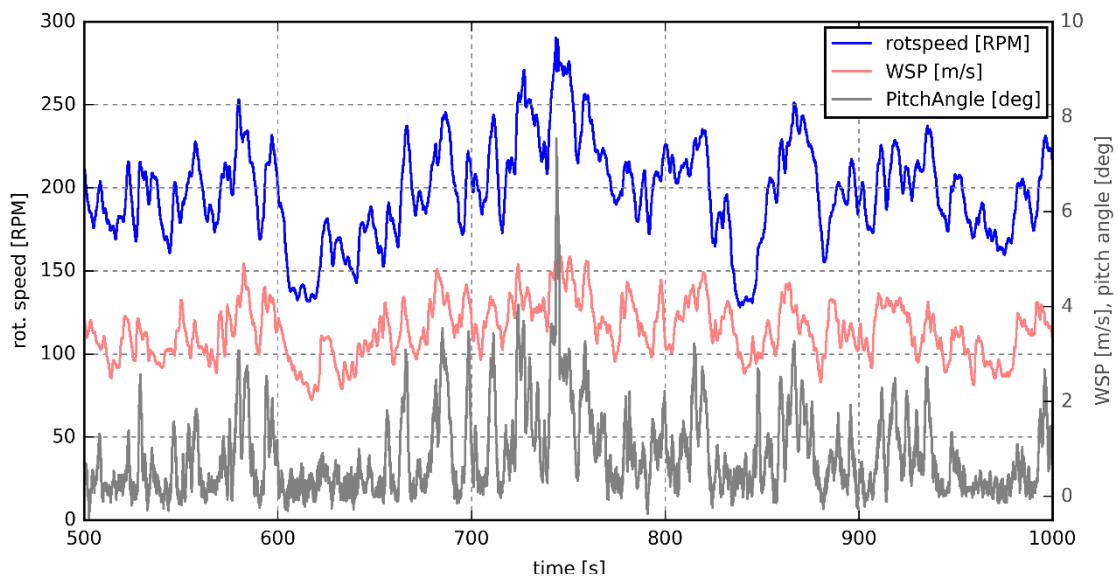


Figure 47. Sample time-series of the field test.

A sensitivity analysis has been conducted, where the generator characteristic has been modified to respond with a different torque, proportional to the original torque. Figure 48 (up) shows the passive pitch system response to a proportional increase in torque of 30%. The blades pitch out rarely and shortly. The pitch angle shows sometimes values lower than 0 degrees because the top is an elastic rubber bumper. Figure 48 (down) shows the response for a torque 30% lower. The blades are pitched out permanently. This behavior is in line with the operation principle explained in chapter ‘2. The concept’, the generator torque contributes to pitch in the blades, so an increase in this term supposes a reduction of the pitch angle if the other terms remain constant, and vice-versa. The comparison between these experimental time-series is acceptable because the mean wind speeds and standard deviations are almost identical.

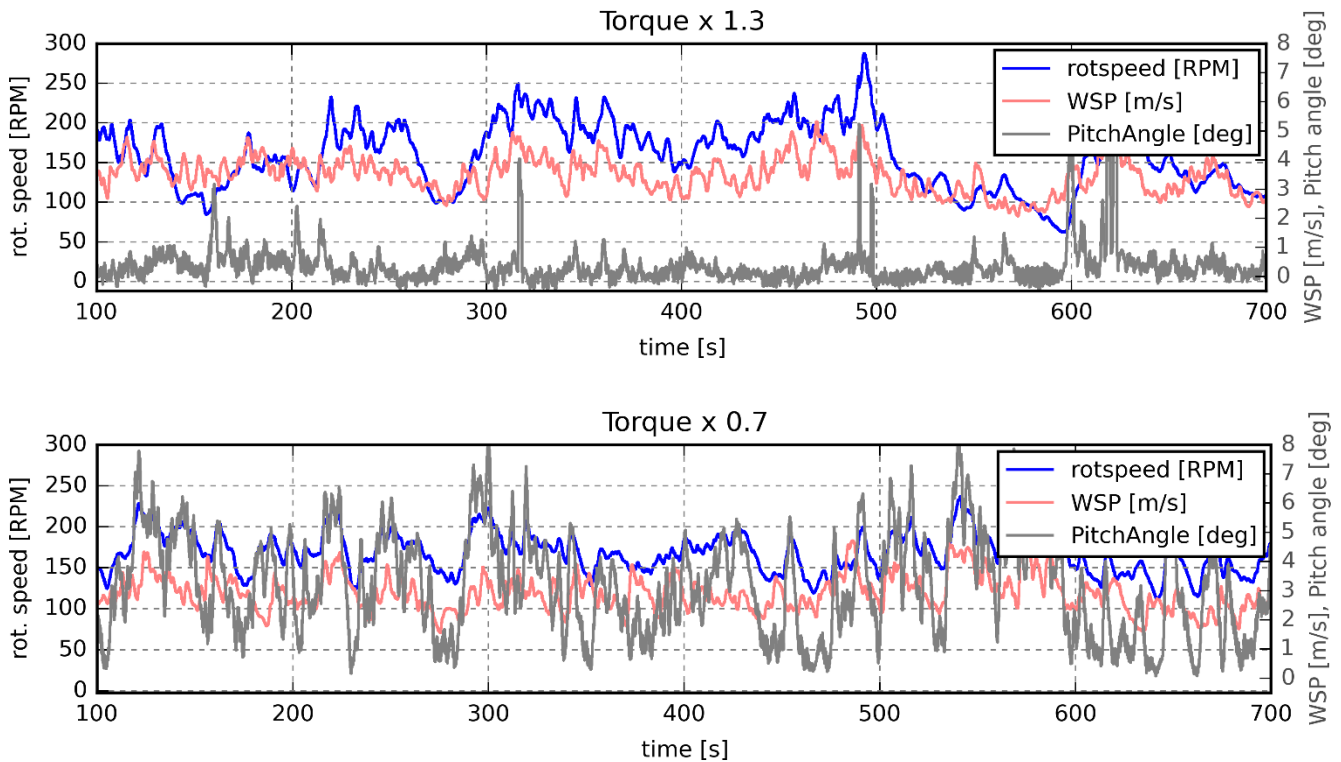


Figure 48. Time-series passive pitch system response to different generator torques.

Another test carried out has been to use the passive pitch system to keep the rotational speed at 200 RPM (22 W). Figure 49 shows a 10-minutes time-series of this experiment. It can be seen that when the 200 RPM value is surpassed, the pitch angle increases rapidly. It is noteworthy to say that the linkages have not been rearranged for this experiment, so the linkages for pitching out at 300W have been used. Nevertheless, the system performed notably well. This performance evidences the robustness of the system against changes in the power curve.

More information and results about the field test is given in Appendix E.

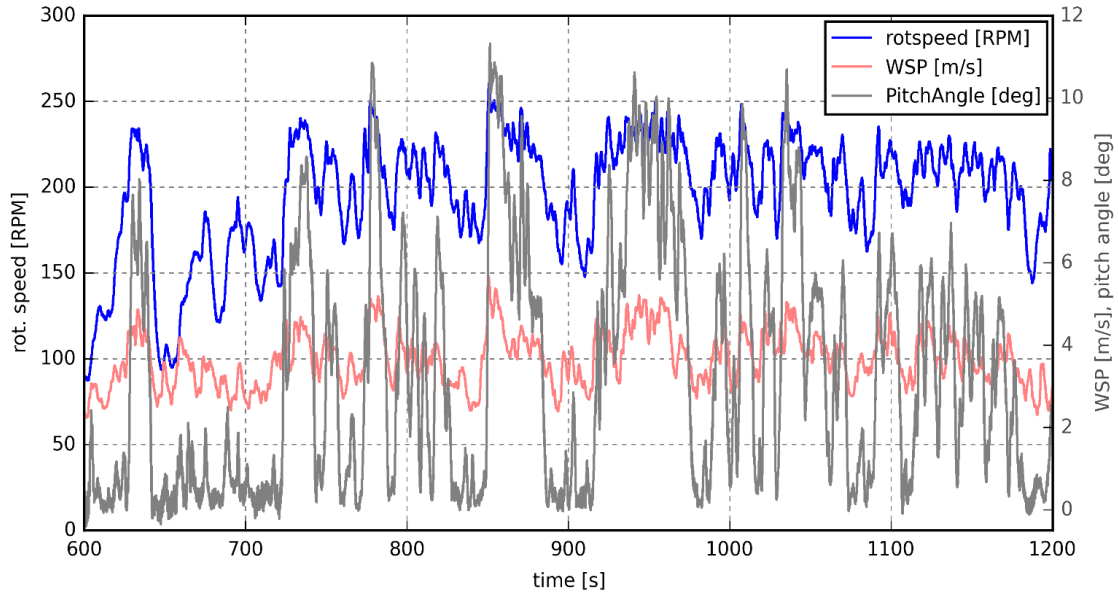


Figure 49. Time-series passive pitch system pitching out at 200 RPM.

Fatigue failure

Although the wind turbine was showing less vibrations than in the wind tunnel, a failure happened. This failure occurred in the thrust-torque sensor. Figure 50 and Figure 51 show the aftermath of this tragic incident.



Figure 50. SWT rotor after fatigue break



Figure 51. Nacelle and shaft after fatigue break.

Figure 52 and Figure 53 show a detail of two fracture sections. The section in Figure 52 presents beach marks, what indicates the fracture occurred due to fatigue. As the failure has been produced in a small number of cycles (less than 10^5), it corresponds to low-cycle fatigue²⁷. The uniform color in the beach marks suggests that the loading frequency remained unchanged. The pronounced shear lip²⁸ indicates that the fast fracture was ductile.

The section in Figure 53 correspond to another column of the component. This column, instead, does not present beach marks. The fracture resembles more to a ductile fracture than a brittle fracture, because of its fibrous appearance, although there is no clear neck. Furthermore, aluminum is a ductile material, and the fracture has not been produced due to an impact.

After this brief analysis of the failure, possible reasons of the origin of this accident will be given.

First of all, the passive pitch components were supposed to be made of aluminum, but they have been manufactured of steel. This added an extra weight to the system. Steel is approximately three times heavier than aluminum. As there were components taken from the previous design, made of aluminum, and other components were supposed to be made of steel, such as the slider, as deduced in section ‘3.1. Integration of the concept on the DTU SWT’, or other standard components, such as bearings, lever arms or screws, the hub weight became approximately twice the expected weight.

Furthermore, the slider, which is actually a shaft²⁹, presented an eccentricity. It was visible with naked eye. Ideally, a shaft must be manufactured as a single piece but, for this case, the slider was designed as a separate piece, in order to not remove the thrust-torque sensor in the design. This design did not perform well, and a redesign of the shaft and the slider as a single piece will be proposed in chapter ‘8. Future works’.

This chapter has presented the preparation of the entire system in the wind tunnel outlet, where, although it has been demonstrated that the wind flow is not adequate for valid measurements, a generator characteristic curve has been found experimentally, and the software has been tested. In the field test, it has been proved the passive pitch system concept, behaving as expected. The fatigue failure didn’t prevent us to take enough measurements for proving the concept and carrying out sensitivity analysis. In the next chapter, the collected data will be contrasted with the HAWC2 simulation results.

²⁷ Low cycle fatigue corresponds to less than 10^5 cycles, and its behavior is described by the Coffin-Manson relation.

²⁸ The shear lip can be seen in the top of the section in Figure 52. A shear lip is a zone near the outer surface where the fracture forms an angle of 45° with respect to the plane of the major fracture [42], which occurs in ductile fractures.

²⁹ A shaft is defined as a rotating machine element, which is used to transmit power from one part to another [58].

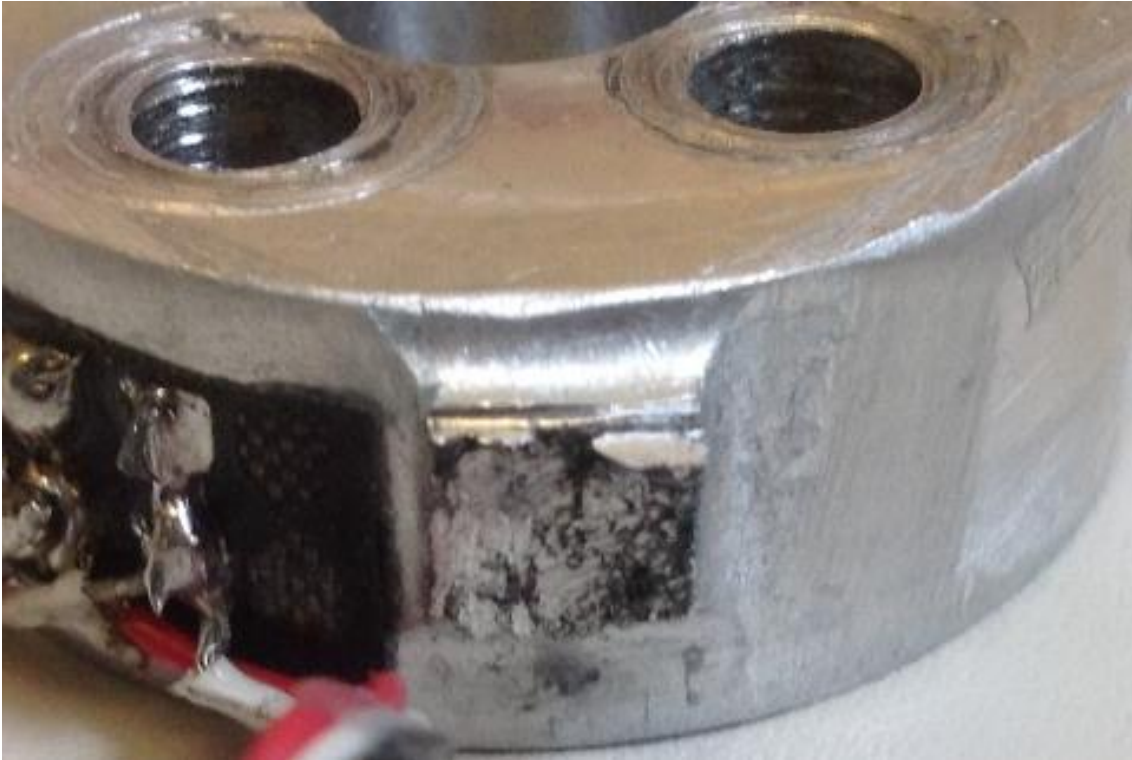


Figure 52. Fatigue break detail. Beach marks start from the lower right corner and spread to a big part of the section.



Figure 53. Sudden fragile fracture detail.

5. MODEL OF THE WIND TURBINE WITH HAWC2

In order to simulate accurately the real behavior of a wind turbine, aerodynamics and elasticity of the structure cannot be treated separately. The aerodynamic behavior influences the elastic behavior and vice-versa. Therefore, they have to be coupled. The coupling of these two disciplines is called aeroelasticity.

As wind turbines are submitted to turbulence and fluctuations from the wind, the process cannot be considered static, but time-dependent. The wind turbine behavior is described, therefore, by dynamic aeroelasticity, where inertial effects play also an important role.

Wind turbines are not simple mechanical machines, but they are monitored and controlled, in order to yield the biggest amount of energy and avoid failure. The elements usually controlled in a wind turbine are the pitch system and the generator. The coupling of control theory and aeroelasticity is called aeroservoelasticity.

Several commercial aero-hydro-servo-elastic³⁰ modelling software packages exist nowadays, such as FAST, BLADED, ADAMS, FLEX5 and HAWC2 [29]. HAWC2 is the software used in this project because of its wide multibody application, the ability of model any complex system with ease, and its flexibility.

HAWC2 (Horizontal Axis Wind turbine simulation Code 2nd generation) is a powerful code for aero-hydro-servo-elastic simulations especially designed for wind turbines developed by DTU [30] [31].

5.1. Dynamic simulation

The DTU 500W SWT already disposed of a HAWC2 model, made by previous years' students. However, several changes have been done in order to implement the new hub with the enbreeze pitch system and change to downwind. Figure 54 shows the layout of the numerical model.

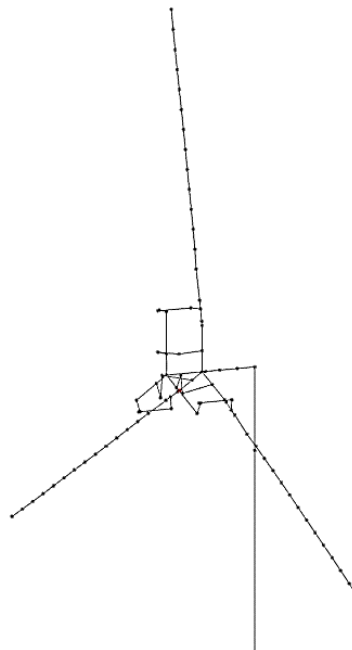


Figure 54. Layout of the DTU SWT structure in HAWC2

³⁰ The hydrodynamic part is not relevant in this project

The change to downwind in practice only implied to change the orientation of the blades. In the numerical model, however, it is more complex, because the tower shadow behaves differently, for being the downwind rotor affected by the wake of the tower.

For upwind wind turbines, potential flow is assumed. But assuming potential flow is a bad approximation for a downwind machine, where each blade passes the tower wake once a revolution [32]. Potential flow is characterized by an irrotational velocity field. For flows with strong vorticity effects, the potential flow is not applicable [33]. The wake is not characterized only for its decrease in wind speed, but also for its increase in turbulence. Therefore, another method is required. HAWC2 offers a model based on the boundary layer equations which especially suits downwind simulations. This model has been used in this project.

To implement the tower shadow in HAWC2, the drag coefficient of the tower is needed. The tower is a cylinder, and the drag coefficient on a cylinder depends on the Reynolds number as in Figure 55. For a tower of 10cm diameter, and a temperature of 10°C, the Reynolds number is approximately $Re=2.2e-6$, according to Equation 1, which corresponds to a drag coefficient of around $C_D = 0.6$.

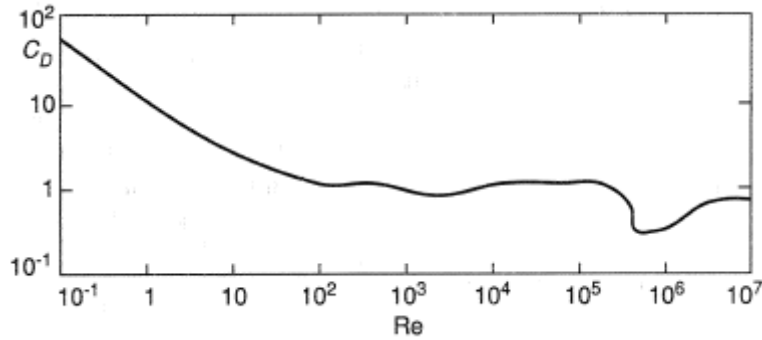


Figure 55. Drag coefficient for a cylinder in function of the Reynolds number. Source: [52]

The first dynamic simulation has been carried out in order to compare the behavior of the real model with the HAWC2 model. To do so, the same conditions as in the field test have been recreated. As the wind is only measured in one point (the anemometer), and this point does not belong to the wind turbine, the same wind field cannot be reproduced. Instead, the measured mean wind speed and standard deviation are applied. These values are given in Table 5.

Table 5. Field test conditions

<i>Indicator</i>	<i>Value</i>
<i>Mean (μ) [m/s]</i>	3.24
<i>Std (σ) [m/s]</i>	0.55
<i>Turb. Int (I) [-]</i>	0.17

HAWC2, however, does not consider the standard deviation as an input, but the turbulence intensity (I). Turbulence intensity is defined as in Equation 11.

$$I = \frac{\sigma}{\mu} \quad (11)$$

In Table 5, it can be seen that it results a high turbulence intensity. The reason is that the standard deviation is approximately independent of height in the surface layer [10], but not the mean wind speed. Therefore, the turbulence intensity decreases with height and, in this case, the hub height is very low.

The chosen method to create the turbulent wind field is the Mann model. More information about this model and its configuration in function of the weather conditions can be found in Appendix F.

The simulation resulted in a similar behavior of the HAWC2 model with the prototype. Table 6 and Figure 56 compare the rotational speed, the wind speed and the pitch angle.

Table 6. RPM comparison between the HAWC2 simulation and the prototype in the field test.

<i>Indicator</i>	HAWC2	Prototype
<i>Mean rot. speed [RPM]</i>	190.3	171.8
<i>Std. rot. speed [RPM]</i>	28.3	34.4

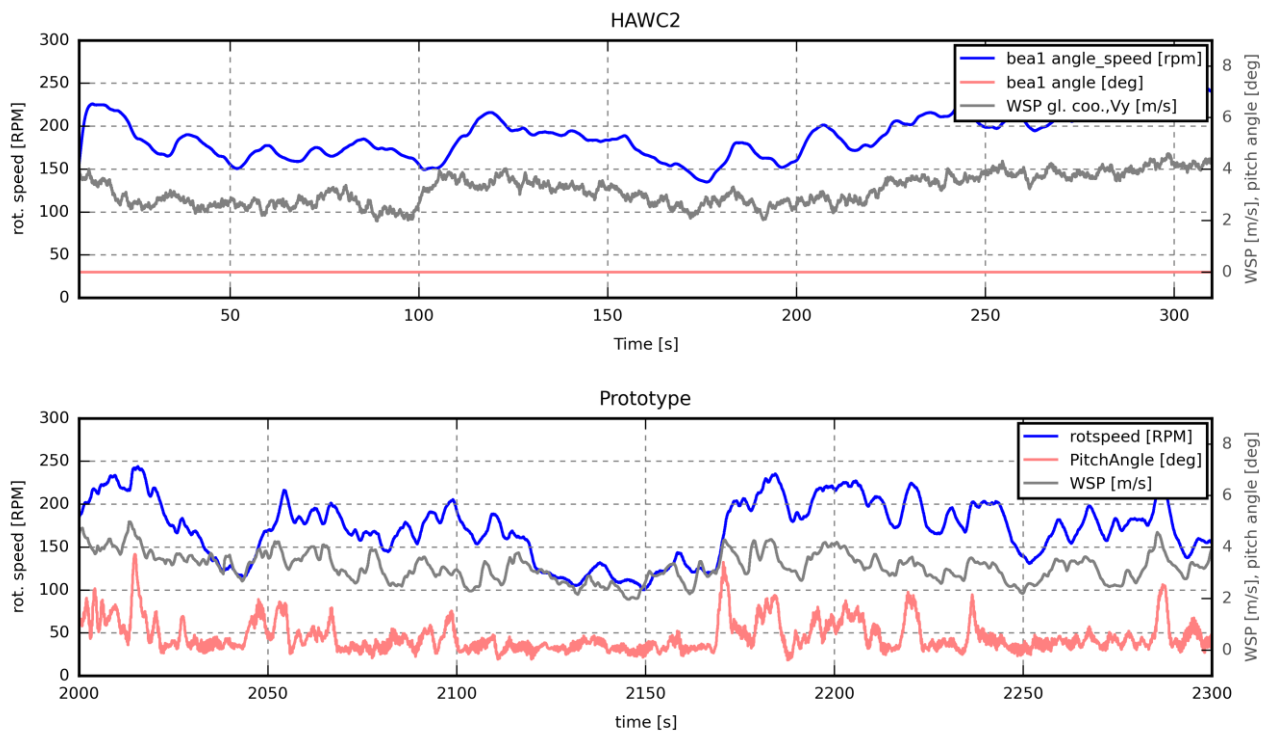


Figure 56. Comparison between HAWC2 simulation and the prototype in the field test.

In Figure 56, the wind speed in the field test appears to be less turbulent. This is actually the result of the smoothing filter. This effect helps a better visualization but destroys the real frequency spectrum.

The parameter that really diverges in both time-series is the pitch angle. In the HAWC2 simulation it is constantly 0, and in the prototype, it varies with wind fluctuations. It means, some parameters in the HAWC2 model need a re-adjustment.

In the design of the model, two parameters have been estimated due to the impossibility of finding the exact value. These are the pre-stress and the damping in the passive pitch system.

During the assembly of the system, it has been noticed that a small difference in the length of the passive pitch system rods for each blade creates a big increase in the force needed to move the hub along the slider. So, even an accurate calculation of these parameters can lead to a mismatch with the real system.

Pre-stress and damping are included in an external function (in a ‘dll’ file) that contains the equations of motion of the passive pitch system and describes the behavior of this. A small sensitivity analysis has been carried out to assess the influence of these in the pitch behavior.

Figure 57 shows the effect of the damping value in the external function. The comparison between the results with the real system suggests that the damping is even lower than 0.1 Nms/rad.

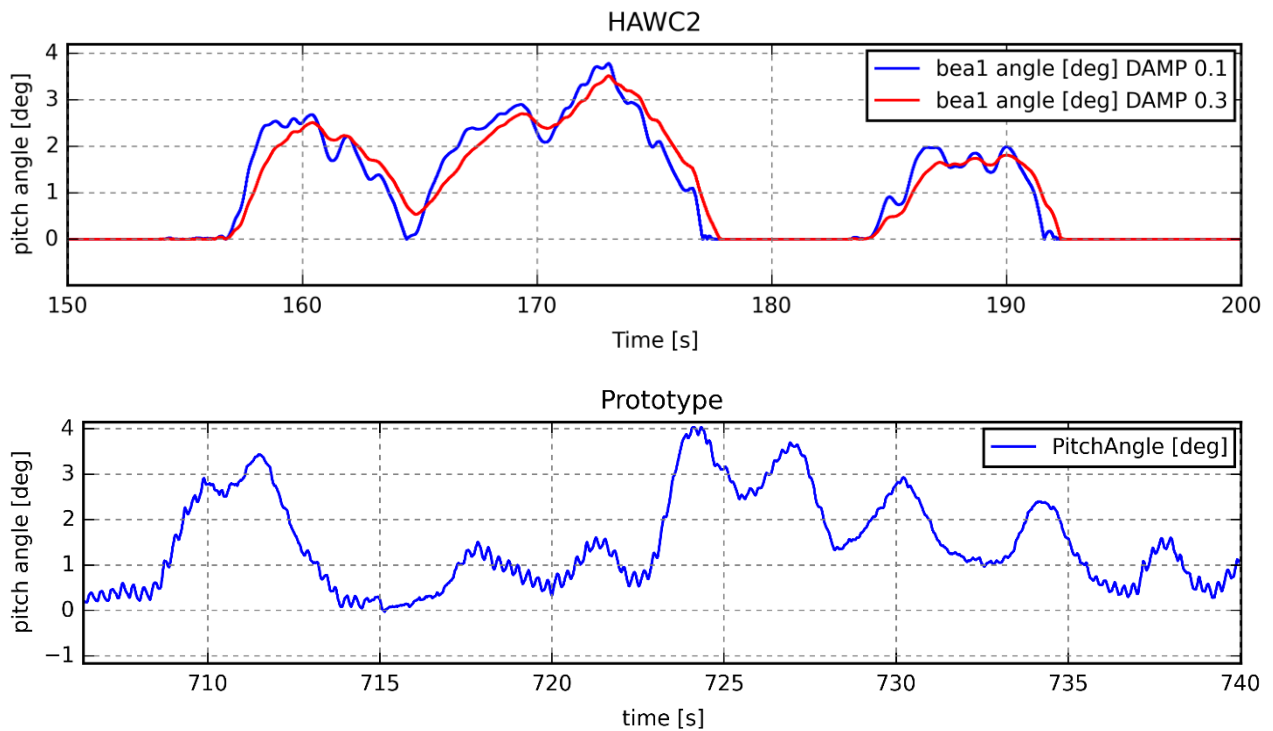


Figure 57. Pitch angle for different values of damping in the passive pitch system (up), and comparison with the real behavior (down)

The pre-stress can be understood as a fixed force that reduces the pitch angle a constant value (unless it is already 0), as seen in Figure 58.

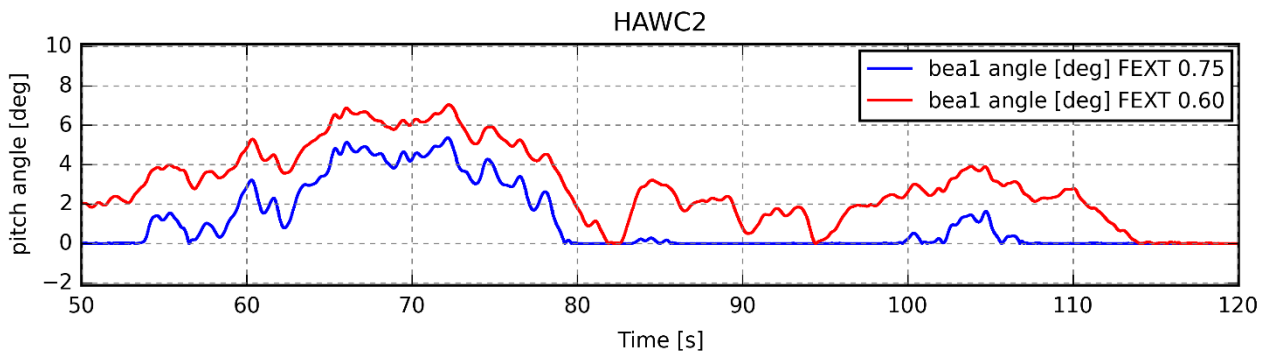


Figure 58. Pitch angle for different values of friction in the passive pitch system.

By fine-tuning, it is found that the values of damping and pre-stress that best fit the real behavior are 0.05 Nms/rad and 0.075 N, respectively. The time-series with these parameters can be seen in Figure 59. The estimated pre-stress was 0.05 N, which is a difference of 33%, but the estimated damping was 0.5Nms/rad, which is a difference of 90%.

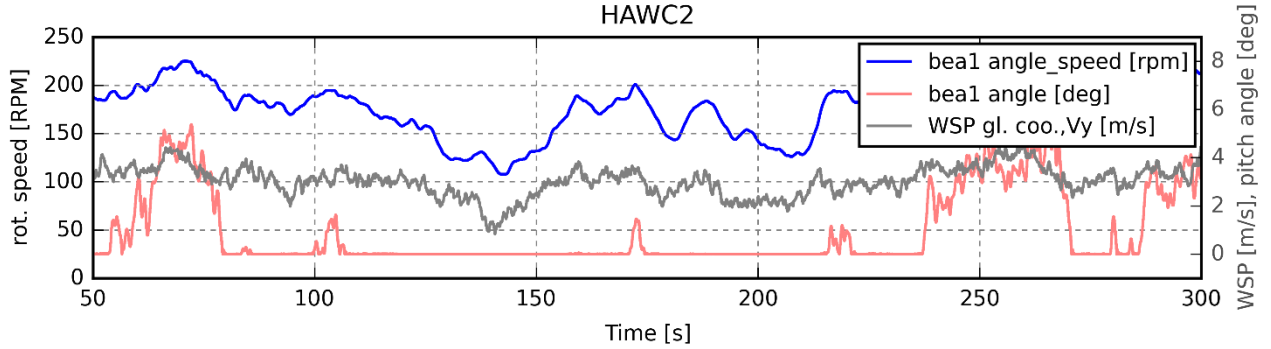


Figure 59. Time-series of the recreated conditions in HAWC2 of the field test after fine-tuning.

5.2. Comparison between DTU 500W SWT and enbreeze 15kW WT

The parameters of both turbines are shown in Table 7. In order to compare both models, a 500W downscale of the enbreeze wind turbine has been calculated according to similarity rules for wind turbines. The used similarity rules are shown in equations from 12 to 15.

$$\frac{P_2}{P_1} = \frac{R_2^2}{R_1^2} \quad (12)$$

$$\frac{H_2}{H_1} = \frac{R_2}{R_1} \quad (13)$$

$$\frac{\omega_2}{\omega_1} = \frac{R_1}{R_2} \quad (14)$$

$$\frac{V_2}{V_1} = 1 \quad (15)$$

Where P is the rated power, R the rotor radius, H the hub height, ω the rotational speed and V the wind speed. Note that V applies to all wind speed-related parameters.

The values of the downscale model in Table 7 exhibit a better performance than the ones of the DTU turbine, reaching rated power at a lower wind speed. As shown in section ‘1.3. Scope and limitations’, this would not be possible because, for such a small size, the Reynolds number decreases below $Re=2e5$, changing the blade coefficients and, therefore, leading to a lower performance.

Table 7. Comparison of the specifications between the DTU 500W SWT and the enbreeze 15kW WT. The values in parenthesis refer to the late generator characteristic modification to 300W to adapt to the acquired electronic load.

<i>Parameter</i>	DTU ³¹	enbreeze	Exact enbreeze 500W downscale
<i>Rated power [kW]</i>	0.5 (0.3)	15	0.5
<i>Rated rot. Speed [RPM]</i>	600 (480)	83	455
<i>Rated wind speed [m/s]</i>	9.6 (8.2)	8.3	8.3
<i>Switch on wind speed [m/s]</i>	3 ³²	2.5	2.5
<i>Switch off wind speed [m/s]</i>	15	15	15
<i>Rotor diameter [m]</i>	1.75	11.5	2.1
<i>Number of blades</i>	3	3	3
<i>Wind direction tracking</i>	Passive, downwind	Active, downwind	Active, downwind
<i>Generator</i>	PMSG	PMSG	PMSG
<i>Hub height (m)</i>	1.5	20.85	3.8

The power curves of both wind turbines in function of the wind speed are depicted in Figure 60. As it can be seen, both curves match accurately the rated power in the limitation zone, evidencing the well performance of the enbreeze passive pitch system. It is noteworthy to say that, when the wind speed exceeds 15 m/s, the generator is disconnected, producing no electrical output.

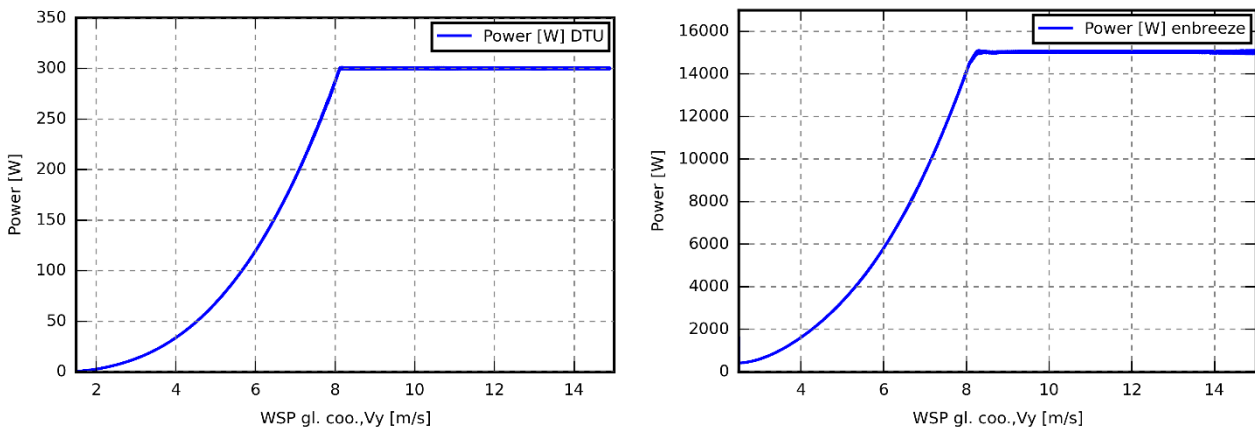


Figure 60. Power curve for the DTU SWT (left) and the enbreeze WT (right).

³¹ The specifications of the DTU SWT consider the empirical power curve explained in section ‘4.1. Wind tunnel outlet’.

³² The switch on wind speed in the SWT depends on the cogging torque. The cogging torque is the torque caused by the magnets of the generator, when moving from one slot to the next. It fades with increasing rotational speed, because the rotor inertia becomes bigger, but at low revolutions it plays an important role, being the most important barrier to start the generator.

The DTU SWT has been tested successfully under wind speeds lower than 3 m/s, but it needed human help to start spinning.

Figure 61 shows the rotor rotational speed and the pitch angle in function of the wind speed. The enbreeze wind turbine pitches out before rated wind speed, and it keeps a more constant rotational speed in the limitation zone. The same behavior could not be recreated in the DTU SWT for constructive reasons (the crank length could not be reduced further).

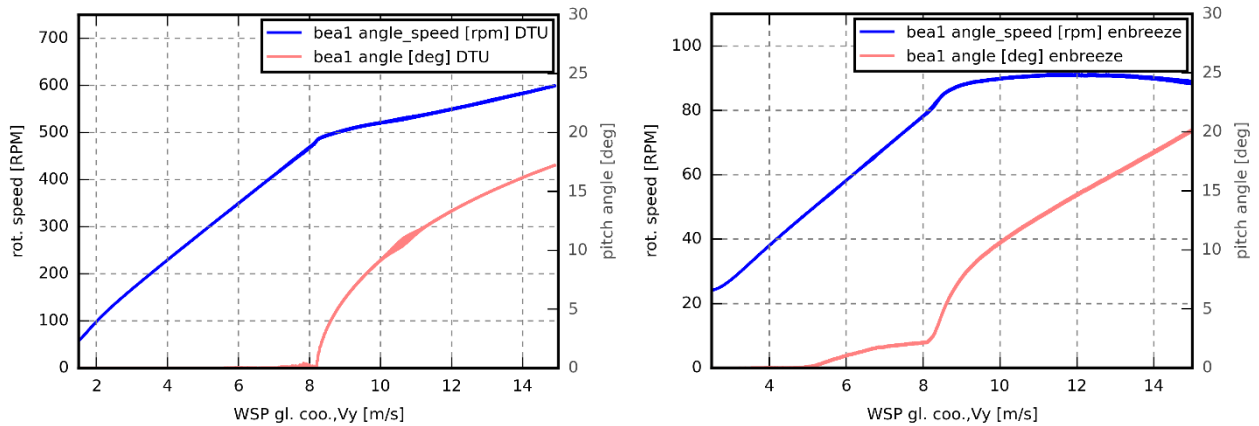


Figure 61. Rotational speed and pitch angle in function of the wind speed for the DTU SWT (left) and the enbreeze WT (right).

The rotational speed is the only parameter that changes qualitatively in the enbreeze passive pitch system with respect to an active pitch system. Being the rotational speed in the latter a straight horizontal line. This is not a big issue for the enbreeze passive pitch system, because the generator characteristic of the PMSG prevents the power from increasing beyond the rated power.

The generator characteristics of both wind turbines are shown in Figure 62. Both follow Equation 4, but each one with different parameters. Note the huge difference in torque between both wind turbines. This is because the torque scales to the cube of the rotor radius, as can be deduced from equations 3, 12 and 14.

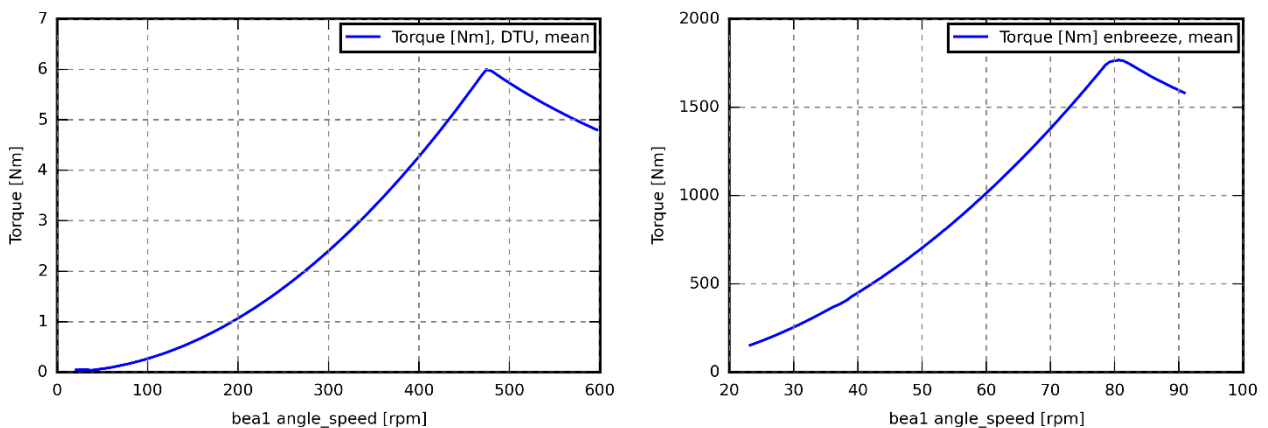


Figure 62. Generator characteristic of DTU SWT(left) and enbreeze WT (right).

The thrust for different values of wind speed is presented in Figure 63. The thrust behavior in both wind turbines is similar. In the figure, as well as in previous figures, the DTU wind turbine has a sharper peak. This is because the generator characteristic is implemented following discrete points, and in the DTU wind turbine a point matches exactly the rated value.

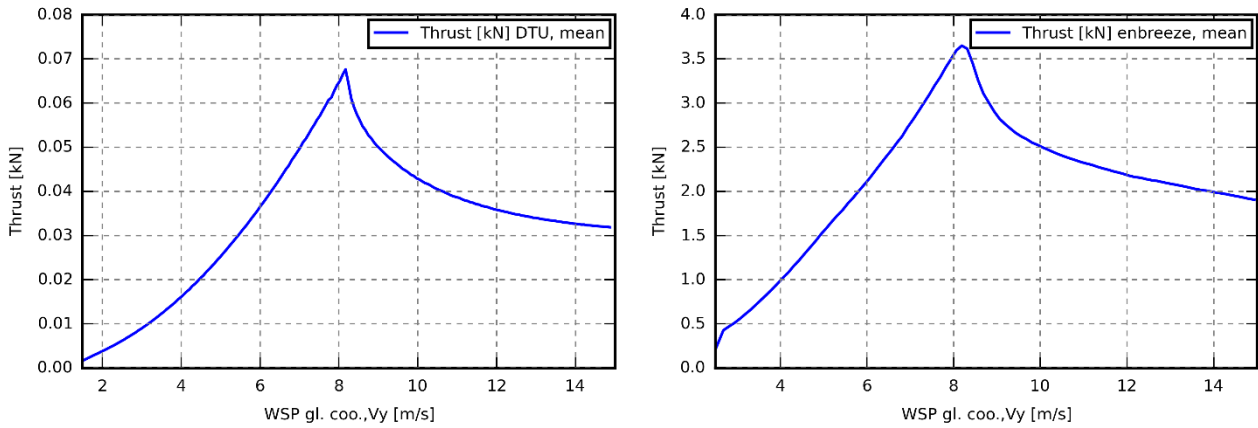


Figure 63. Thrust vs wind speed for DTU SWT (left) and enbreeze WT (right).

The pitching moment of both wind turbines for the operative range of wind speeds is shown in Figure 64. For the same reason as in the thrust, the pitching moment decreases beyond rated speed because the blades are more parallel to the flow, because of the increasing pitch angle. It calls the attention that the DTU SWT reaches negative pitch moment values. It means that the pitching moment pitches to feather (the positive sign is set following the right hand rule, corresponding to pitch to stall), contributing to the movement of the blade in the desired direction.

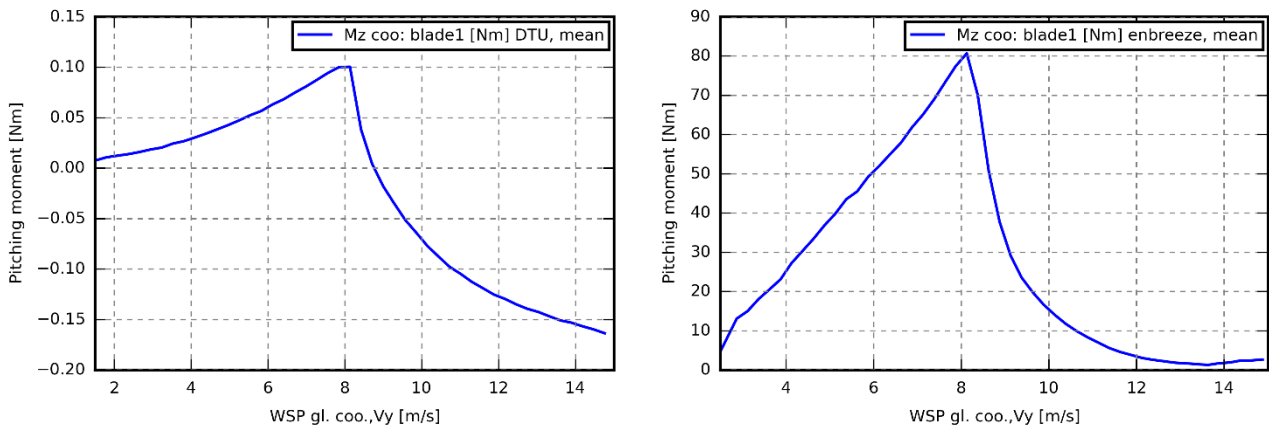


Figure 64. Pitching moment vs wind speed for the DTU SWT (left) and the enbreeze WT (right).

In this chapter, it has been validated the HAWC2 model by contrasting with the experimental data. Once this has been achieved, the parameters of the DTU SWT have been compared with the parameters of the enbreeze WT. The enbreeze wind turbine shows a higher efficiency, because its hypothetical 500W downscale model reaches rated power at a lower wind speed than the DTU SWT. The enbreeze wind turbine also shows a better control of the rotational speed, being the behavior of the DTU SWT difficult to improve due to constructive reasons.

6. ANALYSIS OF THE 15KW WIND TURBINE

As commented in the introduction, one of the reasons why it has been decided to start this project is to approach the reduction of an instability on the enbreeze wind turbine that prevents the correct operation of the passive pitch system when a damper is not used. The actual damper is a magnetorheological damper placed between the generator disc and the hub. The damper is undesired for its investment and maintenance costs. This instability on the rotational speed and the pitch angle is shown in Figure 65 (up). The response to the same wind step with damper is shown in Figure 65 (down).

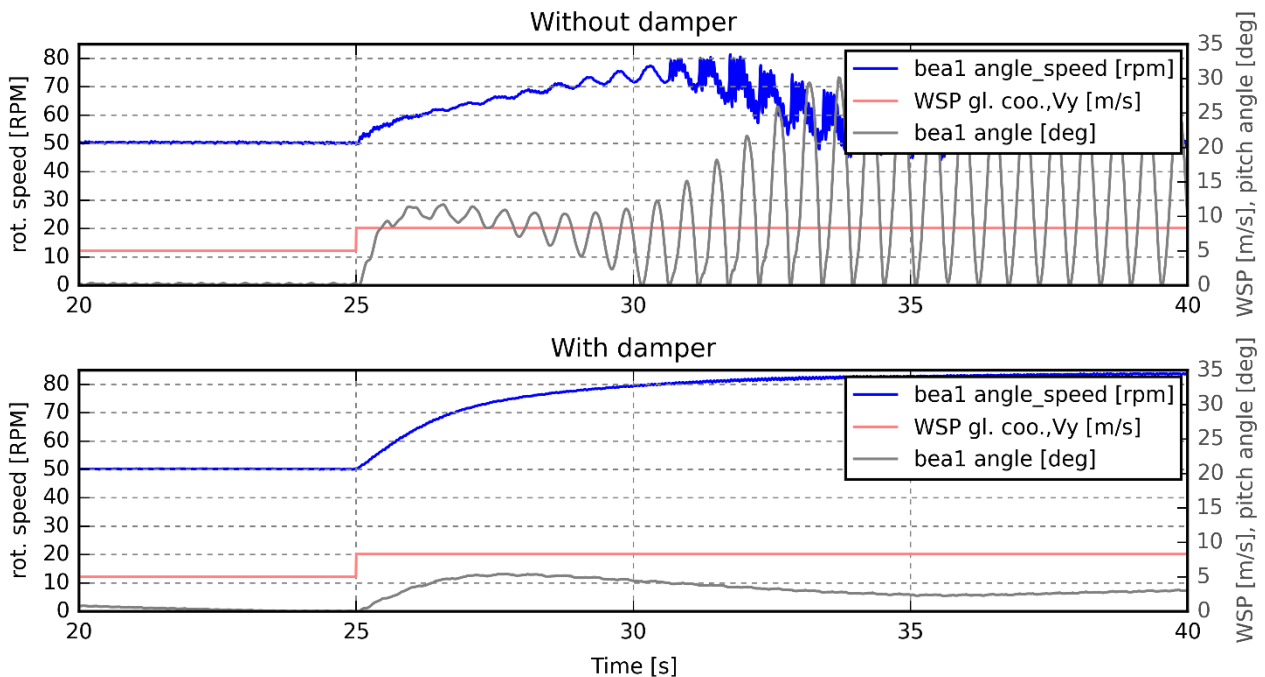


Figure 65. Instability on the 15kW wind turbine (up) and a solution to this problem with a damper (down) against a step change in the wind speed.

It has been also mentioned that the instability is thought to be caused by the oscillation of the tower. In this project, a stiff tower has been used. However, after changing the position of a linkage (from $L=0.55$ to $L=0.4$, but this is not important), the behavior shown in Figure 66 has been found. It is also an instability.

It is noteworthy to say that there is a chance that this instability is not real, and it is caused by a computational error. This possibility is considered because the conditions in Figure 66 have been tested with the prototype, and this instability did not appear. However, this fact does not imply that the instability does not exist, since the HAWC2 model, although appears to behave similar as the prototype, something could have been overlooked.

Henceforth, solutions for the instability will be presented assuming that it exists, because, even if it were not real, the presented proposals are useful for a general better performance of the wind turbine.

Two important conclusions can be stated so far: the instability can happen without the influence of the tower oscillation, and it is not an issue of a specific wind turbine.

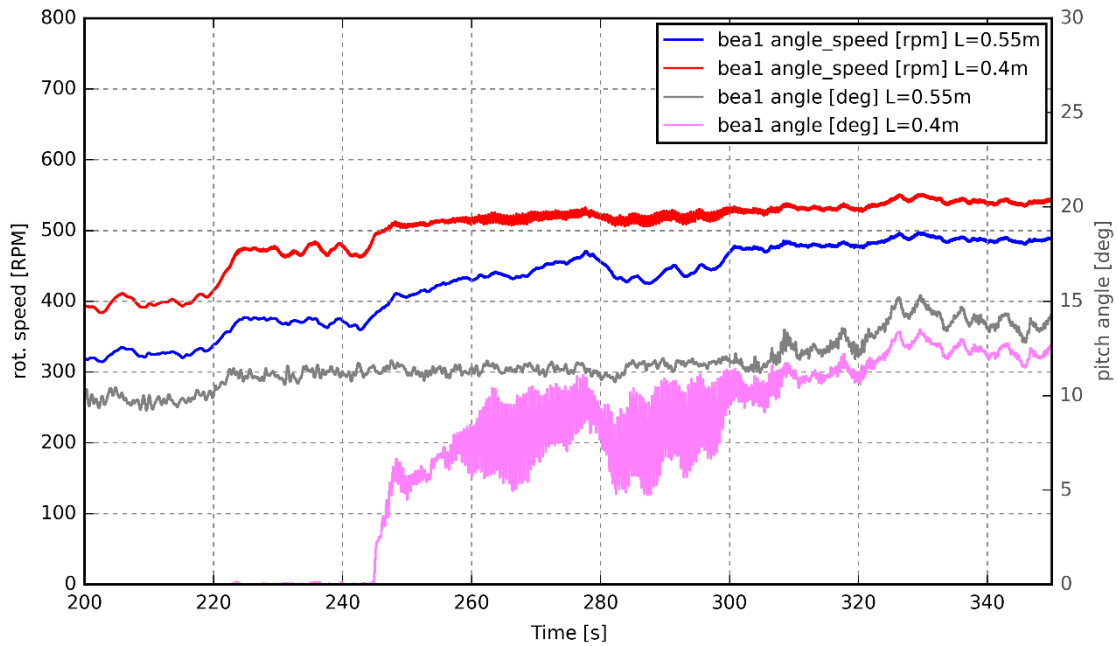


Figure 66. Instability found in the DTU SWT when changing the position of a linkage of the passive pitch system.

Indeed, if the tower is assumed stiff, there is no instability in the 15kW WT. However, this is because the smoothing filter of the generator prevents the instability to increase. Figure 67 shows the instability when the smoothing filter is removed. From this can be concluded that the tower does not cause the instability, but maximizes its effect and decreases its frequency.

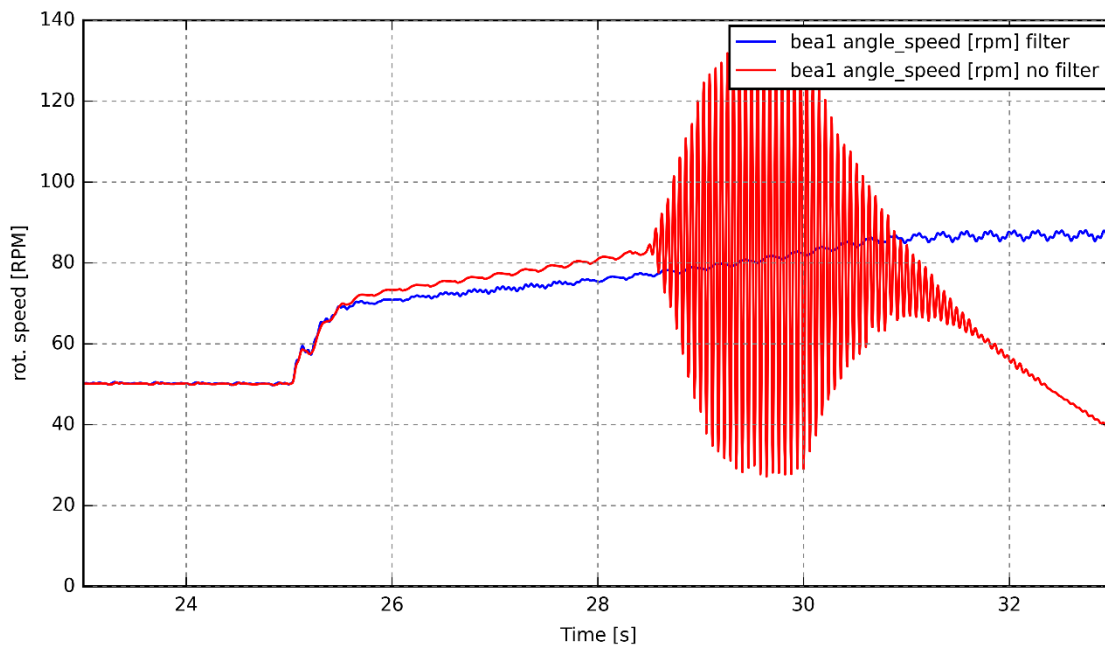


Figure 67. Instability in the 15kW WT with a stiff tower when the smoothing filter is removed.

The aerodynamic damping is not involved in this issue either. The aerodynamic damping is the damping associated to the aerodynamic forces on the wind turbine [32]. If the angle of attack were enough big to reach the zone of the lift coefficient with negative slope in a lift coefficient vs angle of attack curve, the aerodynamics would contribute negatively to the damping

of the system. This is not the case, since the blades pitch to feather. The so-called stall flutter³³ issue appears in pitch-to-stall systems, because the airfoil works in the abovementioned zone with negative lift coefficient slope.

The lift coefficient slope has been measured in HAWC2, reaching negative values only when the instability has grown considerably. This confirms that the aerodynamics contribute positively to the damping of the system.

From the experience acquired in this project, two kinds of solutions will be presented for further analysis by another student.

6.1. Control solution

The generator controller is a key system to prevent the instability. As said in chapter ‘2. The concept’ one of the advantages of the enbreeze passive pitch system is that it can be controlled from the generator. This advantage can be used now to fix the instability issue.

The MPPT controller exposed in the ‘3.2.5. Generator control’ section is only the core of the generator controller. This controller in a real wind turbine can become much more complex. Figure 68 shows the old Risø controller, where the generator controller is located in the half-upper part.

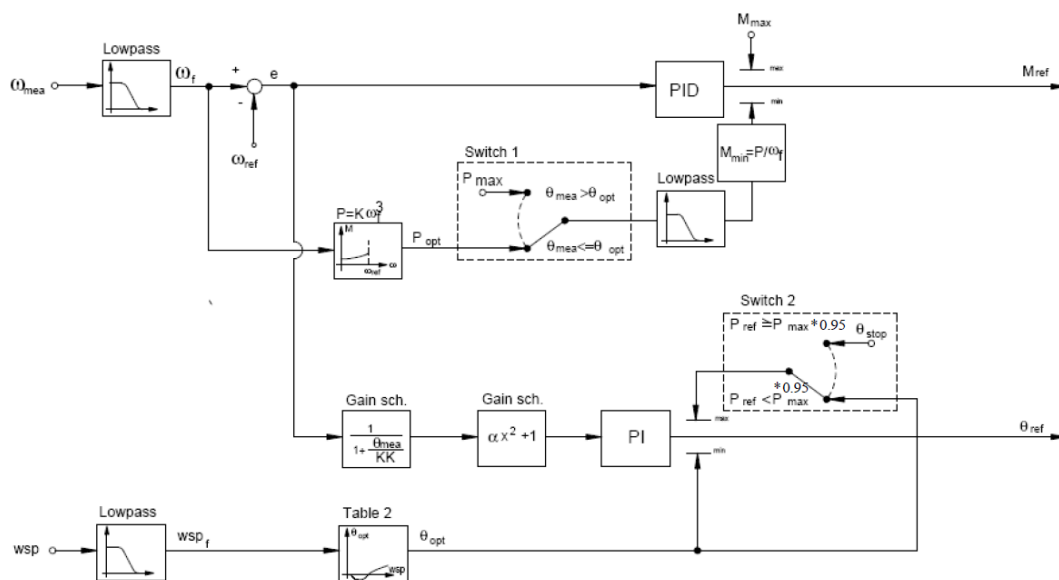


Figure 68. Old Risø controller. Source: [53]

The enbreeze controller, as mentioned before, already includes a low-pass filter (smoothing filter) and the torque saturation limits. An important part that has not been included yet is the PID. PID controllers are control loop feedback mechanisms that affect only to the dynamic response of the controller (if configured correctly). By using a PID, the generator would respond better to wind fluctuations, and the instability could be solved.

From the control theory point of view, the response of the pitch system is unstable. It means that the pitch angle value tends to infinity when a step change in the wind speed is produced. Unstable systems can become stable by choosing the correct PID parameters. A common mistake is to try to stabilize the system by using zero-pole cancellation. This is not

³³ The stall flutter is the flutter caused by stalling the blade.

possible because in the reality, the value of the zero would never match with the value of the pole. Even in a computer, due to rounding error, the response becomes unstable.

If the source of the instability is known, and is not the system itself, disturbance rejection mechanisms, such as feedforward or cascade control can be applied. Feedforward control has the disadvantage that it needs a measurement of the disturbance, i.e. an extra sensor, while cascade control is a PID-controlled loop inside the main loop. The main loop is the loop where the torque (manipulated variable) controls the rotational speed (controlled variable).

6.2. Design solution

The presented approach is based on mitigating actively the effect of the instability. But, in Figure 66 it has been shown that the instability appeared by simply changing the position of a linkage in the DTU SWT. There is not a single linkage solution that fulfills the requirements, but a wide range of solutions. The process of calculating the linkages is long, and requires subsequent manual fine-tuning with HAWC2.

A proposed approach to find the best linkage positions is to use operations research. To assess all possible configurations one by one would be too computationally expensive. Instead, an optimization algorithm would reach much faster to an optimal solution.

A way to link HAWC2 with an optimization algorithm is by using MATLAB. HAWC2 can be linked to MATLAB through a TCP/IP connection. In the HAWC2-MATLAB communication, HAWC2 is controlled from MATLAB.

MATLAB offers built-in operations research functions. For example, the genetic algorithm function would fit for this purpose because it can solve non-linear problems.

An optimization problem is defined by an objective function and constraints. In this case, the objective function would be to maximize the power output, and the constraints, among others, to keep the instability under a certain limit.

In the same way as the previous proposed solution, this solution, even if it does not solve the instability, the performance can potentially be improved.

This chapter concludes the thesis. It has been evaluated the behavior of the passive pitch system in the enbreeze wind turbine without damper. An instability prevents the correct operation appears when the pitch system is activated. Two solutions, one based on the active control of the generator, and the other based on a different design process, have been proposed for a further study.

7. CONCLUSIONS

The 500W DTU SWT has been used in order to prove the passive pitch concept introduced by enbreeze. An exact downscale of the 15kW WT has not been built because similarity rules are not fulfilled for Reynolds numbers lower than $Re=2e5$.

The most important conclusion is that the passive pitch system performed qualitatively as expected. However, quantitatively, some discrepancies have been found. For example, the pitch angle presented a slightly different behavior below rated wind speed, but with a small correction in the HAWC2 model, the behavior has been corrected.

A remarkable comment is that with a reduced budget (less than 3000€), an entire prototype hub with passive pitch system plus all the necessary instrumentation to analyze its behavior have been built.

The output of a small wind tunnel has been used in order to check the correct operation of the instrumentation and control system. It has been proven that the wind conditions in the output are not adequate for a reliable test. In the Risø test field, the passive pitch system concept has been proven. A fatigue failure during the test did not avoid to prove the concept and validate the HAWC2 model with the collected data.

The enbreeze wind turbine has been tested without the use of a damper in the passive pitch system. An instability that prevents the correct operation of the wind turbine has been shown. It has been shown that the flexibility of the tower is not causing this instability, although it influences its impact. Two different improvements have been proposed in order to fix the instability problem and improve the behavior of the wind turbine.

As a final conclusion, this thesis evidences the challenge that suppose wind turbines. To accomplish this project, a combination of different disciplines has been required. Mechanics, design and drafting, aerodynamics, micrometeorology, instrumentation, electronics and control engineering. For a complete wind turbine design project, expertise in more disciplines are needed, such as civil engineering or materials science. To be successful in a wind turbine design, it is required, therefore, not only a team composed by expert members, but a well-coordinated team.

8. FUTURE WORKS

This project required a considerable amount of work, which led some secondary tasks to be postponed. An important task that could not be done is to find the optimal pitch angle of the new rotor configuration, which is explained in section ‘3.1. Integration of the concept on the DTU SWT’.

Another task that could not be completed is the optimization of the generator controller in LabVIEW. Considering what is explained in section ‘6.1. Control solution’, the actual controller only comprises the MPPT lookup table. Furthermore, the tasks of data acquisition and control are working in series, that prevents the computer to use more than one core. The performance can be improved if a parallel configuration which allows multicore processing, such as a producer/consumer pattern, is used.

The bending moment sensor described in section ‘3.3. Designing the bending moment sensor’ could not be manufacture. The drawing is appended to this report to allow its manufacture.

The pitch angle requires an accurate measurement. As said in section ‘3.1. Integration of the concept on the DTU SWT’, the limits of the pitch angle have been checked using a phone app. Furthermore, in the post-processing tool, it has been assumed that the pitch angle is linear in function of the slider position, which is a simplification. The pitch angle measurement can be improved by using the real mathematical relationship and more accurate methods to find and adjust its limits.

An unforeseen issue was the eccentricity on the shaft, exposed in section ‘4.2. Risø test field’. If a future student desires to work with the prototype, this issue will have to be fixed before testing the prototype. In the same line, a more robust shaft might be needed for the increase in weight.

A proper wind tunnel could not be accessed. If in the future there is the opportunity to test the wind turbine in a wind tunnel, valuable information will be acquired, such as the optimal power curve in function of the wind speed.

Finally, this project is actually a part of a bigger project, which is the design and commercialization of the enbreeze 15kW wind turbine. Two more students are now doing their thesis as a part of this project. One is working with the mitigation of the instability, and the other is working in the instrumentation of the wind turbine, for a later test. It is desired that both can take advantage of the experience acquired in this project.

REFERENCES

- [1] S. e. al..Germany Patent DE 10 2017 004 909.2, 5 2017.
- [2] A. K. Antariksh Dicholkar, "Rotor Design for SWT 500W HAWT," DTU, 2017.
- [3] T. Poryzala, "Design and analysis of a mechanical passive pitch control system for a small HAWT," DTU, 2016.
- [4] H. A. M. F. R. Leonardo Bergami, "A Two-Bladed Teetering Hub configuration for the DTU 10 MW RWT: loads considerations," DTU Wind Energy, Roskilde, Denmark.
- [5] J. Dabrowski, "Strömungskraftanlage". Germany Patent WO2014012591 A1, 19 7 2014.
- [6] A. D. Hansen, Introduction to wind power models for frequency control studies, DTU Wind Energy, 2016.
- [7] M.-G. K. a. P. H. Dalhoff, "Yaw Systems for wind turbines – Overview of concepts, current challenges and design methods," Journal of Physics: Conference Series, Hamburg, Germany, 2014.
- [8] J. R. A. Gerhard H Albers, "Governor for wind-driven propellers". United States of America Patent US2480687 A, 30 8 1949.
- [9] J. T. Robert Gasch, Wind Power Plants, Berlin: Springer, 2012.
- [10] J. M. M. K. a. M. N. Jacob Berg, Micro meteorology for Wind Energy, DTU, 2017.
- [11] "<http://www.sensopart.com/>," SensoPart Industriesensorik GmbH. [Online].
- [12] "<http://www.ni.com/white-paper/4803/en/>," National Instruments. [Online].
- [13] T. J. L. Mads M. Pedersen, "Pdap Manual," DTU Wind Energy, 2014.
- [14] "en.wikipedia.org/wiki/Boost_converter," Wikipedia. [Online].
- [15] M. R. M. M. R. Kot, "Comparison of maximum peak power tracking algorithms for a small wind turbine," *SciVerse ScienceDirect*, 2013.
- [16] D. & S. S. C. & M. A. & A. M. Zammit, "MPPT with Current Control for a PMSG Small Wind Turbine in a Grid-Connected DC Microgrid," 2017.
- [17] S. Z. B. M. M. L. E. Badreddine Lahfaoui, "Real time study of P&O MPPT control for small wind PMSG turbine systems using Arduino microcontroller," *ScienceDirect*, 2016.

- [18] "www.thedebugstore.com," Great Western Microsystems Ltd. [Online].
- [19] J. R. Folch, INTRODUCCIÓN A LAS MÁQUINAS SÍNCRONAS, Polytechnic University of Valencia.
- [20] VISHAY GENERAL SEMICONDUCTOR, "Rectifiers for Power Factor Correction (PFC) Application Note".
- [21] "www.hbm.com/en/7115/how-does-a-multi-axis-sensor-work/," [Online].
- [22] Y.-L. & P. J.-J. & S. J.-B. Kim, "Crosstalk calibration for torque sensor using actual sensing frame," *Journal of Mechanical Science and Technology*, pp. 1729-1735, 2010.
- [23] "https://www.automation.com/pdf_articles/cross_talk.pdf," automation.com. [Online].
- [24] M. Coope, "sensorland.com," [Online].
- [25] "http://www.electronics-tutorials.ws/," AspenCore. [Online].
- [26] "http://www.ni.com/white-paper/3642/en/," NI. [Online].
- [27] S. Y. a. J. P. Frangi, "Cup anemometer response to the wind turbulence – measurement of the horizontal wind variance," *Annales Geophysicae*, 2004.
- [28] L. Kristensen, "Cup Anemometer Behavior in Turbulent Environments," Risø National Laboratory, Roskilde, Denmark, 1998.
- [29] M. F. Jørgensen, N. L. Pedersen and J. N. Sørensen, "Aerodynamic and Mechanical System Modelling," Technical University of Denmark. Department of Mechanical Engineering, 2013.
- [30] J. Thirstrup Petersen, "Kinematically nonlinear finite element model of a horizontal axis wind turbine. Part 1: Mathematical model and results," Risø National Laboratory. Department of Meteorology and Wind Energy, Roskilde, Denmark, 1992.
- [31] A. M. H. Torben Juul Larsen, "How 2 HAWC2, the user's manual," Risø National Laboratory, DTU, Roskilde, Denmark, 2015.
- [32] M. O. L. Hansen, Aerodynamics of Wind Turbines, Technical University of Denmark: Routledge, 2015.
- [33] F. M. White, Fluid mechanics, McGraw-Hill, 2011.
- [34] "www.contrinex.com," CONTRINEX. [Online].
- [35] "www.me-systeme.de," ME-Meßsysteme GmbH. [Online].
- [36] "http://www.shop.fahrwind.de," VWA-Deutschland. [Online].
- [37] "www.aliexpress.com," Alibaba Group. [Online].

- [38] ["http://www.ni.com/white-paper/9401/en/,"](http://www.ni.com/white-paper/9401/en/) NI. [Online].
- [39] M. A. Siddiqui, ["https://www.slideshare.net/MuhammadAliSiddiqui6/fracture-mechanics-failure-analysislectures-fractography,"](https://www.slideshare.net/MuhammadAliSiddiqui6/fracture-mechanics-failure-analysislectures-fractography) 2016. [Online].
- [40] ["www.windspot.es,"](http://www.windspot.es) Sonkyo Energy. [Online].
- [41] ["windenergysolutions.nl,"](http://windenergysolutions.nl) WES. [Online].
- [42] S. Sureshkumar, "Aeroelastic Simulation of small Wind Turbine using HAWC2," Department of Mechanical Engineering, Blekinge Institute of Technology, Karlskrona, Sweden, 2014.
- [43] ["http://wincharger.com/,"](http://wincharger.com/) Wincharger. [Online].
- [44] ["http://www.weatherspares.co.uk/,"](http://www.weatherspares.co.uk/) Weather Spares. [Online].
- [45] ["www.hbm.com,"](http://www.hbm.com) Hottinger Baldwin Messtechnik GmbH. [Online].
- [46] ["thermopedia.com,"](http://thermopedia.com) [Online].
- [47] DTU Wind Energy, "HAWC2 E-lessons: Control".
- [48] ["http://www.ni.com/data-acquisition/what-is/,"](http://www.ni.com/data-acquisition/what-is/) National Instruments. [Online].
- [49] ["novalynx.com,"](http://novalynx.com) NovaLynx. [Online].
- [50] ["www.nrgsystems.com,"](http://www.nrgsystems.com) NRG Systems. [Online].
- [51] A. v. Breitenbach, "Dynamics of a free yawing downwind wind turbine," Institut für Strömungsmechanik und Technische Akustik (ISTA), FG Experimentelle Strömungsmechanik, TU Berlin, Berlin, 2016.
- [52] J. G. R.S. KHURMI, "14. Shafts," in *A Textbook of Machine Design*, New Delhi, EURASIA PUBLISHING HOUSE (PVT.) LTD., 2005, p. 1251.
- [53] R. M. Bruce Carter, *OP AMPS for everyone*, Texas Instruments, 2009.

APPENDICES

A. Wind measurement devices

Sonic anemometers (Figure 69), compared to cup anemometers, have the advantage that they can measure the three components of the wind speed, and they can reach higher sampling frequencies, around 10 and 20Hz [10]. Sonic anemometers present another advantage: since the sound speed depends on the temperature and the water vapor, they can also measure temperature, which can be used to estimate the buoyant heat flux, but this is not required for the present project.



Figure 69. Sonic anemometer.
Source: [55]

The vertical wind component is not needed to be measured, since it is usually very small. It is noteworthy to say that, with cup anemometers it is also possible to measure the three components by using two devices but, as said, this is not necessary.

However, a higher sampling frequency would provide more information, as explained in the ‘3.2.3. Data acquisition’ section, but this is not strictly necessary, and it does not justify the extra cost that a sonic anemometer would suppose.

LIDAR (Laser Imaging Detection And Ranging) (Figure 70) is based on the properties of light propagation. It has the advantage that it does not need a mast, and it can measure the wind speed at several points at the same time. This technology is, however, discarded because it is very expensive, and it also requires a lot of time to implement.



Figure 70. LIDAR. Source: [56]

B. Distance sensors

One of the simplest ways to measure the pitch angle is by using an angle encoder placed in the blade root. However, the lack of space to install it, added to the fact that the blade is in the rotor, and the signal would have been needed to be transferred wirelessly or by using a slip ring, led to the use of an indirect way to measure the pitch angle: the distance between the generator disc and the hub is related to the pitch angle, with an almost proportional relationship. The relationship between the position of the plate over the slider and the pitch angle can be calculated mathematically. The position of the slider, which has a variation of less than 20mm, can be measured from the nacelle with a distance sensor. After a first screening, three possible options have been selected:

- inductive distance sensor (Figure 71)
- Potentiometric distance sensor (Figure 72)
- Optical distance sensor (Figure 73)



Figure 71. Inductive distance sensor. Source: [34]



Figure 72. Potentiometric distance sensor. Source: [35]



Figure 73. Optical sensor. Source: [11]

Induction sensors can measure distance ranges up to around 30mm. Unlike potentiometric and optical sensors, induction sensors need a minimum area on the surface they measure the distance. This required area, for the commercial models found, was not fulfilled, and therefore these sensors have been discarded.

Potentiometric sensors present some drawbacks with respect to optical sensors, like low IP protection, e.g. IP40, and need of a physical contact. They have a ball or a roller on the tip, and it is not specified in the consulted datasheets how much speed can withstand the element on the tip.

The chosen optical sensor, although it is the most expensive option, it has IP65 protection and it does not need physical contact. Besides, as stated in section '3.2.1. Sensors', it has a significant advantage with respect to the potentiometric sensor: it can be used also as a rotational speed sensor.

C. Strain gages attachment

Once the configuration is defined, the strain gages can be attached. The procedure explained is not intended to be a tutorial on how to attach strain gages, but a summary of the steps done, focusing on some relevant aspects.

The followed procedure has been the following:

- The surface where the strain gage was going to be attached has been sanded with sandpaper in order to have a rugged surface where the glue can have more contact surface.
- The surface has been cleaned with 'M-prep conditioner' which is an acid product that cleans the surface, removing rust, paint, coatings, etc. Afterwards 'M-prep neutralizer' has been applied to neutralize any chemical reaction produced by the previous product. In both cases the surface has been dried with cotton sticks.
- With the help of a Vernier caliper and a scribe, the mid-points where the strain gages have to be attached have been marked. The strain gage has a mid-point mark that helps to position it more accurately.
- The strain gage has been stuck to a piece of adhesive tape using tweezers (it has to be avoided to touch the strain gage with the fingers), it has been stuck in its correct place, and afterwards the tape has been partially lifted in order to be able to access the bottom surface of the strain gage. This step is for the correct positioning of the strain gage.
- Catalyst for the glue has been spread over the side that will be in contact with the metal surface. A small amount of this has to be applied, only the necessary to leave a fine layer of catalyst on the surface.
- The glue has been applied on both sides and spread over the surfaces. Subsequently, it has been pressed with the fingers for some minutes, until the glue got consistent, in order to guarantee a correct settlement. The used glue was cyanoacrylate adhesive, which toughens fast (some minutes), but it could have also been used epoxy adhesive, which is stronger but takes around 6 hours to toughen.

After this step, something mentioned when talking about the crosstalk is revealed: it can be observed with the naked eye that some strain gages are slightly crooked. See Figure 74.

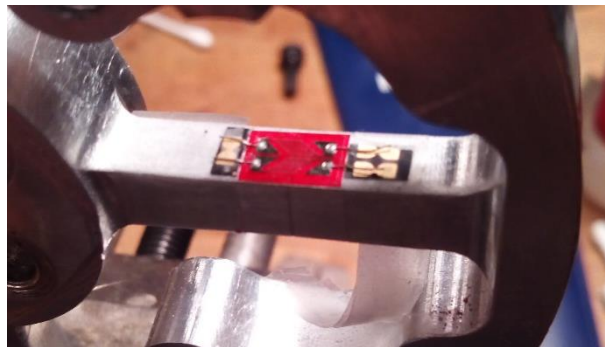


Figure 74. Shear strain gage with soldering terminals. The strain gage is slightly crooked.

- The soldering terminals (Figure 74) could have been glued at the same time as the strain gage, but it has been done afterwards for simplicity. The strain gage already includes the leads, and these have been soldered to the soldering terminals. In the case the leads had to be soldered, it would have to be done with low temperature, to not damage the strain gage.
- An optional step is to apply a protective coating, e.g. 'M-Coat A', to the strain gage. This step has not been done due to unavailability of the product.

Finally, the wires from the soldering terminals have been extended to another phase of soldering terminals, where the common cables in both strain gages in the Wheatstone bridge have been soldered together in order to extend only 4 cables for each bridge, instead of 6, up to the amplifier. See Figure 75.

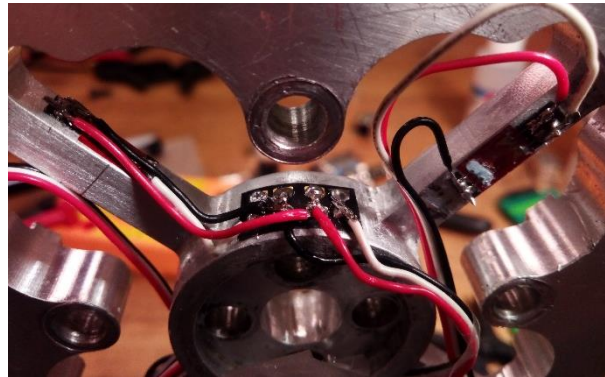


Figure 75. Intermediate phase of soldering terminals

The strain gages at this step are ready to measure, but before taking field measurements, a last task has to be done: calibration.

In order to calibrate the strain gage bridges, a portable amplifier has been used. The connection between the bridges and the amplifier has been built (Figure 76), and measurements at different weights have been taken for both torque and thrust.

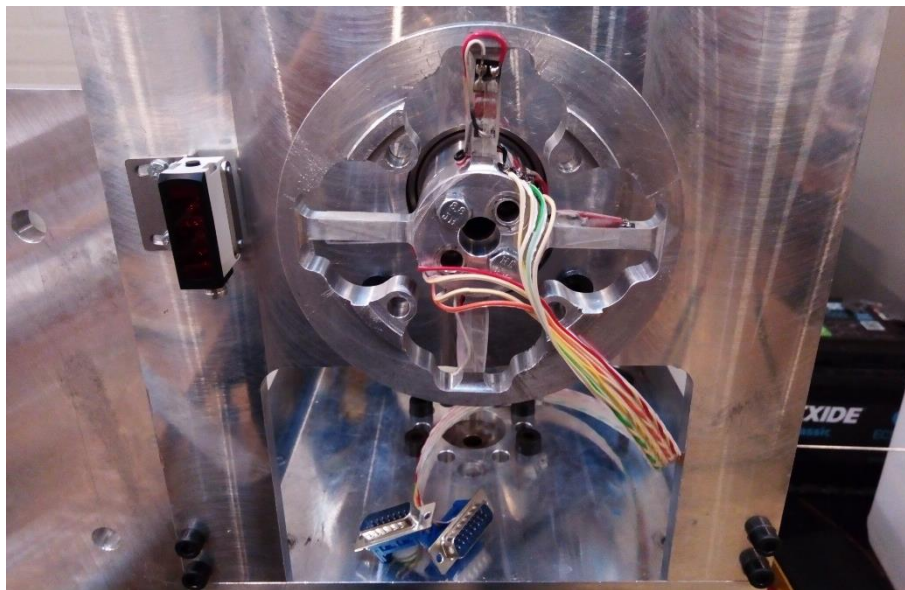


Figure 76. Thrust torque sensor prepared to be connected to the portable amplifier.

As the sensor is intended to be used on another amplifier, the signal (mV/V) vs weight (N), for the case of thrust, and signal (mV/V) vs moment (Nm) for the case of torque have been measured. Due to the absence of proper calibration weights, a plastic water container has been used, adding water previously weighted with a scale for each thrust measurement. For the case of torque, a rod has been used, placing the water container at different distances from the center of the sensor to obtain different moments. The results are shown in Figure 77.

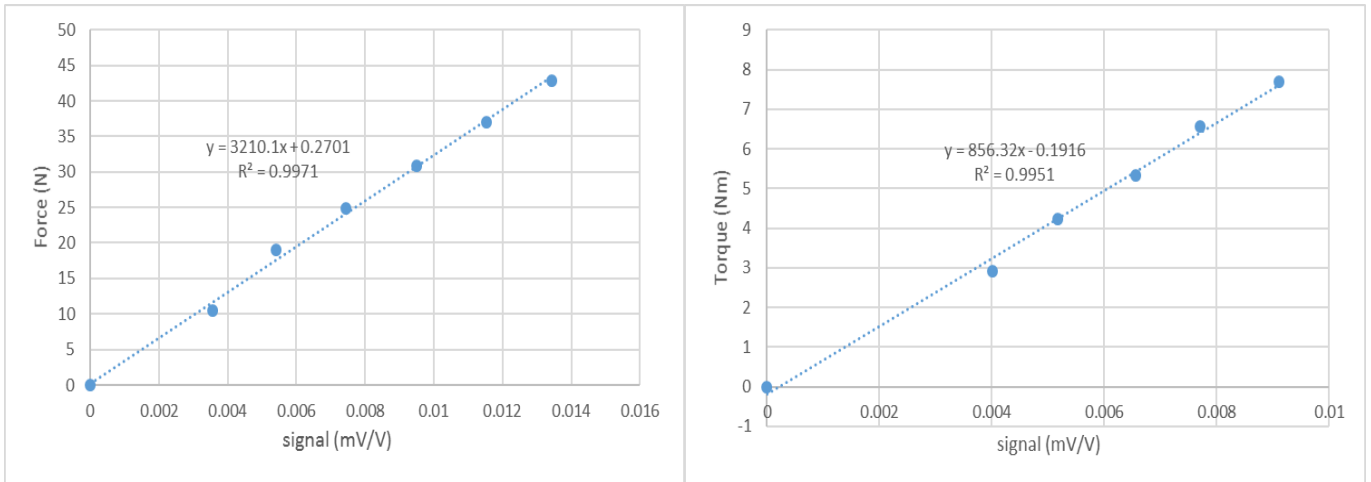


Figure 77. Calibration curves for thrust (left) and torque (right)

Figure 77 shows that the signal in function of the weight follows a linear trend. The coefficient of determination (R^2) is very close to 1 in both cases. That means the linear trendline fits very well the acquired data. From the equation of the trendline is found that the output signal in mV/V from the thrust bridge has to be multiplied by 3210 to obtain the thrust in N, and the output signal from the torque bridge has to be multiplied by 856 to obtain the torque in Nm.

The crosstalk from other components have been tried to be measured unsuccessfully, because the values were of the same order of magnitude as the noise in the amplifier. See Figure 78. So higher weights or a more accurate device would have been needed in order to calculate these small values.



Figure 78. Crosstalk measurement. In this figure can also be seen the utilized portable amplifier SCOUT55, and the water container.

D. Generator controllers

In the market, there are many different devices that work based on the explained DC-conversion mechanism. The available options are the following:

- Make a homemade generator controller.
- Frequency converter³⁴ (on-grid)
- Battery charger (off-grid)
- Electronic load

The first option has been discarded due to the impossibility³⁵ to find a DC-DC converter able to be controlled by a microcontroller. Building a homemade DC-DC converter would have supposed an excessive time.

For the second option, some products have been found, although they are scarce for so low power. For example, the WINDMASTER 500 (Figure 79) could fit in the system. However, this device does not allow much flexibility, since the power curve comes pre-set from the vendor and, besides, it does not follow Equation 4, but a straight ramp. Furthermore, it needs additional protection on the DC side. However, the decision of not to use this device came because we are not allowed to deliver power to the grid in the test field. So, an on-grid device cannot be used.



Figure 79. WINDMASTER 500. Source: [36]

An off-grid system, then, has to be used. On internet can be found many battery-charging systems for small wind turbines. However, manufacturers don't use to provide datasheet, so the characteristics of the device are difficult to known. No device that fits the requirements could be found. Figure 80 shows a system that fits the wind turbine. After a conversation with the manufacturer, an important fact has been noticed: when the generator exceeds the nominal power (500W), the extra power is dumped in the dump load. This means that the power output from the generator is not limited in any way.

³⁴ A frequency converter is a device composed of a rectifier, a DC-DC converter and an inverter.

³⁵ Do exist some programmable boards, for example from Texas Instruments, which can work as frequency converters, but this way has been disregarded as a recommendation from a professor due to the excessive time needed to learn and program these boards.



Figure 80. MPPT wind solar system controller with dump load. Source: [37]

The device, therefore, does not fit for this purpose.

E. More about measurement campaigns

Passive yaw system

The DTU SWT includes a bearing on its tower top to allow free yaw rotation. As already explained, the designed hub is prepared to work with a passive yaw system because the blades present a coning angle that allow to track the wind direction. However, the passive yaw system is not fully operative because the slip ring is not installed.

Fortunately, the Danish wind pattern, characterized by the predominance of westerly winds, coming from the North Sea, allowed us to use the SWT without blocking the yaw bearing. Figure 81 depicts the wind rose of the whole test in Risø. The figure evidences that the wind pattern was very directional. Hence, the passive yaw system could work freely because the cables were not in danger of being stretched due to rotation of the yaw.

The passive yaw system performed correctly in the field. However, in the wind tunnel output, it had to be blocked, because it turned due to gyroscopic effect. The responsible of this gyroscopic effect was the shear stress. The yaw turned clockwise. So, following the right-hand rule, the shear was stronger at the bottom than at the top.

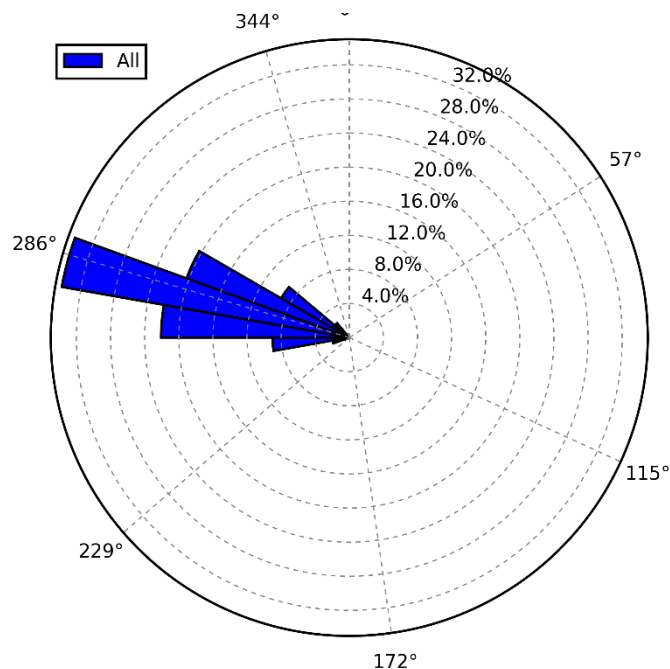


Figure 81. Risø field test wind rose. North corresponds to 0°.

Voltage and current from the generator

By plotting voltage and current from the measured data against the rotational speed (Figure 82), it can be seen what has been stated when the generator has been presented: the voltage is proportional to the rotational speed, and the current is proportional to the torque (therefore, proportional to the square of the rotational speed). Note that the relationships that can be derived from Figure 82 do not match with the optimal point found in Table 4. This is because the pitch angle is not 0 due to wind fluctuations along the test.

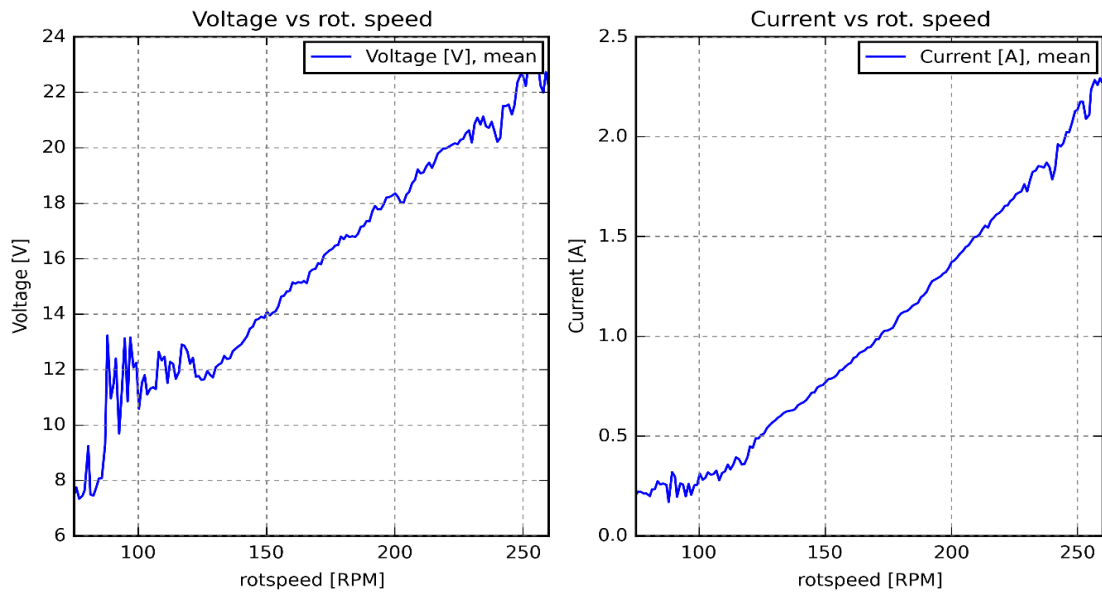


Figure 82. Voltage and current vs rotational speed

Finding the MPP

In Table 4, the values of the found optimal point have been presented. The recorded time-series from the experiment are shown in Figure 83. The figure shows that the current is slowly increased. At the same time, the pitch angle decreases because the torque increases. Around $t=370s$, the torque exceeds its optimum value and the rotational speed starts to decrease, but the current is quickly redirected. The MPP is found at around $t=400$ where, if the torque increases or decreases, the power decrease. The wind speed is plotted to show that it remains constant, although the value is not real, as demonstrated in section ‘4.1. Wind tunnel outlet’. The spikes in the power and the current are not real, but the post processing tool could not eliminate. These spikes are caused by the electronic load DAQ.

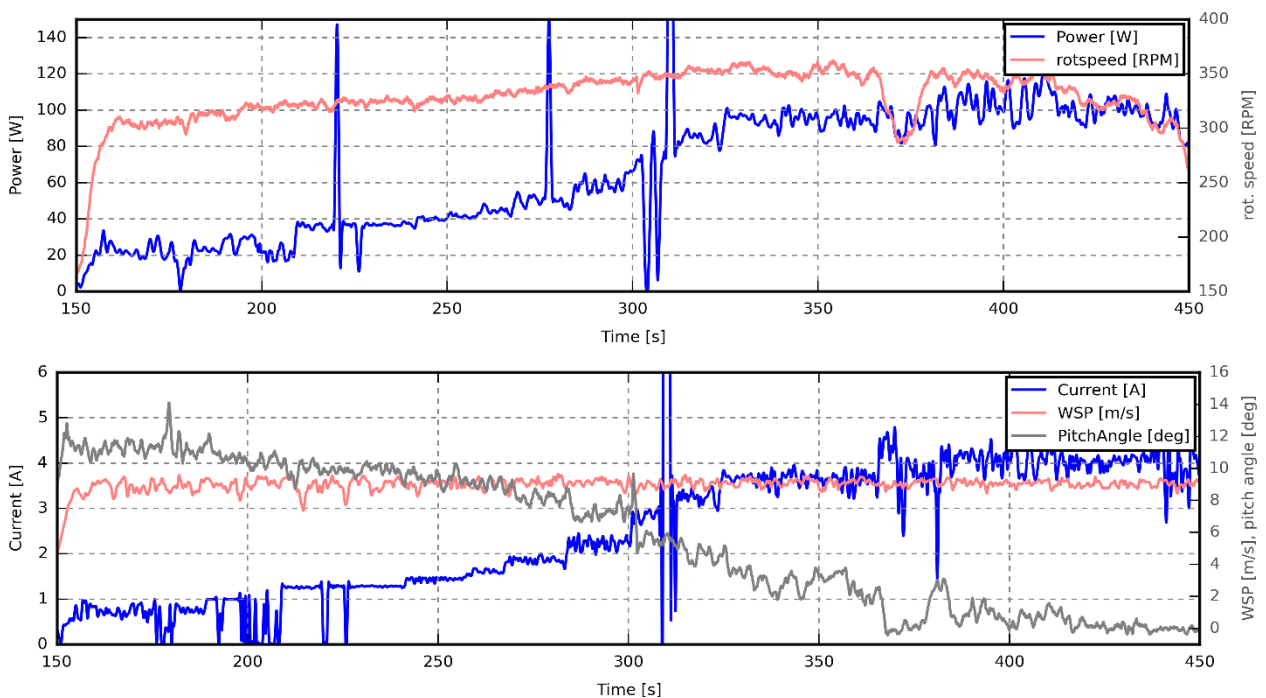


Figure 83. Time-series of the experiment for finding the MPP in the wind tunnel outlet.

F. Mann model

The Mann model is a wind turbulence model. In the Mann model, the wind field is contained in a ‘turbulence box’, which is a 3D matrix with wind speed values. The third dimension is the time, which can be seen as another space dimension, but it moves when the simulation time advances.

The Mann model is based on the von Karman turbulence model, which considers an isotropic turbulent field. In the Mann model, the von Karman turbulent field is distorted by a velocity shear. This distortion is defined by an extra parameter called ‘shear distortion parameter’ (γ). This parameter allows to have into account the stability effects in the surface layer of the atmosphere.

Stability in the surface layer depends on the heat flux between the ground and the air, having unstable conditions when it is sunny (heat transfer from the ground to the air), neutral conditions when it is cloudy (no heat transfer) and stable conditions at night (heat transfer from the air to the ground). For neutral conditions, a shear distortion parameter of $\gamma=3.9$ is obtained, best-fitting with the aforementioned Kaimal spectrum.

The atmospheric conditions were not neutral during the field test. It was sunny. Thus, unstable conditions were given. To quantify the stability effect, the Obukhov length scale (L) (Equation 12) is used.

$$L = -\frac{T_0}{\kappa g} \frac{u_*^3}{Q_0} \quad (12)$$

Where T_0 is the surface air temperature, κ the von Karman constant, g the gravity, u_* the friction velocity, and Q_0 the heat flux from the ground to the air.

From these parameters, both friction velocity and heat flux need the vertical wind component to be calculated. As the vertical wind component has not been measured, the Obukhov length scale is unknown.

If the Obukhov length scale cannot be calculated, would it be reasonable to assume neutral conditions?

At the latitude of the Risø test field (55.8°) on December 4th, the Sun altitude reaches a maximum altitude of 12° during the noon, with respect to the horizon. At this altitude, which is very low, the sun rays arrive very tilted, transferring a small amount of heat to the Earth surface. Therefore, assuming neutral conditions is not a big issue.

G. Arduino code for distance sensor and anemometer

```
1. int pulsePin = 3; //it has to be 2 or 3 because of the interrupt routine
2. volatile unsigned int counter = 0;
3. volatile unsigned long ContactBounceTime; // Timer to avoid contact
   bounce in isr
4. unsigned long period = 0, period4=0;
5. unsigned long start = 0, start4=0;
6. float velocity = 0;
7. unsigned int duration = 333; //(ms) sampling frequency of the anemometer
   is 3Hz
8. int const wDirPin=A0;
9. int wDir=0;
10. int potVal=0, potValBefore=0;
11. int pulsePinRPM = 2; //it has to be 2 or 3 because of the interrupt
   routine
12. volatile int countRPM = 0;
13. volatile unsigned long ContactBounceTime2; // Timer to avoid contact
   bounce in isr
14. unsigned long period2 = 0, period3=0;
15. unsigned long start2 = 0, start3=0;
16. float RPM = 0;
17. unsigned int duration2 = 10; //(ms) sampling period for optical sensor
18. int const distance=A1;
19. int potVal2=0;
20.
21.
22. void setup()
23. {
24.   pinMode(pulsePin, INPUT);
25.   pinMode(pulsePinRPM, INPUT);
26.   // enable the 20K pull-up resistor to steer
27.   // the input pin to a HIGH reading.
28.   attachInterrupt(digitalPinToInterrupt(pulsePin), ISR1, RISING);
29.   attachInterrupt(digitalPinToInterrupt(pulsePinRPM), ISR2, RISING);
30.   Serial.begin(115200);
31. }
32.
33. void loop()
34. {
35.   //Anemometer
36.
37.           //Wind speed
38.   period4=millis()-start4;
39.   if (counter!=0){
40.     start4=millis();
41.     velocity=1005.81135*counter/period4; //m/s
42.     counter=0;
43.   }
44.   if (period4>1000){
45.     velocity=0;
46.   }
47.   period=millis()-start;
48.   if (period >= duration){
```

```
49.   start=millis();
50.   //Wind direction
51.   potVal=analogRead(wDirPin);
52.   if (potVal!=potValBefore){
53.     potValBefore=potVal;
54.     wDir=map(potVal,0,1023.0,0,360.0);
55.   }
56.   //Serial.print("wdir: ");
57.   Serial.print(wDir);
58.   //Serial.print(", wsp: ");
59.   Serial.print(",");
60.   Serial.println(velocity);
61. }
62. //optical
63.   //RPM
64.   period3=millis()-start3;
65.   if (countRPM!=0){
66.     start3=millis();
67.     RPM=60.*1000./period3*countRPM/3.; //rpm
68.     countRPM=0;
69.   }
70.
71.   period2=millis()-start2;
72.   if (period2 >= duration2){
73.     start2=millis();
74.
75.     //distance
76.     potVal2=analogRead(distance);
77.
78.     //Serial.print("potVal: ");
79.     Serial.print(potVal2);
80.     //Serial.print(", RPM: ");
81.     Serial.print(" ");
82.     Serial.println(RPM);
83.   }
84.
85. }
86.
87. void ISR1(){
88.   if((millis() - ContactBounceTime) > 15 ) { // debounce the switch
      contact.
89.     counter++;
90.     ContactBounceTime = millis();
91.   }
92. }
93. void ISR2(){
94.   if((millis() - ContactBounceTime2) > 15 ) { // debounce the switch
      contact.
95.     countRPM++;
96.     ContactBounceTime2 = millis();
97.   }
98. }
```

H. Post-processing code

```

1. clear
2. close all
3.
4. % Inputs
5. date='171127_174138'; % format: yymmdd_HHMMSS
6. opti0deg=290; %value from 0-1024 in the distance sensor which
   corresponds to 0 deg pitch angle
7.
8. % Collect data
9.
10. dataset=importdata(char(strcat('res\opti',date,'.csv')));
11. dataset=dataset.data;
12.
13. optiTime = dataset(:,1); %ms random beginning in LabVIEW
14. optiRPM = dataset(:,2); %RPM - no change needed
15. optiDist = dataset(:,3); %(adim.) values from 0 to 1023
16.
17. %anemometer
18. dataset=importdata(char(strcat('res\anem',date,'.csv')));
19. dataset=dataset.data;
20.
21. anemTime = dataset(:,1); %ms random beginning in LabVIEW
22. anemWdir = dataset(:,2); %° wind direction from north - no change
   needed
23. anemWSP = dataset(:,3); %m/s wind speed
24.
25. %electronic load
26. dataset=importdata(char(strcat('res\EL',date,'.csv')));
27. dataset=dataset.data;
28.
29. ELTime = dataset(:,1); %ms random beginning in LabVIEW
30. ELp = dataset(:,2); %W Power from generator
31. ELv = dataset(:,3); %V values from 0 to 1023
32. ELr = dataset(:,4); %Ohm values from 0 to 1023
33. ELc = dataset(:,5); %A values from 0 to 1023
34.
35. %data conditioning
36. % Elapsed time
37. optiTime=(optiTime-optiTime(1))/1000;%s relative time from the
   beginning
38. anemTime=(anemTime-anemTime(1))/1000;%s relative time from the
   beginning
39. ELTime=(ELTime-ELTime(1))/1000;%s relative time from the beginning
40.
41. % Angle
42. for i=2:length(optiRPM)
43.     if optiRPM(i)~=optiRPM(i-1) %in each RPM variation for sure
       there is wrong measurement
44.         if optiRPM>100 %the lower the rot speed, the longer the
           perturbation
45.             optiDist(i-1:i+1)=NaN;
46.         else
47.             optiDist(i-2:i+2)=NaN;
48.         end
49.     end
50. end
51. optiDist=optiDist(1:length(optiTime));
52. for i=3:length(optiDist)-2
53.     if optiDist(i)>=optiDist(i-1)+70 || optiDist(i)<=optiDist(i-1)-
70

```

```

54.         if optiRPM>100
55.             optiDist(i-1:i+1)=NaN;
56.         else
57.             optiDist(i-3:i+3)=NaN;
58.         end
59.     end
60. end
61. for i=2:length(optiDist)
62.     if isnan(optiDist(i))
63.         optiDist(i)=optiDist(i-1);
64.     end
65. end
66.
67. maxAngle=35;
68. optiAngle=(maxAngle-0)/(1024-opti0deg)*(optiDist-opti0deg)+0;
69.
70. windowSize = 10;
71. b = (1/windowSize)*ones(1,windowSize);
72. a = 1;
73. optiAngle = filter(b,a,optiAngle);
74.
75. figure(1)
76. plot(optiTime,optiRPM)
77. title('before filter')
78. yyaxis right
79. plot(optiTime,optiAngle)
80. ylabel('Pitch angle (deg)')
81. xlabel('time(s)')
82. ylabel('rot. speed (RPM)')
83.
84.     %filter rot.speed
85. windowSize = 30;
86. b = (1/windowSize)*ones(1,windowSize);
87. a = 1;
88. optiRPMf = filter(b,a,optiRPM);
89.     %filter pitch
90. windowSize = 100;
91. b = (1/windowSize)*ones(1,windowSize);
92. a = 1;
93. optiAnglef = filter(b,a,optiAngle);
94.
95.     %EL
96. for i=2:length(ELTime)
97.     if ELp(i)>310 || abs(ELp(i)-ELp(i-1))>20
98.         ELp(i)=NaN;
99.         ELv(i)=NaN;
100.         ELc(i)=NaN;
101.         ELr(i)=NaN;
102.     end
103. end
104.
105. for i=2:length(ELp)
106.     if isnan(ELp(i))
107.         ELp(i)=ELp(i-1);
108.     end
109. end
110. for i=2:length(ELv)
111.     if isnan(ELv(i))
112.         ELv(i)=ELv(i-1);
113.     end
114. end
115. for i=2:length(ELc)
116.     if isnan(ELc(i))

```

```

117.         ELC(i)=ELC(i-1);
118.     end
119. end
120. for i=2:length(ELr)
121.     if isnan(ELr(i))
122.         ELr(i)=ELr(i-1);
123.     end
124. end
125.
126. windowSize = 3;
127. b = (1/windowSize)*ones(1,windowSize);
128. a = 1;
129. ELpf = filter(b,a,ELp);
130.
131. % Resample
132.
133. [optiRPMr,optiTimer]=resample(optiRPMf,optiTime); %for a
constant sampling frequency
134. optiAngler=resample(optiAnglef,optiTime);
135. [anemWSPr,anemTimer]=resample(anemWSP,anemTime);
136. anemWdirr=resample(anemWdir,anemTime);
137. [ELpr,ELTimer]=resample(ELpf,ELTime);
138. ELcr=resample(ELc,ELTime);
139. ELvr=resample(ELv,ELTime);
140. ELrr=resample(ELr,ELTime);
141.
142. optifs=optiTimer(end)\length(optiTimer);
143. anemfs=anemTimer(end)\length(anemTimer);
144. ELfs=ELTimer(end)\length(ELTimer);
145.
146.
147. fs=65;
148. TimeEnd=min([optiTime(end),anemTime(end),ELTime(end)]);
149. Time=0:1/fs:TimeEnd;
150.
151. method='spline';
152.
153. optiRPMr=interp1(optiTimer,optiRPMr,Time,method);
154. optiAngler=interp1(optiTimer,optiAngler,Time,method);
155. anemWSPr=interp1(anemTimer,anemWSPr,Time,method);
156. anemWdirr=interp1(anemTimer,anemWdirr,Time,method);
157. ELpr=interp1(ELTimer,ELpr,Time,method);
158. ELvr=interp1(ELTimer,ELvr,Time,method);
159. ELcr=interp1(ELTimer,ELcr,Time,method);
160. ELrr=interp1(ELTimer,ELrr,Time,method);
161.
162. % Calculate torque
163. Torque=ELpr./(optiRPMr*pi/30);
164. Torque(isnan(Torque))=0;
165. %Plots
166. figure(2)
167. plot(optiTime,optiRPMf)
168. hold on
169. plot(Time,optiRPMr)
170. ylabel('rot. speed (RPM)')
171. yyaxis right
172. plot(optiTime,optiAnglef)
173. ylabel('Pitch angle (deg)')
174. xlabel('time(s)')
175. title('after filter')
176. saveas(gcf,char(strcat('plots\RPMvsAngle',date)),'fig')
177.
178. [anemWSPr2,anemTimer2]=resample(anemWSP,anemTime,65,'linear');
179.

```

```
180. figure(3)
181. plot(anemTime,anemWSP,'linewidth',1.5)
182. ylabel('rot. speed (RPM)')
183. hold on
184. plot(Time,anemWSPr,'linewidth',1.5)
185. plot(anemTimer2,anemWSPr2,'linewidth',1.5)
186. xlabel('time(s)')
187. ylabel('WSP (m/s)')
188. legend('raw data','without anti-aliasing','with anti-aliasing')
189. saveas(gcf,char(strcat('plots\RPMvsWSP',date)),'fig')
190.
191. figure(4)
192. plot(ELTime,ELp)
193. ylabel('Power (W)')
194. xlabel('time(s)')
195. hold on
196. plot(Time,ELpr)
197. yyaxis right
198. plot(ELTime,ELr)
199. ylabel('Resistance (Ohm)')
200.
201. %Export to CSV
202. filename=char(strcat('res\results',date,'.csv'));
203. pdapMatrix=[Time;optiRPMr;optiAngler;anemWSPr;anemWdirr;ELpr;ELv
r;ELrr;ELcr;Torque]';
204. title='Time,rotspeed,PitchAngle,WSP,Wdir,Power,Voltage,Resistanc
e,Current,Torque';
205. units='s,RPM,deg,m/s,deg,W,V,Ohm,A,Nm';
206.
207. fid = fopen(filename,'w');
208. fprintf(fid,'%s\r\n',title);
209. fprintf(fid,'%s\r\n',units);
210. fclose(fid);
211.
212. dlmwrite(filename, pdapMatrix,'-append','delimiter','');
```

I. PSD code

Main Code

```
clear
close all
% %generated kaimal
% U=mean(u);
% Uvar=var(u);
% Y=kaimal_spectra_generator_fun(U,Uvar,fs,z);
% u=Y;
% wind_spectrum_fun(u,fs,z,1)

% %RISO
% data1=importdata('anem171204_1h.csv');
% u=data1.data(:,3);
% fs=3;
% z=1.5;%m measurement height
% wind_spectrum_fun(u,fs,z,1)

%CUP
data1=importdata('anem171204_1h.csv');
u=data1.data(:,3);
fs=3;
z=1.5;%m measurement height
wind_spectrum_fun_corrCUP(u,fs,z,1)

%WTO
data1=importdata('anem171215_123314_1h3ms.csv');
u=data1.data(:,3);
wind_spectrum_fun_corrCUP(u,fs,z,0)
%finish plots
figure(1)
grid on
xlabel('f[Hz]')
ylabel('S(f) [m^2/s^2]')
legend('u')
hold off
saveas(gcf,'q1_1','eps')

figure(2)
grid on
% loglog([0.05 0.05],[0.001 1],'--','linewidth',2,'color','r')
% text(0.08,0.002,'inertial
effects','HorizontalAlignment','left','color','r');
% loglog([0.8 0.8],[0.001 1],'--','linewidth',2,'color','r')
% text(1,0.002,'signal +
white','HorizontalAlignment','left','color','r');

xlabel('f[Hz]')
ylabel('f·S(f)/\sigma^2 [dimensionless]')
xlim([1e-3 0.6])
% legend('Test field','Kaimal IEC 1.5','Test field corrected')
legend('Test field','Kaimal IEC 1.5','Wind tunnel outlet')
hold off
saveas(gcf,'q1_4','eps')
```

PSD without cup anemometer correction

```

function wind_spectrum_fun(u, fs, z, draw_kaimal)

% Mean and variance

U=mean(u);
Uvar=var(u);

% Time spectrum

N=length(u);

% FFT
Sf=fft(u); %Fourier transform
P2 = abs(Sf/N); %two-sided spectrum
mean1h=P2(1);
% PSD
Pyy2 = Sf.*conj(Sf)/N;%double sided normalized by the total time
Pyy1 = 2*Pyy2(1:floor(N/2));%single sided spectrum
f = fs/N*(0:N/2-1);

figure(1)
loglog(f(2:end),Pyy1(2:end)) %the first point is related to the
mean
hold on

%Check normalization
Uvar_psd=mean(Pyy1(2:end))/2; %var of the double-sided psd should
be the same as the var of time series

% Point 4: filter

a=-3;%starting decade
b=1;%ending decade
n=30;%spectral estimates per decade
fslog=logspace(a,b,n*(b-a));

bin=zeros(length(fslog),1);
count=zeros(length(fslog),1);
for i=2:length(fslog)
    for j=1:N/2
        if f(j)<fslog(i) && f(j)>fslog(i-1)
            bin(i)=bin(i)+Pyy1(j);
            count(i)=count(i)+1;
        end
    end
end
Pyyf=bin./count;
flog=fslog(~isnan(Pyyf));
Pyyf=Pyyf(~isnan(Pyyf));

PyyND=flog'.*Pyyf/Uvar/fs; %dimensionless PSD

figure(2)
loglog(flog,PyyND,'LineWidth',1);
hold on

if draw_kaimal==1
    %Kaimal fit
    if z<60
        Lu=0.7*z*8.1;
    else

```

```
Lu=42*8.1;%integral scale , where 42 is the scale
parameter for zhub>60m
end
KaimalND=4*flog*Lu/U./(1+6*flog*Lu/U).^ (5/3);
figure(2)
plot(flog,KaimalND,'linewidth',1)
end
```

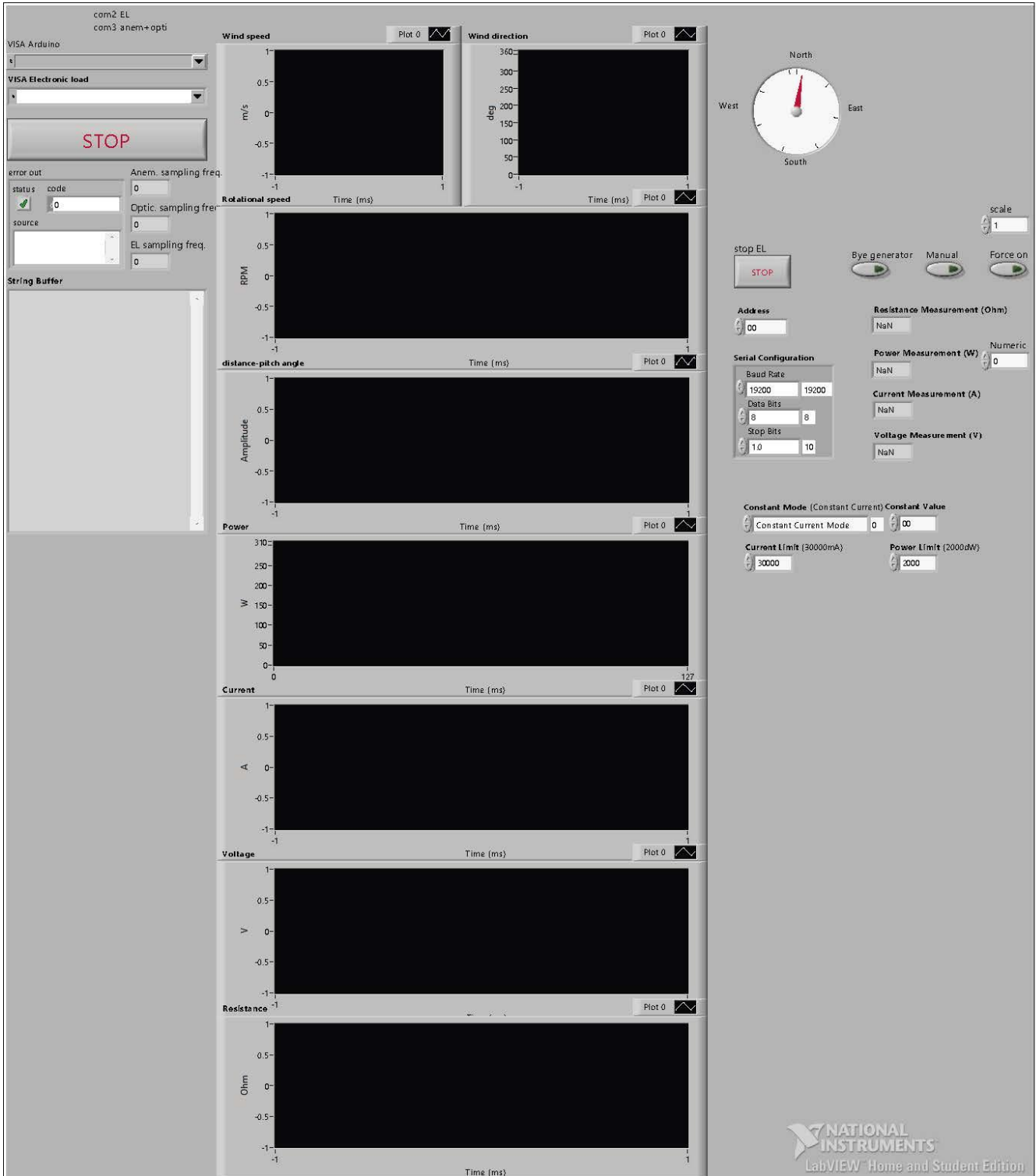
PSD with cup anemometer correction

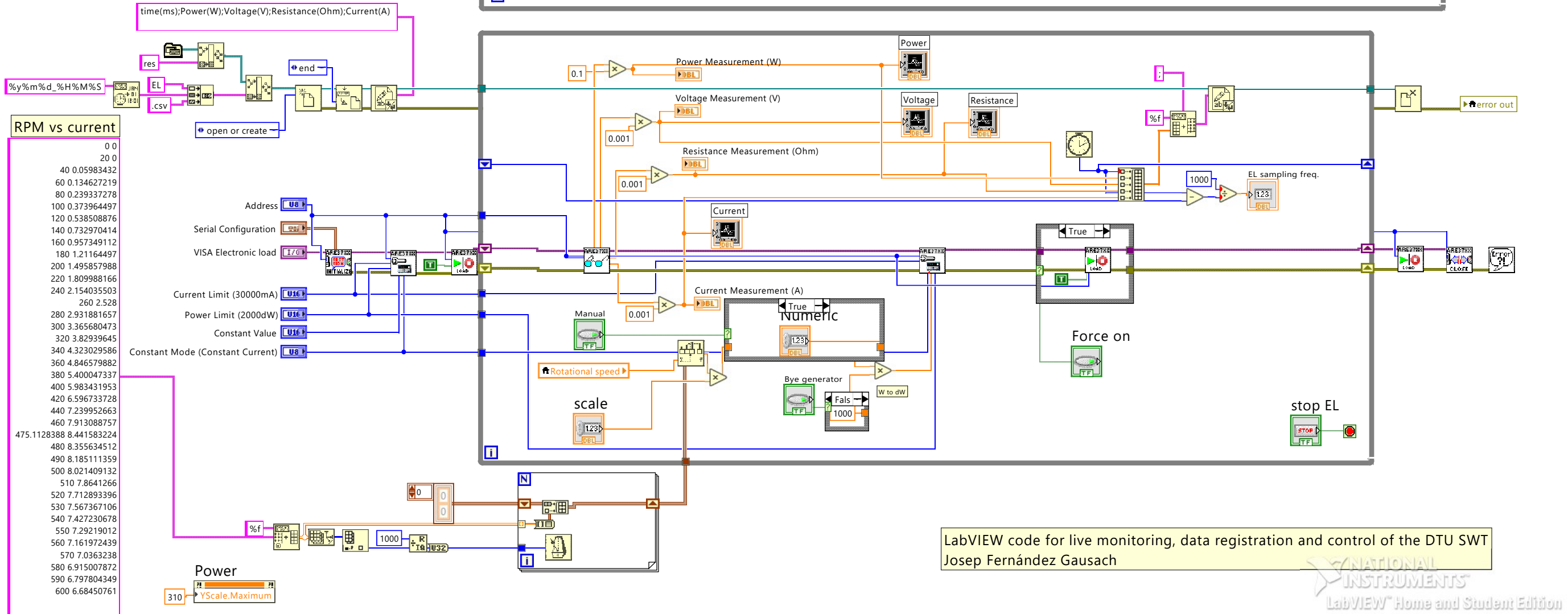
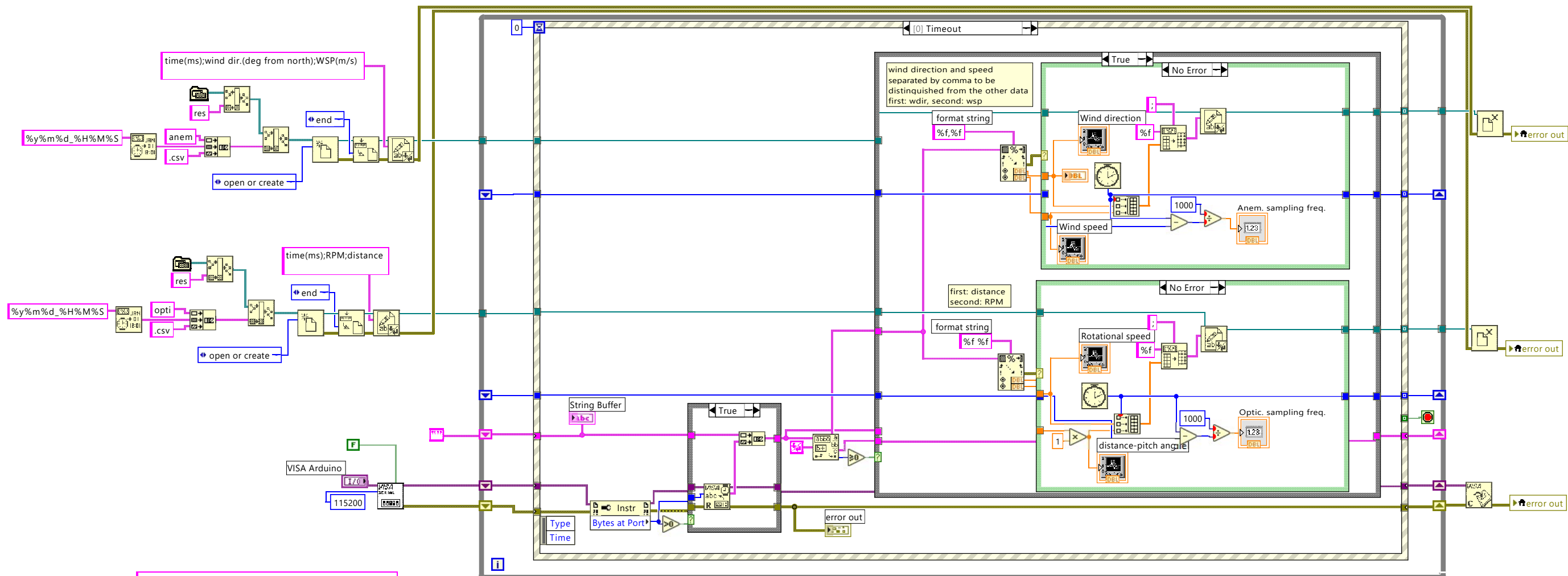
```
function wind_spectrum_fun_corrCUP(u,fs,z,draw_kaimal)
% Mean and variance
U=mean(u);
Uvar=var(u);
% Time spectrum
N=length(u);
% FFT
Sf=fft(u); %Fourier transform
P2 = abs(Sf/N); %two-sided spectrum
meanlh=P2(1);
% PSD
Pyy2 = Sf.*conj(Sf)/N;%double sided normalized by the total time
Pyy1 = 2*Pyy2(1:floor(N/2));%single sided spectrum
f = fs/N*(0:N/2-1);
figure(1)
loglog(f(2:end),Pyy1(2:end)) %the first point is related to the
mean
hold on
%Check normalization
Uvar_psd=mean(Pyy1(2:end))/2; %var of the double-sided psd should
be the same as the var of time series
% Point 4: filter
a=-3;%starting decade
b=1;%ending decade
n=30;%spectral estimates per decade
fslog=logspace(a,b,n*(b-a));
bin=zeros(length(fslog),1);
count=zeros(length(fslog),1);
for i=2:length(fslog)
    for j=1:N/2
        if f(j)<fslog(i) && f(j)>fslog(i-1)
            bin(i)=bin(i)+Pyy1(j);
            count(i)=count(i)+1;
        end
    end
end
Pyyf=bin./count;
flog=fslog(~isnan(Pyyf));
Pyyf=Pyyf(~isnan(Pyyf));
%Cup anemometer correction
L=3;%Distance constant, obtained by fitting curve to Kaimal
```

```
PyfCUP=Pyf.*(1+(2*pi*flog').^2*L^2/U^2);  
PyND=flog'.*PyfCUP/Uvar/fs; %dimensionless PSD  
  
figure(2)  
loglog(flog,PyND,'LineWidth',1);  
hold on  
  
if draw_kaimal==1  
    %Kaimal fit  
    if z<60  
        Lu=0.7*z*8.1;  
    else  
        Lu=42*8.1;%integral scale , where 42 is the scale  
        parameter for zhub>60m  
    end  
    KaimalND=4*flog*Lu/U./(1+6*flog*Lu/U).^ (5/3);  
  
    figure(2)  
    plot(flog,KaimalND,'linewidth',1)  
end
```

J. LabVIEW code

In this page, the front panel of the code for live monitoring, recording the acquired data and controlling the DTU SWT is shown. In the next page is attached the block diagram of the code.

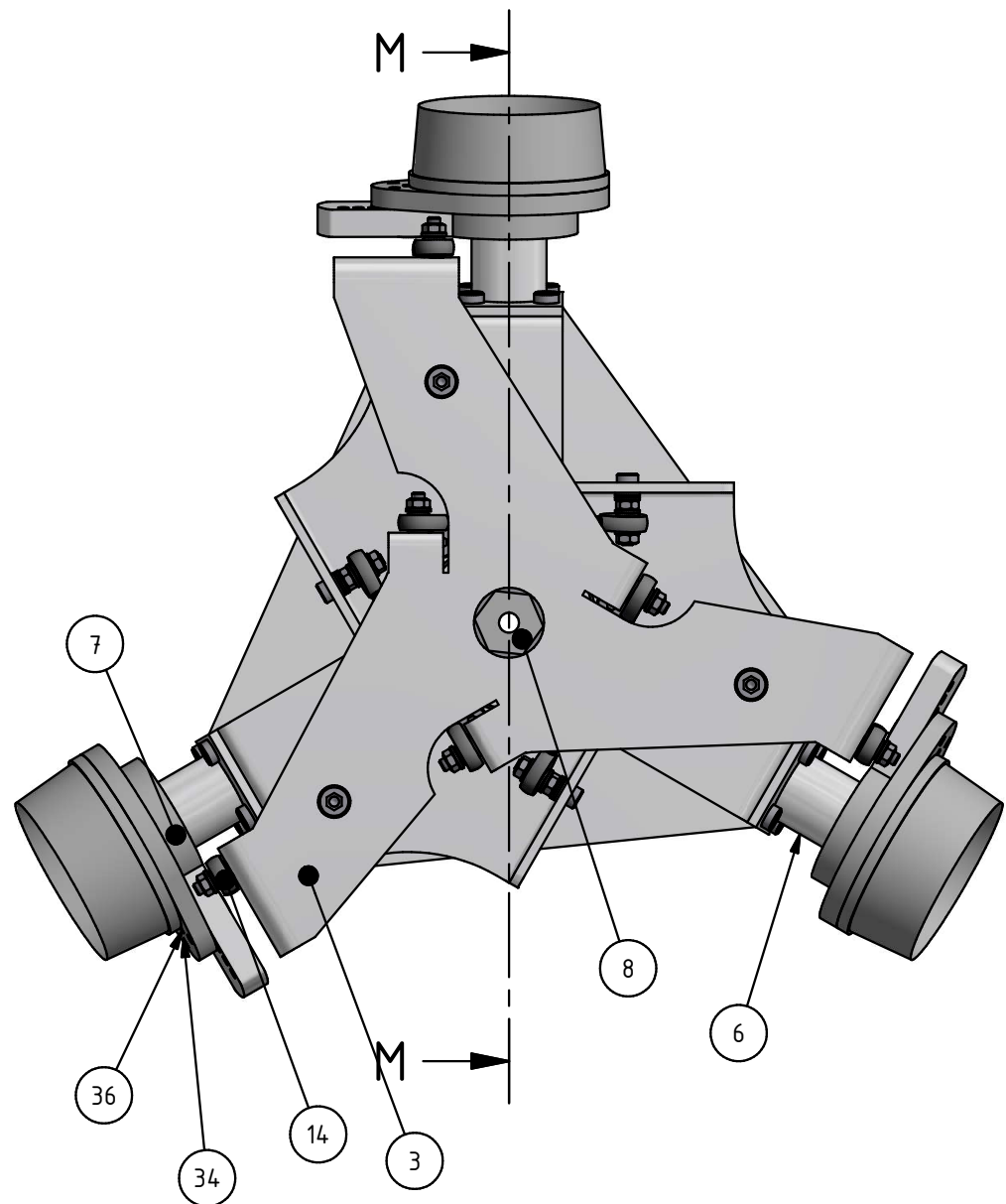




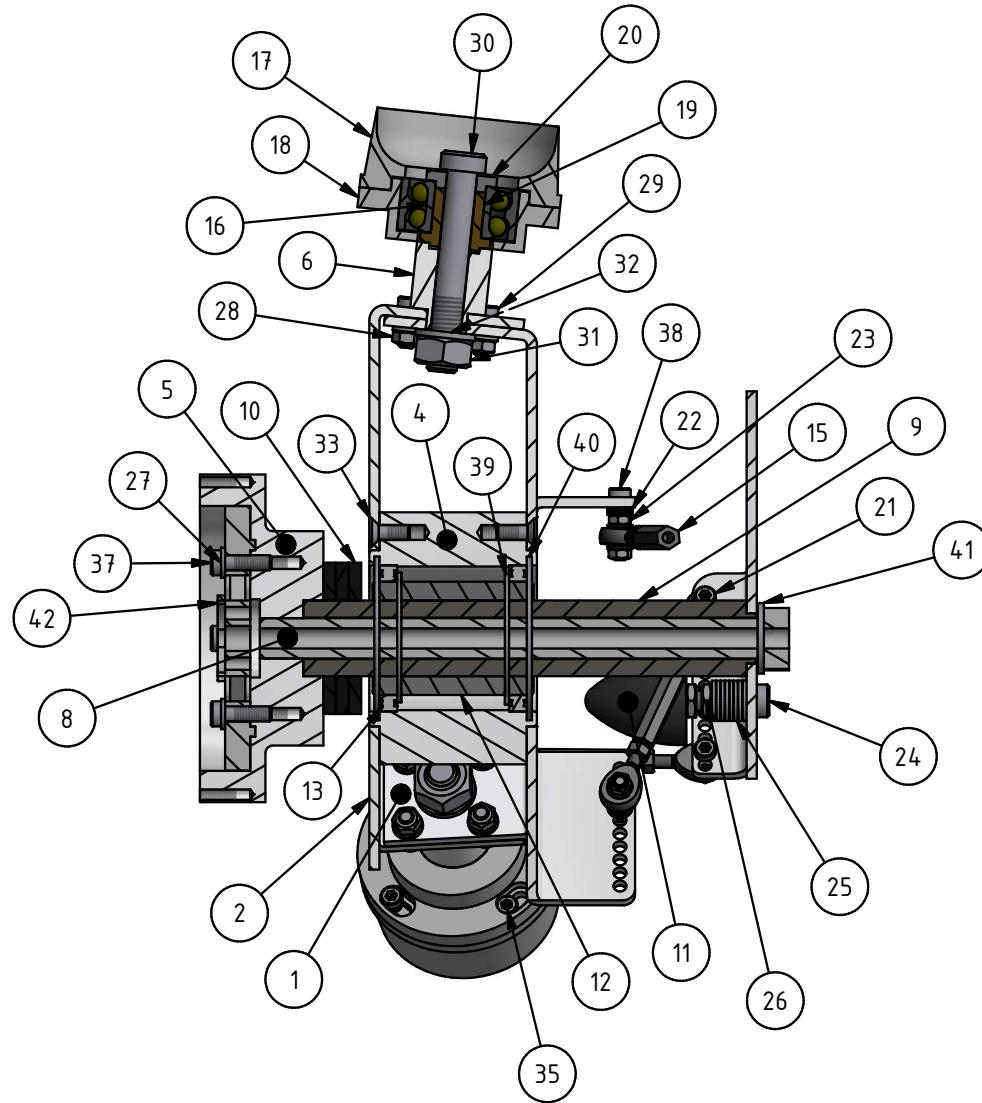
LabVIEW code for live monitoring, data registration and control of the DTU SWT
 Josep Fernández Gausach

K. Drawings

1. Overview
2. Hub sheet 1
3. Hub sheet 2
4. Generator disc
5. Bearing base
6. Slider base
7. Blade base
8. Pitching support arm
9. Hex screw M16
10. Slider
11. Bending moment sensor



M-M (1 : 3)



PARTS LIST

ITEM	QTY	PART NUMBER
1	1	Hub_Sheet 1
2	1	Hub_Sheet 2
3	1	Generator disc
4	1	Bearing Base
5	1	Slider base
6	3	Blade base
7	3	Pitching support arm
8	1	Hex screw M16
9	1	Slider
10	3	Bumper in
11	3	Bumper out
12	1	Linear bearing
13	2	Roller bearing
14	13	Joint bearing
15	6	Lever arm rod
16	3	Blade bearing
17	3	Blade root blade
18	3	Blade root hub
19	3	Blade bearing support 1
20	3	Blade bearing support 2
21	9	DIN 6912 - M5 x 20
22	24	DIN 125 - A 5,3
23	12	DIN 555-5 - M5
24	3	DIN 6912 - M8 x 40
25	24	DIN 125 - A 8,4
26	6	DIN 439 - M8
27	16	DIN 125 - A 6,4
28	12	DIN 555-5 - M6
29	12	DIN 6912 - M6 x 16
30	3	DIN 6912 - M12 x 80
31	3	DIN 555-5 - M14
32	3	DIN 125 - A 13
33	18	DIN 7991 - M6 x 16
34	3	DIN 7991 - M5 x 20
35	12	DIN 6912 - M5 x 12
36	3	DIN 7991 - M6 x 20
37	4	DIN3 6912 - M6 x 20
38	3	DIN 6912 - M5 x 25
39	2	DIN 471 - 42 x 1.75
40	2	DIN 472 - 62x2
41	1	ISO 7092 - ST 16 - 140 HV
42	1	Thrust-torque sensor

Diese Zeichnung und die darin enthaltene Information unterliegt dem Urheberrecht! Das Nutzen, Kopieren und Weitergeben bedarf der Zustimmung des Erstellers.
Schutzvermerk nach DIN ISO 16016 beachten!

enbreeze GmbH Tel. +49 30 98 61 27 10
Marzahner Str. 34 Fax. +49 30 51 30 45 85
13053 Berlin

www.enbreeze.com info@enbreeze.com

Allgemeintoleranzen nach DIN ISO 2768-1		Grenzabmaße in mm für Normalbereich in mm		Grenzmaße für Längenmaße	
Toleranzklasse	0,5	über 0,5	über 3	über 30	über 120
f (mm)	±0,05	±0,05	±0,10	±0,15	±0,2
M (mm)	±0,10	±0,10	±0,20	±0,30	±0,5
H (mm)	±0,15	±0,20	±0,30	±0,50	±1,0
g (sehr groß)	±0,50	±1,00	±1,50	±2,5	±4,0

Zust.	Änderungen	Datum	Name

Oberfläche Maßstab 1:3 Position Menge

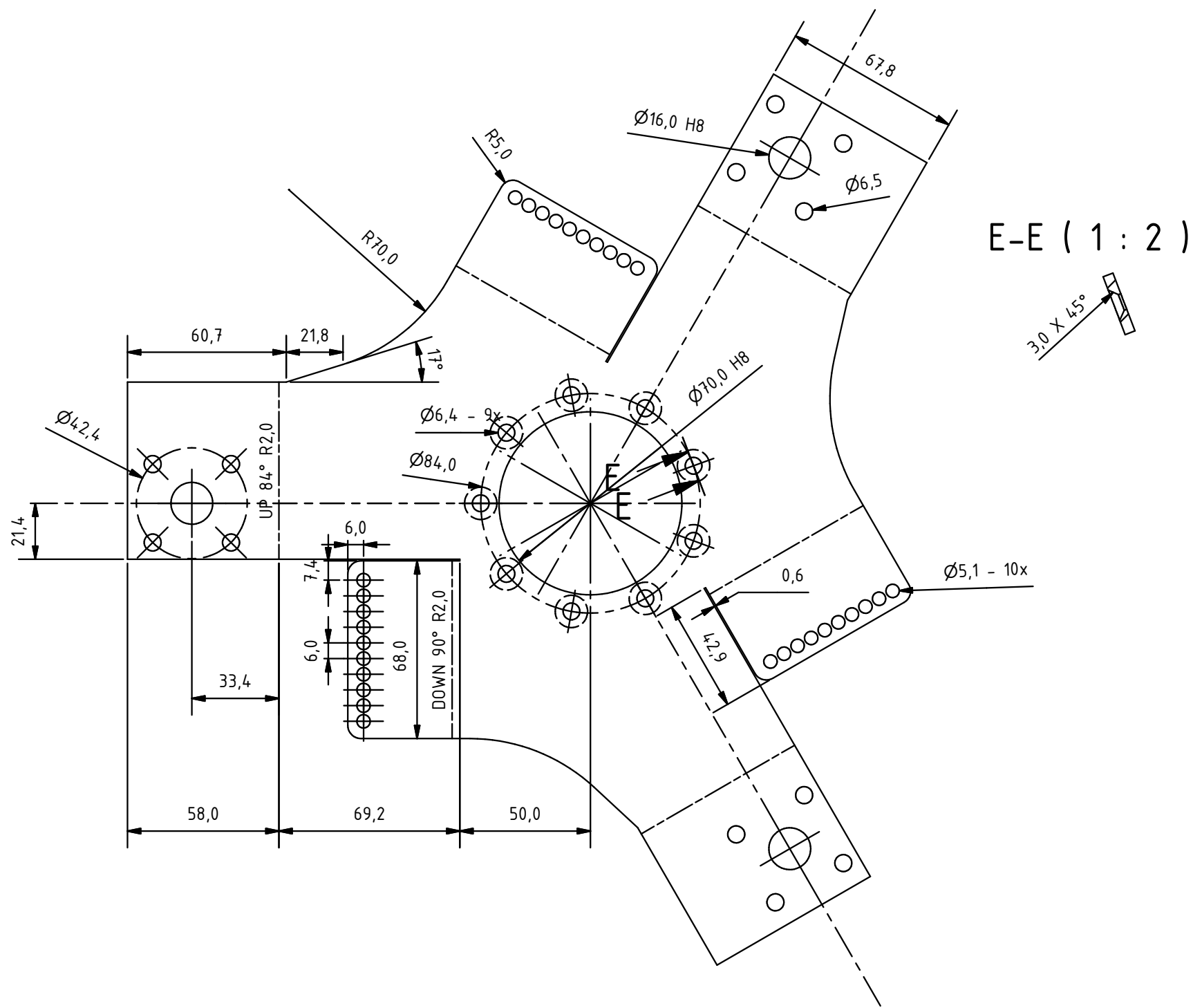
DIN ISO 1302
ISO 2768 -
DIN EN ISO 13920 -

Erstellt 23/1/2018 Name Josep Fernández
Geprüft
letzte Bearbeitung
Freigabe

Passive pitch system

Overview

Fehlende Maße bitte den mitgelieferten STP- oder DXF-Daten entnehmen CNC-, DXF-Daten anfordern



E-E (1 : 2)

Thickness: 6mm

Diese Zeichnung und die darin enthaltene Information unterliegt dem Urheberrecht! Das Nutzen, Kopieren und Weitergeben bedarf der Zustimmung des Erstellers.
Schutzvermerk nach DIN ISO 16016 beachten!

enbreeze GmbH Tel. +49 30 98 61 27 10
Marzahn Str. 34 Fax. +49 30 51 30 45 85
13053 Berlin

www.enbreeze.com info@enbreeze.com

Oberfläche		Maßstab	1:2	Position	Menge
DIN ISO 1302 ISO 2768 - m DIN EN ISO 13920 -		Aluminum 6061 alternativ			
Erstellt	Datum	Name			
Geprüft	23/1/2018	Josep Fernández			
letzte Bearbeitung					
Freigabe					

Passive pitch system

Allgemeintoleranzen nach DIN ISO 2768-1		Grenzmaße für Längenmaße	
Toleranzklasse		Grenzmaße in mm für Normalbereich in mm	
fs (fein)	±0,05	0,5	±0,05
fn (mittel)	±0,10	0,5 bis 3	±0,10
fp (grob)	±0,15	3 bis 30	±0,15
fs (sehr fein)	±0,02	30 bis 100	±0,05
fn (sehr mittel)	±0,05	100 bis 400	±0,10
fp (sehr grob)	±0,20	400 bis 1000	±0,20
		1000 bis 2000	±0,30
		2000 bis 4000	±0,50
		über 4000	±0,70

Hub sheet 1

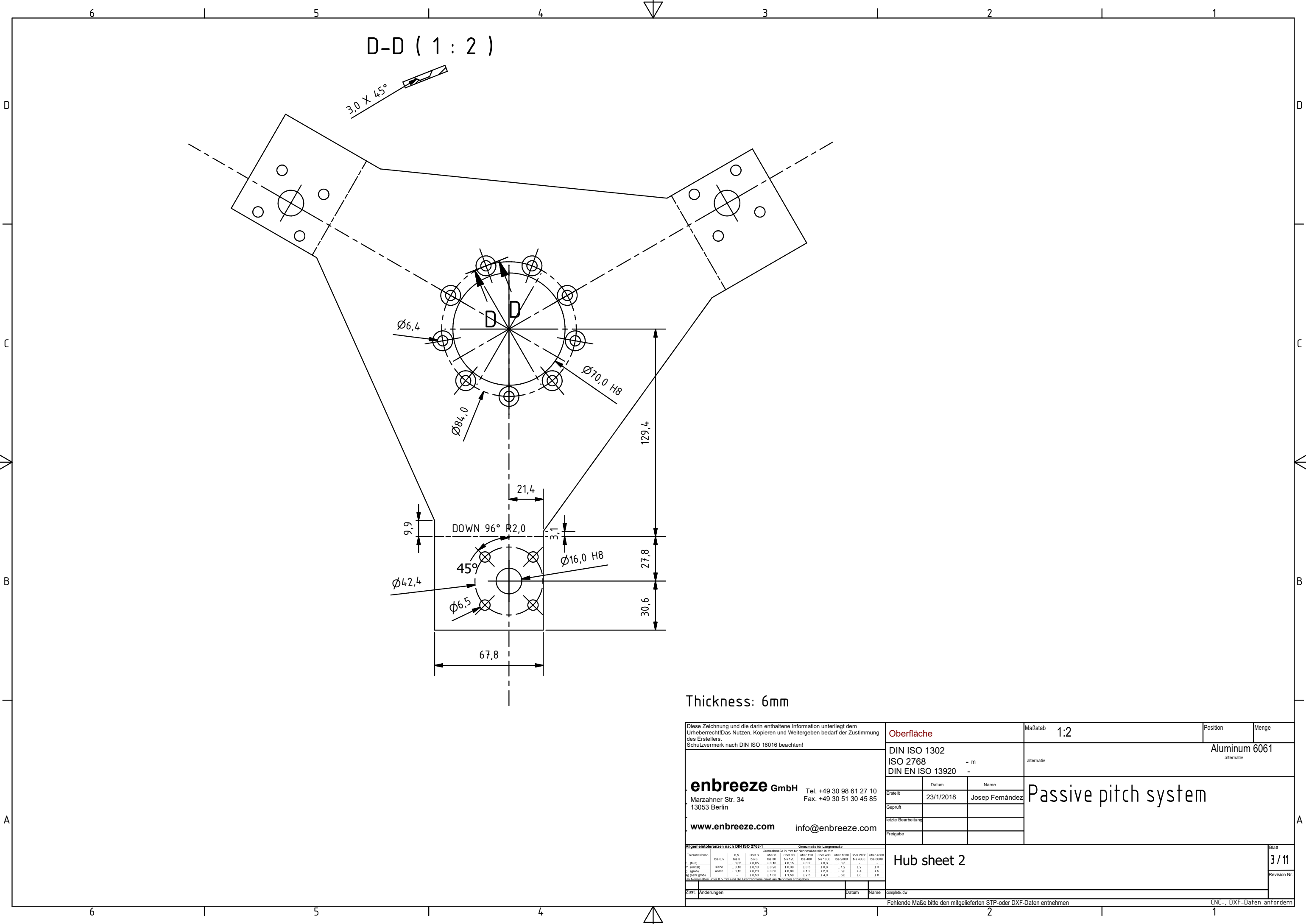
Blatt

2 / 11

Revision Nr.

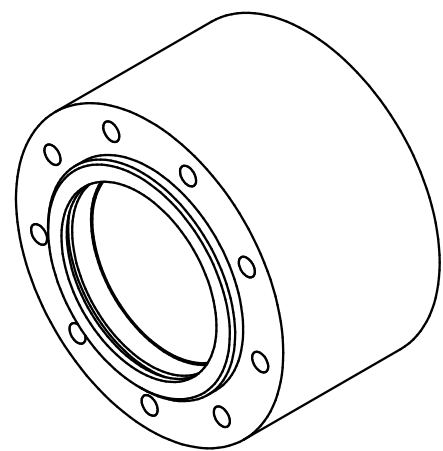
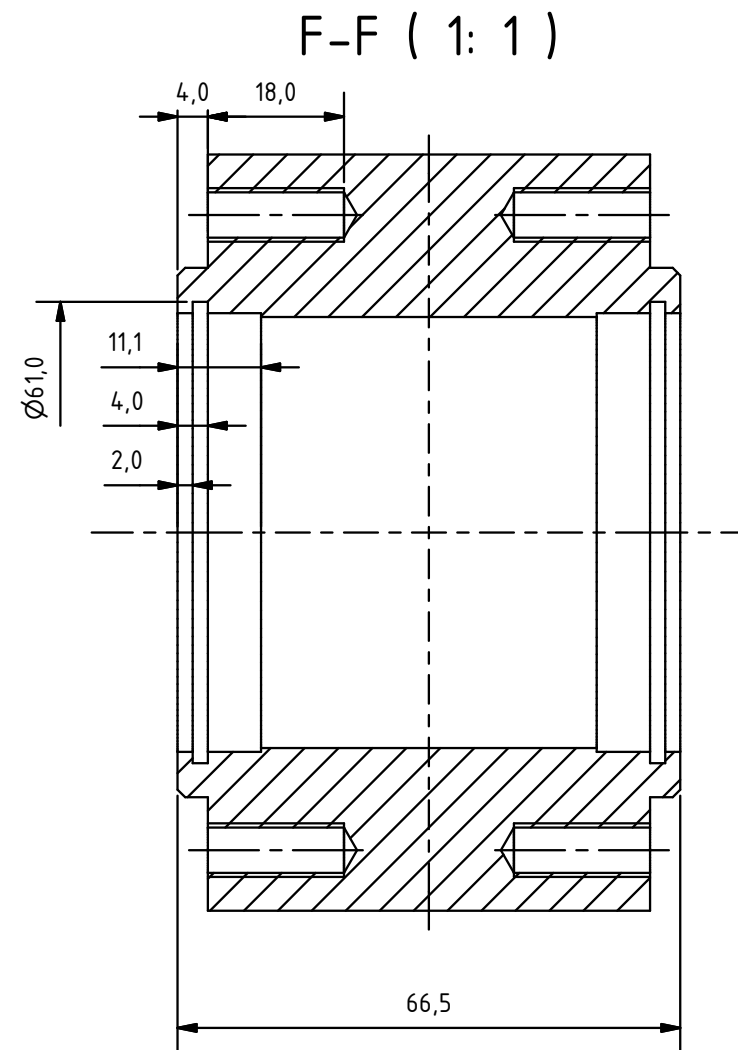
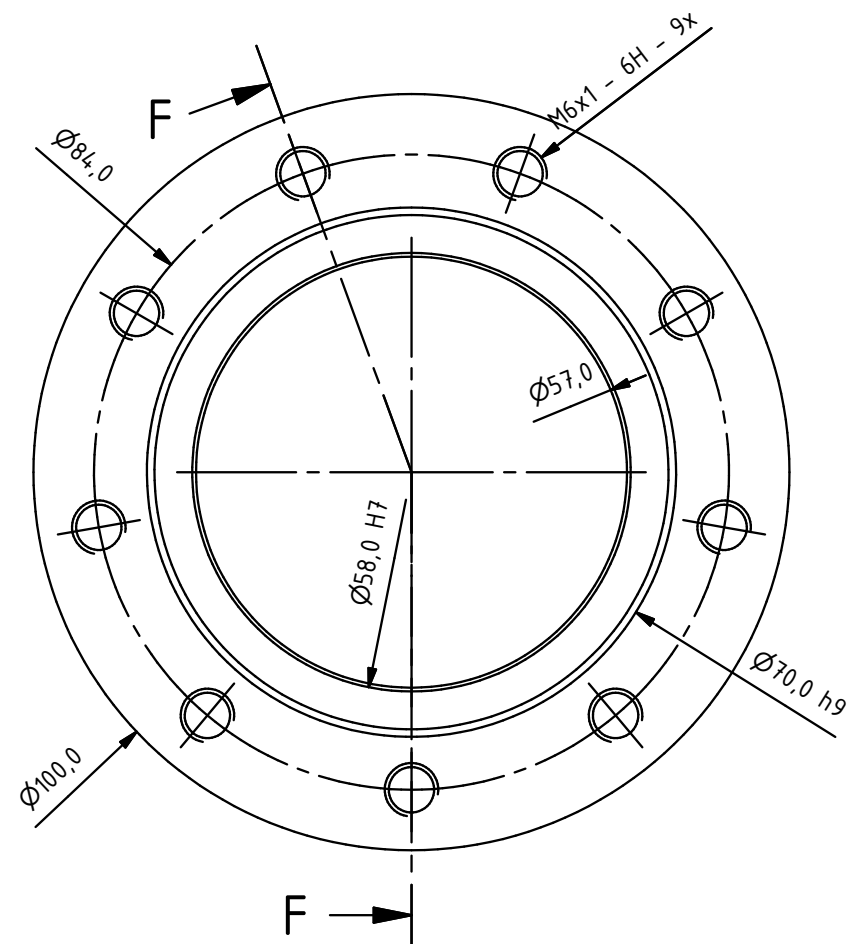
Fehlende Maße bitte den mitgelieferten STP- oder DXF-Daten entnehmen

CNC-, DXF-Daten anfordern



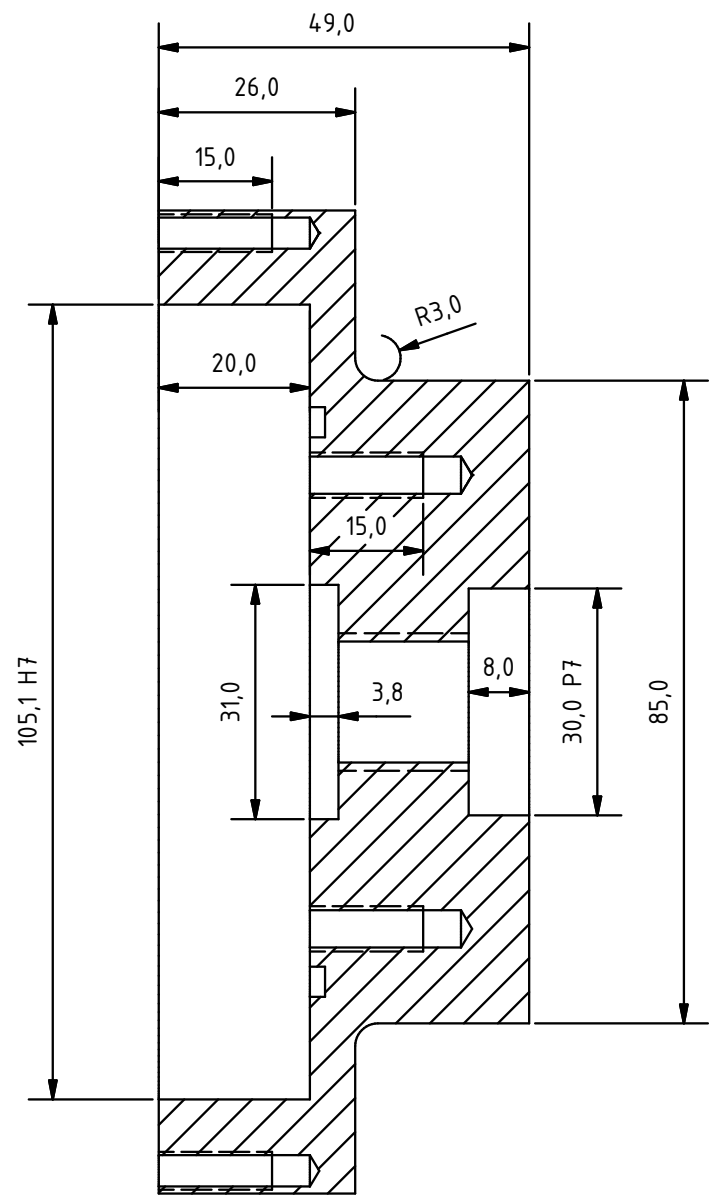
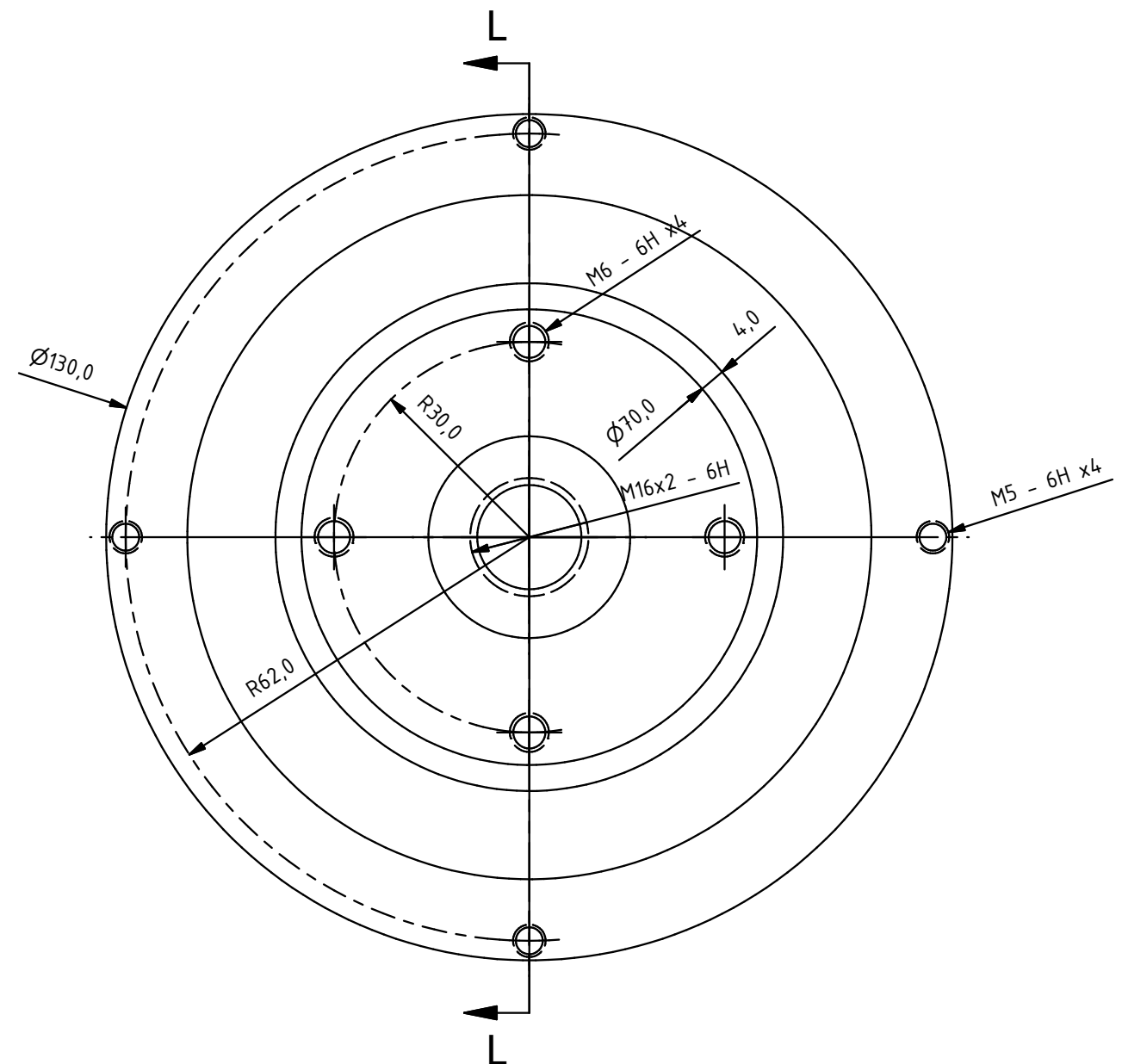
Thickness: 6mm

Diese Zeichnung und die darin enthaltene Information unterliegt dem Urheberrecht! Das Nutzen, Kopieren und Weitergeben bedarf der Zustimmung des Erstellers. Schutzvermerk nach DIN ISO 16016 beachten!		Oberfläche		Maßstab 1:2	Position	Menge																																																																											
enbreeze GmbH Tel. +49 30 98 61 27 10 Marzahner Str. 34 13053 Berlin Fax. +49 30 51 30 45 85 www.enbreeze.com info@enbreeze.com		DIN ISO 1302		Aluminum 6061																																																																													
		ISO 2768 - m		alternativ																																																																													
		DIN EN ISO 13920 -		Passive pitch system																																																																													
		<table border="1"> <tr><td>Erstellt</td><td>Datum</td><td>Name</td></tr> <tr><td>Geprüft</td><td>23/1/2018</td><td>Josep Fernández</td></tr> <tr><td>letzte Bearbeitung</td><td></td><td></td></tr> <tr><td>Freigabe</td><td></td><td></td></tr> </table>		Erstellt	Datum	Name	Geprüft	23/1/2018	Josep Fernández	letzte Bearbeitung			Freigabe																																																																				
Erstellt	Datum	Name																																																																															
Geprüft	23/1/2018	Josep Fernández																																																																															
letzte Bearbeitung																																																																																	
Freigabe																																																																																	
Hub sheet 2				Blatt 3 / 11																																																																													
<table border="1"> <thead> <tr> <th colspan="2">Allgemeintoleranzen nach DIN ISO 2768-1</th> <th colspan="8">Grenzmaße für Längemaße</th> </tr> <tr> <th>Toleranzklasse</th> <th>Größe</th> <th colspan="8">Grenzmaße in mm für Normalbereich in mm</th> </tr> <tr> <th></th> <th>Größe</th> <th>über 0,5 bis 3</th> <th>über 3 bis 6</th> <th>über 6 bis 30</th> <th>über 30 bis 100</th> <th>über 100 bis 400</th> <th>über 400 bis 1000</th> <th>über 1000 bis 2000</th> <th>über 2000 bis 4000</th> <th>über 4000 bis 8000</th> </tr> </thead> <tbody> <tr> <td>f (mm)</td> <td>±0,05</td> <td>±0,05</td> <td>±0,10</td> <td>±0,15</td> <td>±0,20</td> <td>±0,30</td> <td>±0,40</td> <td>±0,50</td> <td>±0,60</td> <td>±0,70</td> </tr> <tr> <td>M (mm)</td> <td>±0,10</td> <td>±0,10</td> <td>±0,20</td> <td>±0,30</td> <td>±0,40</td> <td>±0,50</td> <td>±0,60</td> <td>±0,70</td> <td>±0,80</td> <td>±0,90</td> </tr> <tr> <td>H (mm)</td> <td>±0,15</td> <td>±0,20</td> <td>±0,30</td> <td>±0,40</td> <td>±0,50</td> <td>±0,60</td> <td>±0,70</td> <td>±0,80</td> <td>±0,90</td> <td>±1,00</td> </tr> <tr> <td>g (mehr groß)</td> <td>±0,50</td> <td>±1,00</td> <td>±1,50</td> <td>±2,00</td> <td>±2,50</td> <td>±3,00</td> <td>±4,00</td> <td>±5,00</td> <td>±6,00</td> <td>±8,00</td> </tr> </tbody> </table>		Allgemeintoleranzen nach DIN ISO 2768-1		Grenzmaße für Längemaße								Toleranzklasse	Größe	Grenzmaße in mm für Normalbereich in mm									Größe	über 0,5 bis 3	über 3 bis 6	über 6 bis 30	über 30 bis 100	über 100 bis 400	über 400 bis 1000	über 1000 bis 2000	über 2000 bis 4000	über 4000 bis 8000	f (mm)	±0,05	±0,05	±0,10	±0,15	±0,20	±0,30	±0,40	±0,50	±0,60	±0,70	M (mm)	±0,10	±0,10	±0,20	±0,30	±0,40	±0,50	±0,60	±0,70	±0,80	±0,90	H (mm)	±0,15	±0,20	±0,30	±0,40	±0,50	±0,60	±0,70	±0,80	±0,90	±1,00	g (mehr groß)	±0,50	±1,00	±1,50	±2,00	±2,50	±3,00	±4,00	±5,00	±6,00	±8,00			CNC-, DXF-Daten anfordern		
Allgemeintoleranzen nach DIN ISO 2768-1		Grenzmaße für Längemaße																																																																															
Toleranzklasse	Größe	Grenzmaße in mm für Normalbereich in mm																																																																															
	Größe	über 0,5 bis 3	über 3 bis 6	über 6 bis 30	über 30 bis 100	über 100 bis 400	über 400 bis 1000	über 1000 bis 2000	über 2000 bis 4000	über 4000 bis 8000																																																																							
f (mm)	±0,05	±0,05	±0,10	±0,15	±0,20	±0,30	±0,40	±0,50	±0,60	±0,70																																																																							
M (mm)	±0,10	±0,10	±0,20	±0,30	±0,40	±0,50	±0,60	±0,70	±0,80	±0,90																																																																							
H (mm)	±0,15	±0,20	±0,30	±0,40	±0,50	±0,60	±0,70	±0,80	±0,90	±1,00																																																																							
g (mehr groß)	±0,50	±1,00	±1,50	±2,00	±2,50	±3,00	±4,00	±5,00	±6,00	±8,00																																																																							
Zust. Änderungen		Datum Name		complete idw																																																																													
				Fehlende Maße bitte den mitgelieferten STP- oder DXF-Daten entnehmen																																																																													

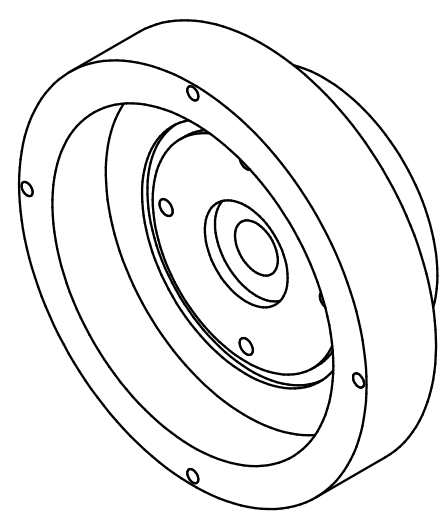


Chamfers without dimension: 1.00x45°

Diese Zeichnung und die darin enthaltene Information unterliegt dem Urheberrecht! Das Nutzen, Kopieren und Weitergeben bedarf der Zustimmung des Erstellers. Schutzvermerk nach DIN ISO 16016 beachten!		Oberfläche		Maßstab 1:1	Position	Menge																																																																	
enbreeze GmbH Tel. +49 30 98 61 27 10 Marzahner Str. 34 Fax. +49 30 51 30 45 85 13053 Berlin www.enbreeze.com info@enbreeze.com		DIN ISO 1302		Aluminum 6061																																																																			
		ISO 2768 - m		alternativ																																																																			
		DIN EN ISO 13920 -		Passive pitch system																																																																			
		Erstellt	Datum					Name																																																															
Geprüft																																																																							
<table border="1"> <thead> <tr> <th colspan="2">Allgemeintoleranzen nach DIN ISO 2768-1</th> <th colspan="8">Grenzmaße für Längenmaße</th> </tr> <tr> <th>Toleranzklasse</th> <th>Grenzmaße in mm für Nennmaßbereich in mm</th> <th>bis 0,5</th> <th>über 0,5 bis 0,8</th> <th>über 0,8 bis 1,6</th> <th>über 1,6 bis 3,15</th> <th>über 3,15 bis 6,3</th> <th>über 6,3 bis 12,5</th> <th>über 12,5 bis 25</th> <th>über 25 bis 50</th> <th>über 50 bis 100</th> </tr> </thead> <tbody> <tr> <td>F (frei)</td> <td></td> <td>± 0,05</td> <td>± 0,05</td> <td>± 0,10</td> <td>± 0,15</td> <td>± 0,2</td> <td>± 0,3</td> <td>± 0,5</td> <td>± 0,8</td> <td>± 1,2</td> </tr> <tr> <td>M (mittel)</td> <td></td> <td>± 0,10</td> <td>± 0,10</td> <td>± 0,20</td> <td>± 0,30</td> <td>± 0,5</td> <td>± 0,8</td> <td>± 1,2</td> <td>± 2</td> <td>± 3</td> </tr> <tr> <td>H (groß)</td> <td></td> <td>± 0,15</td> <td>± 0,20</td> <td>± 0,30</td> <td>± 0,50</td> <td>± 1,0</td> <td>± 1,5</td> <td>± 2,5</td> <td>± 4</td> <td>± 6</td> </tr> <tr> <td>g (sehr groß)</td> <td></td> <td>± 0,50</td> <td>± 1,00</td> <td>± 1,50</td> <td>± 2,5</td> <td>± 4,0</td> <td>± 6,0</td> <td>± 8</td> <td>± 8</td> <td>± 8</td> </tr> </tbody> </table>		Allgemeintoleranzen nach DIN ISO 2768-1		Grenzmaße für Längenmaße								Toleranzklasse	Grenzmaße in mm für Nennmaßbereich in mm	bis 0,5	über 0,5 bis 0,8	über 0,8 bis 1,6	über 1,6 bis 3,15	über 3,15 bis 6,3	über 6,3 bis 12,5	über 12,5 bis 25	über 25 bis 50	über 50 bis 100	F (frei)		± 0,05	± 0,05	± 0,10	± 0,15	± 0,2	± 0,3	± 0,5	± 0,8	± 1,2	M (mittel)		± 0,10	± 0,10	± 0,20	± 0,30	± 0,5	± 0,8	± 1,2	± 2	± 3	H (groß)		± 0,15	± 0,20	± 0,30	± 0,50	± 1,0	± 1,5	± 2,5	± 4	± 6	g (sehr groß)		± 0,50	± 1,00	± 1,50	± 2,5	± 4,0	± 6,0	± 8	± 8	± 8	Datum		Name		Blatt
Allgemeintoleranzen nach DIN ISO 2768-1		Grenzmaße für Längenmaße																																																																					
Toleranzklasse	Grenzmaße in mm für Nennmaßbereich in mm	bis 0,5	über 0,5 bis 0,8	über 0,8 bis 1,6	über 1,6 bis 3,15	über 3,15 bis 6,3	über 6,3 bis 12,5	über 12,5 bis 25	über 25 bis 50	über 50 bis 100																																																													
F (frei)		± 0,05	± 0,05	± 0,10	± 0,15	± 0,2	± 0,3	± 0,5	± 0,8	± 1,2																																																													
M (mittel)		± 0,10	± 0,10	± 0,20	± 0,30	± 0,5	± 0,8	± 1,2	± 2	± 3																																																													
H (groß)		± 0,15	± 0,20	± 0,30	± 0,50	± 1,0	± 1,5	± 2,5	± 4	± 6																																																													
g (sehr groß)		± 0,50	± 1,00	± 1,50	± 2,5	± 4,0	± 6,0	± 8	± 8	± 8																																																													
Zust. Änderungen		Datum		Name		5 / 11																																																																	
				complete idw		Revision Nr.																																																																	
				Fehlende Maße bitte den mitgelieferten STP- oder DXF-Daten entnehmen		CNC-, DXF-Daten anfordern																																																																	



SECTION L-L
SCALE 1 : 1



Diese Zeichnung und die darin enthaltene Information unterliegt dem Urheberrecht! Das Nutzen, Kopieren und Weitergeben bedarf der Zustimmung des Erstellers. Schutzvermerk nach DIN ISO 16016 beachten!		Oberfläche		Maßstab 1:1	Position	Menge																																																																																					
enbreeze GmbH Tel. +49 30 98 61 27 10 Marzahner Str. 34 Fax. +49 30 51 30 45 85 13053 Berlin www.enbreeze.com info@enbreeze.com		DIN ISO 1302		Aluminum 6061																																																																																							
		ISO 2768 - m		alternativ																																																																																							
		DIN EN ISO 13920 -		Passive pitch system																																																																																							
		Erstellt	Datum					Name																																																																																			
Geprüft																																																																																											
		letzte Bearbeitung																																																																																									
		Freigabe																																																																																									
Allgemeintoleranzen nach DIN ISO 2768-1 <small>Grenzabmaße in mm für Normalbereich in mm</small>		Grenzmaße für Längenmaße <small>Grenzabmaße in mm für Normalbereich in mm</small>		Blatt																																																																																							
<table border="1"> <tr> <th>Toleranzklasse</th> <th>bis 0,5</th> <th>über 0,5 bis 3</th> <th>über 3 bis 6</th> <th>über 6 bis 30</th> <th>über 30 bis 120</th> <th>über 120 bis 400</th> <th>über 400 bis 1000</th> <th>über 1000 bis 2000</th> <th>über 2000 bis 4000</th> <th>über 4000 bis 8000</th> </tr> <tr> <td>f. (mm)</td> <td>±0,05</td> <td>±0,05</td> <td>±0,10</td> <td>±0,15</td> <td>±0,2</td> <td>±0,3</td> <td>±0,5</td> <td>±0,8</td> <td>±1,0</td> <td>±1,5</td> </tr> <tr> <td>H. (mm)</td> <td>same</td> <td>±0,10</td> <td>±0,20</td> <td>±0,30</td> <td>±0,5</td> <td>±0,8</td> <td>±1,2</td> <td>±2,0</td> <td>±3,0</td> <td>±5,0</td> </tr> <tr> <td>g. (mehr groß)</td> <td>-</td> <td>±0,15</td> <td>±0,30</td> <td>±0,50</td> <td>±1,0</td> <td>±1,5</td> <td>±2,0</td> <td>±3,0</td> <td>±5,0</td> <td>±8,0</td> </tr> <tr> <td>H. (mehr groß)</td> <td>-</td> <td>±0,50</td> <td>±1,00</td> <td>±1,50</td> <td>±2,5</td> <td>±4,0</td> <td>±6,0</td> <td>±8,0</td> <td>±10,0</td> <td>±15,0</td> </tr> </table>		Toleranzklasse	bis 0,5	über 0,5 bis 3	über 3 bis 6	über 6 bis 30	über 30 bis 120	über 120 bis 400	über 400 bis 1000	über 1000 bis 2000	über 2000 bis 4000	über 4000 bis 8000	f. (mm)	±0,05	±0,05	±0,10	±0,15	±0,2	±0,3	±0,5	±0,8	±1,0	±1,5	H. (mm)	same	±0,10	±0,20	±0,30	±0,5	±0,8	±1,2	±2,0	±3,0	±5,0	g. (mehr groß)	-	±0,15	±0,30	±0,50	±1,0	±1,5	±2,0	±3,0	±5,0	±8,0	H. (mehr groß)	-	±0,50	±1,00	±1,50	±2,5	±4,0	±6,0	±8,0	±10,0	±15,0	<table border="1"> <tr> <th>Toleranzklasse</th> <th>bis 3</th> <th>über 3 bis 6</th> <th>über 6 bis 30</th> <th>über 30 bis 120</th> <th>über 120 bis 400</th> <th>über 400 bis 1000</th> <th>über 1000 bis 2000</th> <th>über 2000 bis 4000</th> <th>über 4000 bis 8000</th> </tr> <tr> <td>f. (mm)</td> <td>±0,10</td> <td>±0,15</td> <td>±0,20</td> <td>±0,30</td> <td>±0,5</td> <td>±0,8</td> <td>±1,2</td> <td>±2,0</td> <td>±3,0</td> </tr> <tr> <td>H. (mm)</td> <td>±0,15</td> <td>±0,20</td> <td>±0,30</td> <td>±0,50</td> <td>±1,0</td> <td>±1,5</td> <td>±2,5</td> <td>±4,0</td> <td>±6,0</td> </tr> </table>		Toleranzklasse	bis 3	über 3 bis 6	über 6 bis 30	über 30 bis 120	über 120 bis 400	über 400 bis 1000	über 1000 bis 2000	über 2000 bis 4000	über 4000 bis 8000	f. (mm)	±0,10	±0,15	±0,20	±0,30	±0,5	±0,8	±1,2	±2,0	±3,0	H. (mm)	±0,15	±0,20	±0,30	±0,50	±1,0	±1,5	±2,5	±4,0	±6,0	6 / 11		
Toleranzklasse	bis 0,5	über 0,5 bis 3	über 3 bis 6	über 6 bis 30	über 30 bis 120	über 120 bis 400	über 400 bis 1000	über 1000 bis 2000	über 2000 bis 4000	über 4000 bis 8000																																																																																	
f. (mm)	±0,05	±0,05	±0,10	±0,15	±0,2	±0,3	±0,5	±0,8	±1,0	±1,5																																																																																	
H. (mm)	same	±0,10	±0,20	±0,30	±0,5	±0,8	±1,2	±2,0	±3,0	±5,0																																																																																	
g. (mehr groß)	-	±0,15	±0,30	±0,50	±1,0	±1,5	±2,0	±3,0	±5,0	±8,0																																																																																	
H. (mehr groß)	-	±0,50	±1,00	±1,50	±2,5	±4,0	±6,0	±8,0	±10,0	±15,0																																																																																	
Toleranzklasse	bis 3	über 3 bis 6	über 6 bis 30	über 30 bis 120	über 120 bis 400	über 400 bis 1000	über 1000 bis 2000	über 2000 bis 4000	über 4000 bis 8000																																																																																		
f. (mm)	±0,10	±0,15	±0,20	±0,30	±0,5	±0,8	±1,2	±2,0	±3,0																																																																																		
H. (mm)	±0,15	±0,20	±0,30	±0,50	±1,0	±1,5	±2,5	±4,0	±6,0																																																																																		
Zust. Änderungen		Datum Name		Blatt																																																																																							
		complete idw		Revision Nr.																																																																																							
		Fehlende Maße bitte den mitgelieferten STP- oder DXF-Daten entnehmen		CNC-, DXF-Daten anfordern																																																																																							

6 1 5 1 4 1 3 1 2 1 1

D

D

C

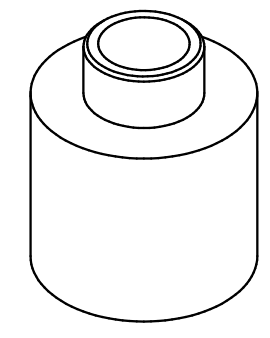
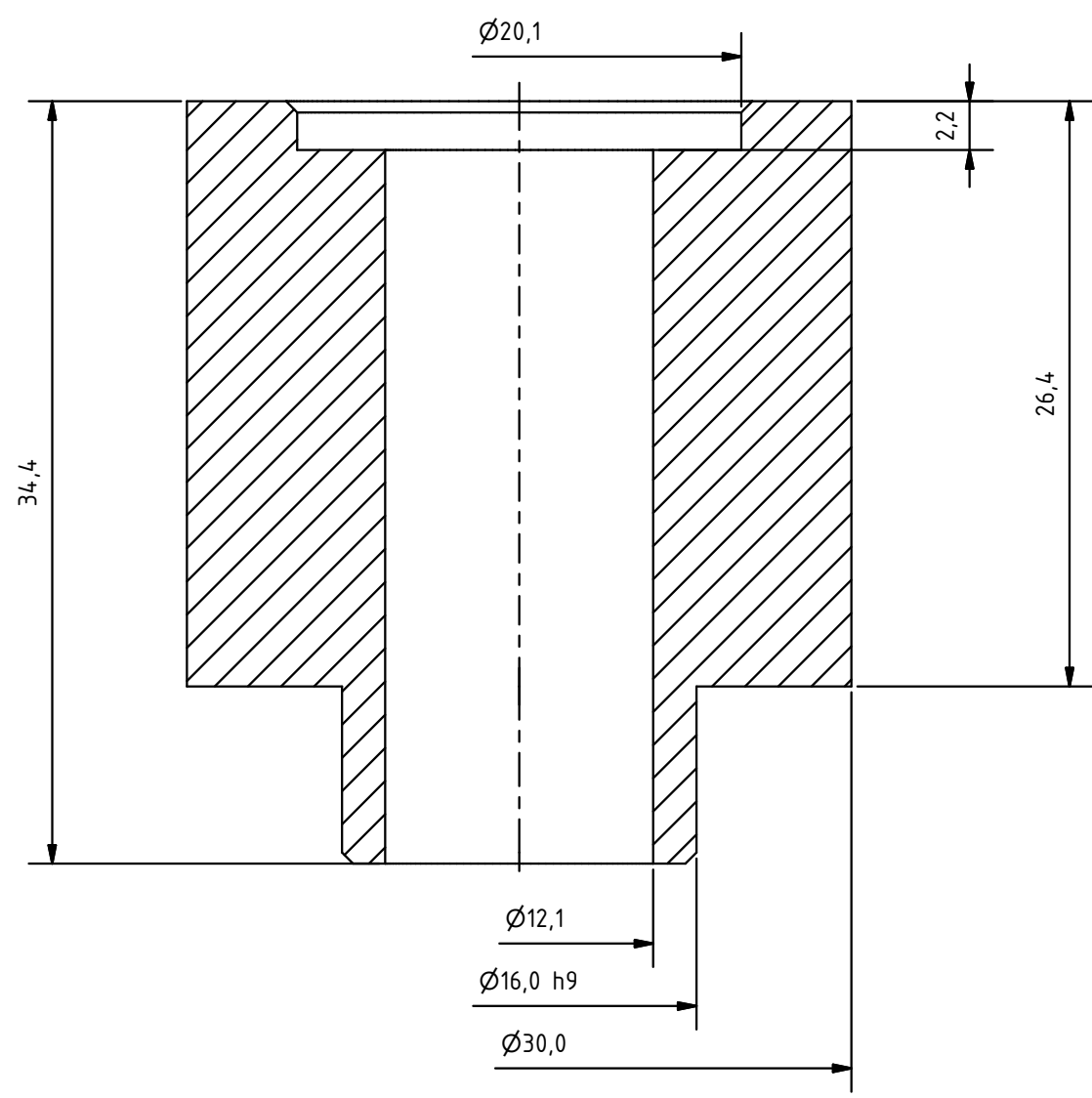
C

B

B

A

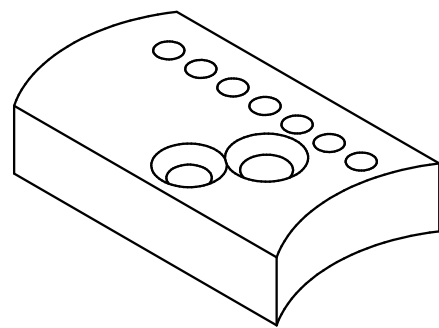
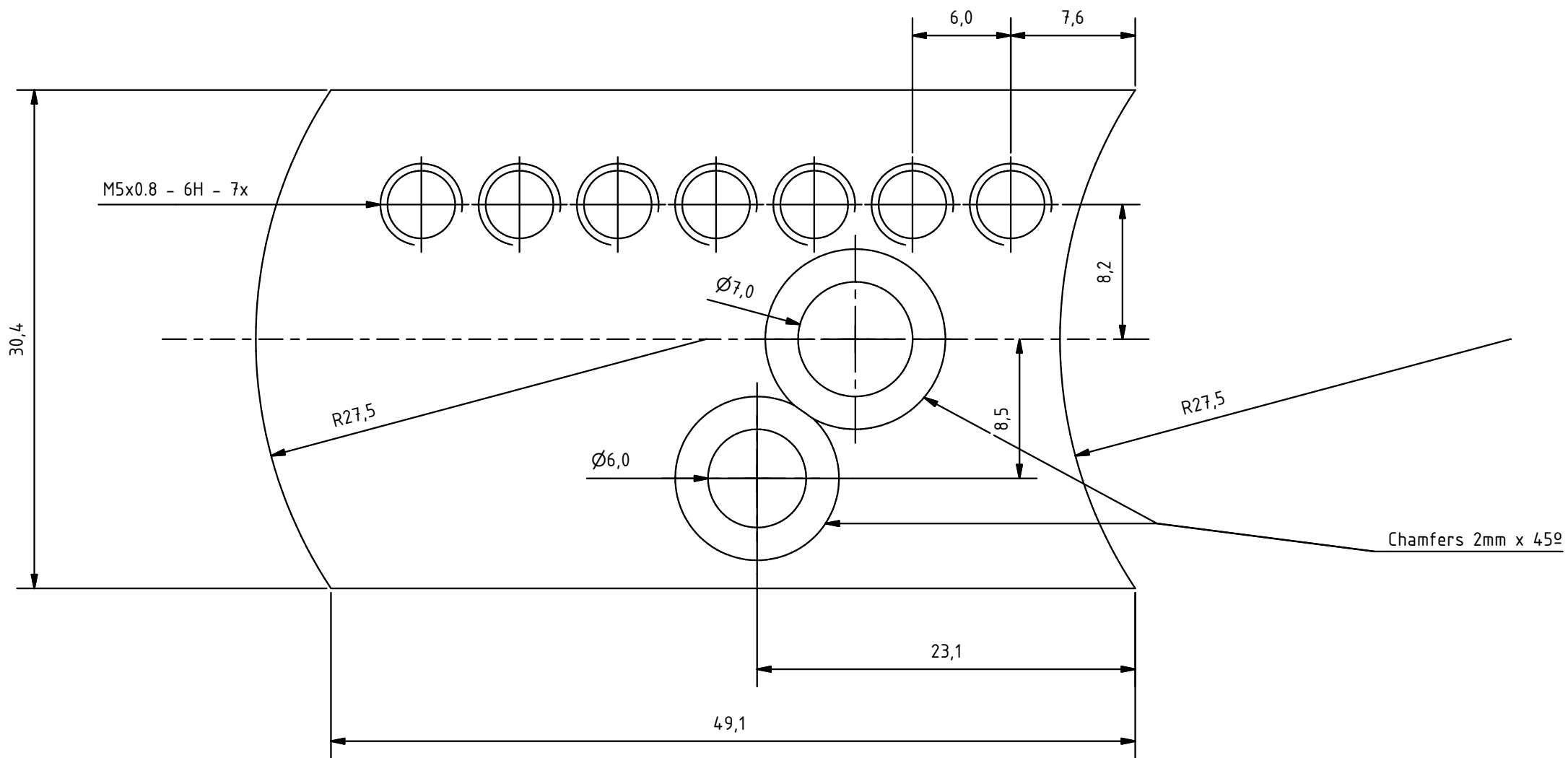
A



Chamfers 0.50mm x 45°

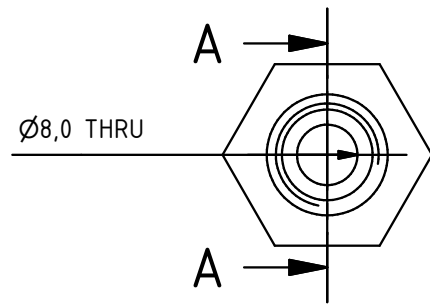
Diese Zeichnung und die darin enthaltene Information unterliegt dem Urheberrecht! Das Nutzen, Kopieren und Weitergeben bedarf der Zustimmung des Erstellers. Schutzvermerk nach DIN ISO 16016 beachten!		Oberfläche		Maßstab 3 : 1	Position	Menge
enbreeze GmbH Tel. +49 30 98 61 27 10 Marzahner Str. 34 Fax. +49 30 51 30 45 85 13053 Berlin www.enbreeze.com info@enbreeze.com		DIN ISO 1302		Aluminum 6061		
		ISO 2768 - m		alternativ		
		DIN EN ISO 13920 -				
		Erstellt: 23/1/2018 Name: Josep Fernández Geprüft: letzte Bearbeitung: 8/9/2017 Freigabe:		Passive pitch system		
Blatt 7 / 11 Revision Nr.						
Allgemeintoleranzen nach DIN ISO 2768-1 Grenzabmaße in mm für Normalbereich in mm Toleranzklasse bis 0,5 über 0,5 bis 3 über 3 bis 6 über 6 bis 30 über 30 bis 120 über 120 bis 400 über 400 bis 1000 über 1000 bis 2000 über 2000 bis 4000 über 4000 f (fein) ± 0,05 ± 0,05 ± 0,10 ± 0,15 ± 0,2 ± 0,3 ± 0,5 m (mittel) ± 0,10 ± 0,10 ± 0,20 ± 0,30 ± 0,5 ± 0,8 ± 1,2 ± 2 ± 3 g (groß) ± 0,15 ± 0,20 ± 0,30 ± 0,50 ± 0,8 ± 1,2 ± 2 ± 3 ± 5 H (sehr groß) ± 0,50 ± 1,00 ± 1,50 ± 2,5 ± 4,0 ± 6,0 ± 8 ± 12 Bei Normalmaßen über 0,5 mm sind die Grenzabmaße direkt am Normalmaß anzugeben.		Blade base		CNC-, DXF-Daten anfordern		
Zust. Änderungen Datum Name		complete idw		Fehlende Maße bitte den mitgelieferten STP- oder DXF-Daten entnehmen		

6 1 5 1 4 1 3 1 2 1 1

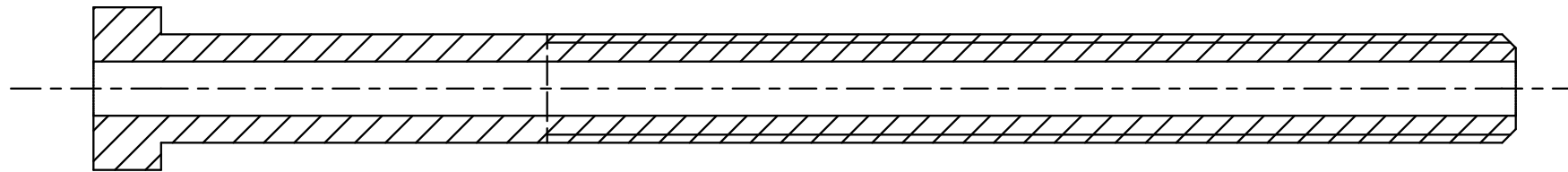


Thickness 11 mm

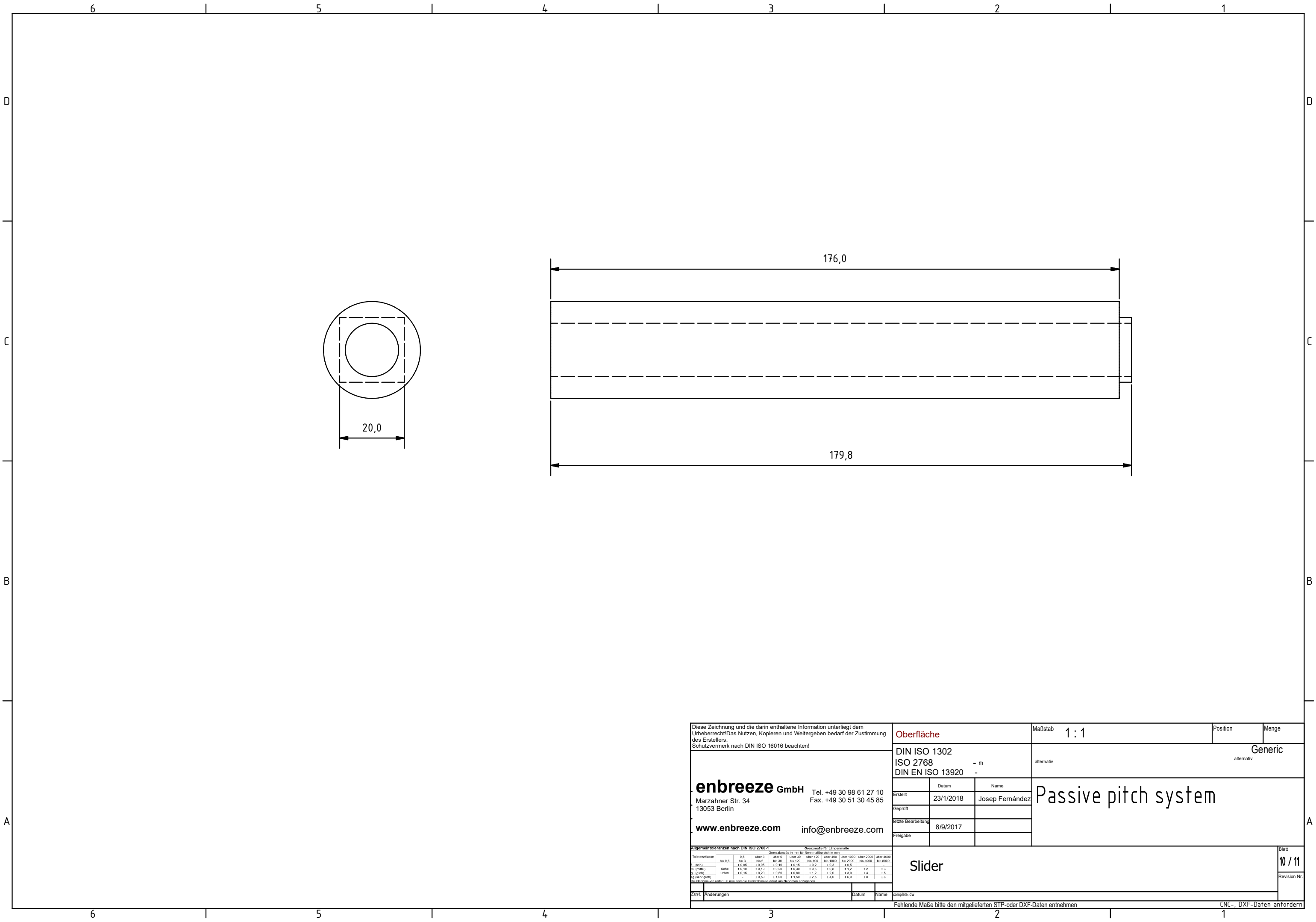
Diese Zeichnung und die darin enthaltene Information unterliegt dem Urheberrecht! Das Nutzen, Kopieren und Weitergeben bedarf der Zustimmung des Erstellers. Schutzvermerk nach DIN ISO 16016 beachten!		Oberfläche		Maßstab 3:1	Position	Menge																																																																											
enbreeze GmbH Tel. +49 30 98 61 27 10 Marzahner Str. 34 Fax. +49 30 51 30 45 85 13053 Berlin www.enbreeze.com info@enbreeze.com		DIN ISO 1302		Aluminum 6061																																																																													
		ISO 2768 - m		alternativ																																																																													
		DIN EN ISO 13920 -		Passive pitch system																																																																													
		Erstellt	Datum	Name																																																																													
	23/1/2018	Josep Fernández																																																																															
Geprüft																																																																																	
letzte Bearbeitung	8/9/2017																																																																																
Freigabe																																																																																	
Allgemeintoleranzen nach DIN ISO 2768-1 <small>Größenabstände in mm für Normalbereich in mm</small>		Grenzmaße für Längenmaße <small>Größenabstände in mm für Normalbereich in mm</small>		Blatt																																																																													
<table border="1"> <tr> <th>Toleranzklasse</th> <th>bis 0,5</th> <th>über 0,5 bis 3</th> <th>über 3 bis 6</th> <th>über 6 bis 30</th> <th>über 30 bis 100</th> <th>über 100 bis 400</th> <th>über 400 bis 1000</th> <th>über 1000 bis 2000</th> <th>über 2000 bis 4000</th> <th>über 4000 bis 8000</th> </tr> <tr> <td>f. (mm)</td> <td>±0,05</td> <td>±0,05</td> <td>±0,10</td> <td>±0,15</td> <td>±0,2</td> <td>±0,3</td> <td>±0,5</td> <td>±0,8</td> <td>±1,2</td> <td>±1,6</td> </tr> <tr> <td>M. (mm)</td> <td>same</td> <td>±0,10</td> <td>±0,20</td> <td>±0,30</td> <td>±0,5</td> <td>±0,8</td> <td>±1,2</td> <td>±2</td> <td>±3</td> <td>±5</td> </tr> <tr> <td>H. (mehr groß)</td> <td>-</td> <td>-0,10</td> <td>-0,20</td> <td>-0,30</td> <td>-0,5</td> <td>-0,8</td> <td>-1,2</td> <td>-2</td> <td>-3</td> <td>-5</td> </tr> <tr> <td>H. (weniger groß)</td> <td>±0,05</td> <td>±1,00</td> <td>±1,50</td> <td>±2,5</td> <td>±4,0</td> <td>±6,0</td> <td>±8</td> <td>±8</td> <td>±8</td> <td>±8</td> </tr> </table>		Toleranzklasse	bis 0,5	über 0,5 bis 3	über 3 bis 6	über 6 bis 30	über 30 bis 100	über 100 bis 400	über 400 bis 1000	über 1000 bis 2000	über 2000 bis 4000	über 4000 bis 8000	f. (mm)	±0,05	±0,05	±0,10	±0,15	±0,2	±0,3	±0,5	±0,8	±1,2	±1,6	M. (mm)	same	±0,10	±0,20	±0,30	±0,5	±0,8	±1,2	±2	±3	±5	H. (mehr groß)	-	-0,10	-0,20	-0,30	-0,5	-0,8	-1,2	-2	-3	-5	H. (weniger groß)	±0,05	±1,00	±1,50	±2,5	±4,0	±6,0	±8	±8	±8	±8	<table border="1"> <tr> <th>Größenabstände in mm für Normalbereich in mm</th> <th>bis 3</th> <th>über 3 bis 6</th> <th>über 6 bis 30</th> <th>über 30 bis 100</th> <th>über 100 bis 400</th> <th>über 400 bis 1000</th> <th>über 1000 bis 2000</th> <th>über 2000 bis 4000</th> <th>über 4000 bis 8000</th> </tr> <tr> <td>Größenabstände in mm für Normalbereich in mm</td> <td>±0,10</td> <td>±0,15</td> <td>±0,20</td> <td>±0,30</td> <td>±0,5</td> <td>±0,8</td> <td>±1,2</td> <td>±2</td> <td>±3</td> </tr> </table>		Größenabstände in mm für Normalbereich in mm	bis 3	über 3 bis 6	über 6 bis 30	über 30 bis 100	über 100 bis 400	über 400 bis 1000	über 1000 bis 2000	über 2000 bis 4000	über 4000 bis 8000	Größenabstände in mm für Normalbereich in mm	±0,10	±0,15	±0,20	±0,30	±0,5	±0,8	±1,2	±2	±3	8 / 11		
Toleranzklasse	bis 0,5	über 0,5 bis 3	über 3 bis 6	über 6 bis 30	über 30 bis 100	über 100 bis 400	über 400 bis 1000	über 1000 bis 2000	über 2000 bis 4000	über 4000 bis 8000																																																																							
f. (mm)	±0,05	±0,05	±0,10	±0,15	±0,2	±0,3	±0,5	±0,8	±1,2	±1,6																																																																							
M. (mm)	same	±0,10	±0,20	±0,30	±0,5	±0,8	±1,2	±2	±3	±5																																																																							
H. (mehr groß)	-	-0,10	-0,20	-0,30	-0,5	-0,8	-1,2	-2	-3	-5																																																																							
H. (weniger groß)	±0,05	±1,00	±1,50	±2,5	±4,0	±6,0	±8	±8	±8	±8																																																																							
Größenabstände in mm für Normalbereich in mm	bis 3	über 3 bis 6	über 6 bis 30	über 30 bis 100	über 100 bis 400	über 400 bis 1000	über 1000 bis 2000	über 2000 bis 4000	über 4000 bis 8000																																																																								
Größenabstände in mm für Normalbereich in mm	±0,10	±0,15	±0,20	±0,30	±0,5	±0,8	±1,2	±2	±3																																																																								
Zust. Änderungen		Datum		Name		complete idw																																																																											
						Fehlende Maße bitte den mitgelieferten STP- oder DXF-Daten entnehmen																																																																											
						CNC-, DXF-Daten anfordern																																																																											



A-A (1 : 1)



Diese Zeichnung und die darin enthaltene Information unterliegt dem Urheberrecht! Das Nutzen, Kopieren und Weitergeben bedarf der Zustimmung des Erstellers. Schutzvermerk nach DIN ISO 16016 beachten!		Oberfläche		Maßstab 1 : 1	Position	Menge																																																					
enbreeze GmbH Tel. +49 30 98 61 27 10 Marzahner Str. 34 Fax. +49 30 51 30 45 85 13053 Berlin www.enbreeze.com info@enbreeze.com		DIN ISO 1302		Generic																																																							
		ISO 2768 - m		alternativ																																																							
		DIN EN ISO 13920 -		alternativ																																																							
		<table border="1"> <tr><td>Erstellt</td><td>Datum</td><td>Name</td></tr> <tr><td>Geprüft</td><td>23/1/2018</td><td>Josep Fernández</td></tr> <tr><td>letzte Bearbeitung</td><td></td><td></td></tr> <tr><td>Freigabe</td><td>8/9/2017</td><td></td></tr> </table>		Erstellt	Datum	Name	Geprüft	23/1/2018	Josep Fernández	letzte Bearbeitung			Freigabe	8/9/2017		Passive pitch system																																											
Erstellt	Datum	Name																																																									
Geprüft	23/1/2018	Josep Fernández																																																									
letzte Bearbeitung																																																											
Freigabe	8/9/2017																																																										
<table border="1"> <tr><td>Zust.</td><td colspan="2">Änderungen</td><td>Datum</td><td>Name</td></tr> <tr><td> </td><td colspan="2"> </td><td> </td><td> </td></tr> </table>		Zust.	Änderungen		Datum	Name						Blatt 9 / 11																																															
Zust.	Änderungen		Datum	Name																																																							
Hex screw M16 <small>Alle Nennmaße unter 0,5 mm sind die Grenzmaße für den Normalbereich.</small>		<table border="1"> <thead> <tr> <th rowspan="2">Toleranzklasse</th> <th colspan="6">Grenzmaße in mm für Normalbereich in mm</th> <th colspan="2">Grenzmaße für Längenmaße</th> </tr> <tr> <th>bis 0,5</th> <th>über 0,5 bis 3</th> <th>über 3 bis 30</th> <th>über 30 bis 100</th> <th>über 100 bis 400</th> <th>über 400 bis 1000</th> <th>über 1000 bis 2000</th> <th>über 2000 bis 4000</th> </tr> </thead> <tbody> <tr> <td>f (Rein)</td> <td>± 0,05</td> <td>± 0,05</td> <td>± 0,10</td> <td>± 0,15</td> <td>± 0,2</td> <td>± 0,3</td> <td>± 0,5</td> <td>± 1</td> </tr> <tr> <td>M (mittel)</td> <td>± 0,10</td> <td>± 0,10</td> <td>± 0,20</td> <td>± 0,30</td> <td>± 0,5</td> <td>± 0,8</td> <td>± 1,2</td> <td>± 2</td> </tr> <tr> <td>H (gröÙ)</td> <td>± 0,15</td> <td>± 0,20</td> <td>± 0,30</td> <td>± 0,50</td> <td>± 1,0</td> <td>± 1,5</td> <td>± 2,0</td> <td>± 3</td> </tr> <tr> <td>Hg (sehr groÙ)</td> <td>± 0,20</td> <td>± 0,30</td> <td>± 0,50</td> <td>± 1,00</td> <td>± 2,0</td> <td>± 3,0</td> <td>± 5,0</td> <td>± 8</td> </tr> </tbody> </table>		Toleranzklasse	Grenzmaße in mm für Normalbereich in mm						Grenzmaße für Längenmaße		bis 0,5	über 0,5 bis 3	über 3 bis 30	über 30 bis 100	über 100 bis 400	über 400 bis 1000	über 1000 bis 2000	über 2000 bis 4000	f (Rein)	± 0,05	± 0,05	± 0,10	± 0,15	± 0,2	± 0,3	± 0,5	± 1	M (mittel)	± 0,10	± 0,10	± 0,20	± 0,30	± 0,5	± 0,8	± 1,2	± 2	H (gröÙ)	± 0,15	± 0,20	± 0,30	± 0,50	± 1,0	± 1,5	± 2,0	± 3	Hg (sehr groÙ)	± 0,20	± 0,30	± 0,50	± 1,00	± 2,0	± 3,0	± 5,0	± 8	CNC-, DXF-Daten anfordern		
Toleranzklasse	Grenzmaße in mm für Normalbereich in mm						Grenzmaße für Längenmaße																																																				
	bis 0,5	über 0,5 bis 3	über 3 bis 30	über 30 bis 100	über 100 bis 400	über 400 bis 1000	über 1000 bis 2000	über 2000 bis 4000																																																			
f (Rein)	± 0,05	± 0,05	± 0,10	± 0,15	± 0,2	± 0,3	± 0,5	± 1																																																			
M (mittel)	± 0,10	± 0,10	± 0,20	± 0,30	± 0,5	± 0,8	± 1,2	± 2																																																			
H (gröÙ)	± 0,15	± 0,20	± 0,30	± 0,50	± 1,0	± 1,5	± 2,0	± 3																																																			
Hg (sehr groÙ)	± 0,20	± 0,30	± 0,50	± 1,00	± 2,0	± 3,0	± 5,0	± 8																																																			
Zust. Änderungen		Datum Name		Fehlende Maße bitte den mitgelieferten STP- oder DXF-Daten entnehmen																																																							



Diese Zeichnung und die darin enthaltene Information unterliegt dem Urheberrecht! Das Nutzen, Kopieren und Weitergeben bedarf der Zustimmung des Erstellers.
Schutzvermerk nach DIN ISO 16016 beachten!

enbreeze GmbH Tel. +49 30 98 61 27 10
Marzahner Str. 34 Fax. +49 30 51 30 45 85
13053 Berlin
www.enbreeze.com info@enbreeze.com

Oberfläche		Maßstab 1:1	Position	Menge
DIN ISO 1302 ISO 2768 - m DIN EN ISO 13920 -		alternativ	Generic alternativ	
Erstellt	Datum	Name	Passive pitch system	
Gepflegt	23/1/2018	Josep Fernández		
letzte Bearbeitung	8/9/2017			
Freigabe				

Allgemeintoleranzen nach DIN ISO 2768-1		Grenzmaße für Längenmaße									
		in mm für Normalbereich in mm									
Toleranzklasse	Größe	0,5	über 0,5	über 3	über 6	über 30	über 120	über 400	über 1000	über 2000	über 4000
F (frei)	bis 0,5	±0,05	±0,05	±0,10	±0,15	±0,20	±0,25	±0,30	±0,40	±0,50	±0,60
M (mittel)	same	±0,10	±0,10	±0,20	±0,30	±0,40	±0,50	±0,60	±0,80	±1,00	±1,20
H (hohe Präzision)	unten	±0,05	±0,05	±0,10	±0,15	±0,20	±0,25	±0,30	±0,40	±0,50	±0,60
Hg (sehr hoch)		±0,05	±0,05	±0,10	±0,15	±0,20	±0,25	±0,30	±0,40	±0,50	±0,60

Slider

Zust. Änderungen Datum Name complete idw

Fehlende Maße bitte den mitgelieferten STP- oder DXF-Daten entnehmen

CNC-, DXF-Daten anfordern

Blatt 10 / 11
Revision Nr.

